The Thesis Committee for Christopher Allen Johnson Blyton
Certifies that this is the approved version of the following thesis:

Kinetics of CO_2 Dissolution in Brine: Experimental Measurement and Application to Geologic Storage

APPROVED BY
SUPERVISING COMMITTEE:

Supervisor:

Steven L. Bryant

Larry W. Lake

Kinetics of CO_2 Dissolution in Brine: Experimental Measurement and Application to Geologic Storage

by

Christopher Allen Johnson Blyton, B.E.

Thesis

Presented to the Faculty of the Graduate School of

The University of Texas at Austin

in Partial Fulfillment

of the Requirements

for the Degree of

Master of Science in Engineering

The University of Texas at Austin

May 2012

Acknowledgements

Graduate study at The University of Texas at Austin has proven to be both a challenge and an immensely rewarding experience. Completing a Masters of Science degree by the research option has broadened my horizons as an engineer. It has provided a deeper insight into science that is often only examined at a low level of detail for engineering purposes. I would like to thank Dr. Steven L. Bryant for demanding high quality work, while understanding the competing time pressures faced as a graduate student. His support and encouragement is much appreciated.

I would like to thank staff and faculty for their assistance over the duration of the research project. Mr. Glen Baum's experience with experimental equipment has been invaluable in working through the many issues associated with constructing an experimental apparatus from scratch. I would like to thank Dr. Larry W. Lake for being a reader of this thesis and providing his valuable feedback. The assistance of Ms. Lindsey Smith of the Division of Statistics and Scientific Computation group is appreciated.

This research would not be possible without the support of the Geologic CO_2 Storage Joint Industry Project sponsors; Shell, Chevron, Luminant, Statoil, BP, Halliburton, ConocoPhillips, ExxonMobil, CMG and USGS.

Lastly, while family and friends in Australia may have been skeptical of the wisdom of moving to Texas, I have been fortunate to have their continued support. Settling, at least temporarily, in the US has provided the opportunity to make many new friends and see more of the world.

Abstract

Kinetics of CO_2 Dissolution in Brine: Experimental Measurement and Application to Geologic Storage

Christopher Allen Johnson Blyton, M.S.E.

The University of Texas at Austin, 2012

Supervisor: Steven L. Bryant

A novel approach to geologic CO_2 sequestration is the surface dissolution method. This method involves lifting native brine from an aquifer, dissolution of CO_2 into the brine using pressurized mixing and injection of the CO_2 saturated brine back into the aquifer. This approach has several advantages over the conventional approach, including minimization of the risk of buoyancy driven leakage and dramatic reduction in the extent of pressure elevation in the storage structure.

The mass transfer coefficient for the CO_2/brine two-phase system and associated transport calculations allow efficient design of the surface equipment required to dissolve CO_2 under pressure. This data was not previously available in the literature. Original experimental data on the rate of dissolution of CO_2 into Na-Ca-Cl brines across a range of temperatures and wet CO_2 densities are presented. From this data, the intrinsic mass transfer coefficient between CO_2-rich and aqueous phases has been calculated. The

statistically significant variation in the mass transfer coefficient was evaluated and compared with the variation caused by the experimental method.

An empirical correlation was developed that demonstrates that the mass transfer coefficient is a function of the NaCl salinity, temperature and wet CO_2 density. For the conditions tested, the value of the coefficient is in the range of 0.015 to 0.056 cm/s. Greater temperature and smaller NaCl salinity increases the mass transfer coefficient. There is an interaction effect between temperature and wet CO_2 density, which increases or decreases the mass transfer coefficient depending on the value of each. $CaCl_2$ salinity does not have a statistically significant effect on the mass transfer coefficient.

The transport calculations demonstrate that wellhead co-injection of CO_2 and brine is feasible, providing the same technical outcome at lower cost. For example, assuming a 2000 ft deep well and typical aquifer injection conditions, complete dissolution of the bulk CO_2 phase can be achieved at 670 ft for bubbles of 0.16 cm initial radius. Using a horizontal pipe or mixing tank was also shown to be feasible. Gas entrainment was shown to provide a marked reduction in size of mixing apparatus required.

Table of Contents

List of Tables

List of Figures

Chapter 1: Introduction

'Climate change' refers to major changes in temperature, precipitation or wind patterns lasting for decades or longer (EPA, 2012). Data collection of various types, instrumental and proxy measurement shows that historically the Earth's climate has been changing as far back as 650 000 years (IPCC, 2007). However, during the short period of time since the start of the industrial revolution, there has been an increase in the average surface temperature and a causal link demonstrated to anthropogenic greenhouse gas emissions (IPCC, 2007). Of these greenhouse gas emissions, carbon dioxide contributes the most to temperature increase.

Geologic CO_2 sequestration is a technically feasible technology that may be used as a component of a greenhouse gas emission reduction strategy. Sufficient storage capacity for a large quantity of CO_2 is available in the subsurface. However, there is a risk of buoyancy driven leakage when employing the standard approach to CO_2 sequestration. The surface dissolution approach described later in this chapter eliminates this risk. The kinetics for CO_2 dissolution into brine is critical to the feasibility of this approach, but such data are not presently available in the literature.

1.1 Recent Climate Change

The commonly used term 'global warming' is an average increase in the temperature of the Earth's surface. Global warming is one aspect of climate change. Global surface temperatures have increased by 0.7 K since the late 19th century (NOAA, 2012). The small temperature increase itself does not pose a great threat to human health or safety. However, there have been associated changes such as a large drying trend since

the mid 1950s over many land areas (IPCC, 2007). Marked increases in drought, as well as heavy rains and flooding are an indication of greater climate extremes. There is evidence of an increase in category 4 and 5 storms since 1970 (IPCC, 2007). A rise in global mean sea level has occurred at an average rate of 1.7×10^{-3} m/year over the past 100 years (NOAA, 2012). Sea level rise reduces land available in low-lying areas, storm activity poses a direct threat to human safety and precipitation patterns have a direct impact on food security.

1.2 Radiative Forcing and Greenhouse Gas Emissions

Radiative forcing is a measure of how the energy balance of the Earth and atmosphere is influenced when factors that affect climate are altered (IPCC, 2007). It is the rate of energy change per unit area of the globe as measured at the top of the atmosphere. It provides a useful metric to understand the relative importance of known contributions to climate change. The radiative forcing for several human activities and natural processes, between the start of the industrial revolution 1750 and 2005, is presented in Figure 1.1.

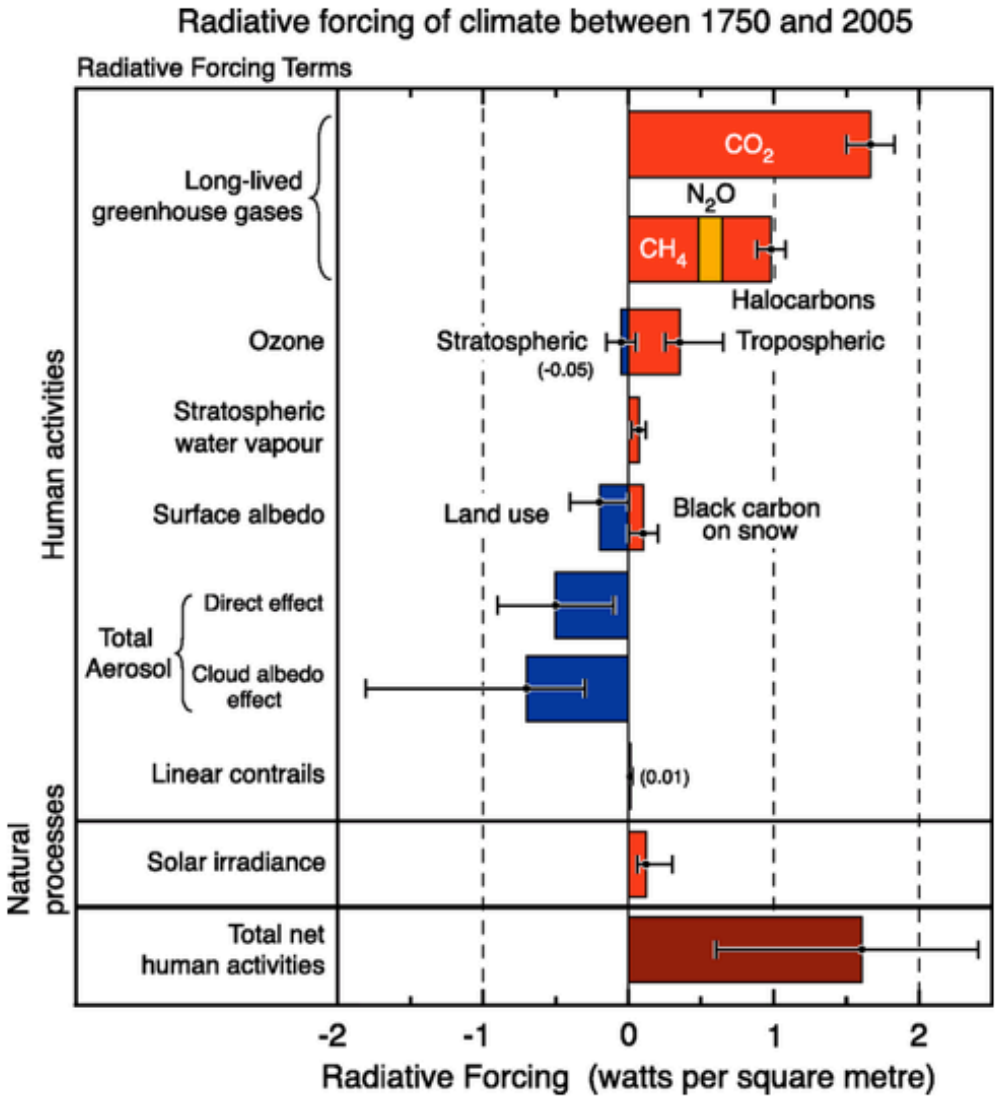

Figure 1.1: Radiative forcing of climate between 1750 and 2005, for various human activities and natural processes (IPCC, 2007)

Figure 1.1 demonstrates that the human impact on climate exceeds that caused by natural processes. Further, out of human activity related activities, greenhouse gas emissions constitute the largest contribution. Of all the greenhouse gas emissions, CO_2

contributes more than each of CH_4, N_2O and the halocarbons. Figure 1.2 shows the atmospheric concentration of major greenhouse gases over the past 2000 years.

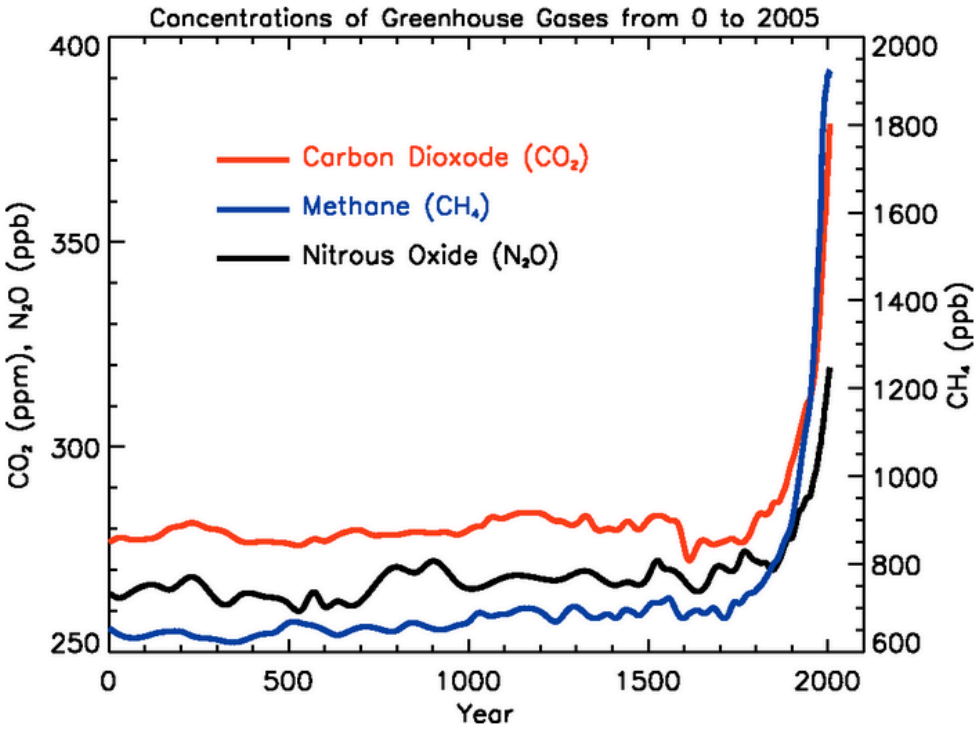

Figure 1.2: Recent historical concentration of major greenhouse gases in the atmosphere (IPCC, 2007)

Figure 1.2 demonstrates that since the industrial revolution, greenhouse gas concentrations have dramatically increased relative to the previous relatively steady concentrations.

The order of magnitude of the radiative forcing caused by CO_2 and CH_4 emissions is the same, though CH_4 emissions and concentration is the atmosphere are far smaller. The IPCC developed a metric, the Global Warming Potential, to compare the ability of

each greenhouse gas to trap heat in the atmosphere relative to another gas. This metric is defined as the ratio of the time integrated radiative forcing caused by release of a standard amount of the gas compared to the reference, which is CO_2. Thus the GWP of CO_2 is 1. The GWPs of a number of gases are shown in Table 1.1.

Gas	GWP
CO_2	1
CH_4*	21
N_2O	310
HFC-23	11,700
HFC-32	650
HFC-125	2,800
HFC-134a	1,300
HFC-143a	3,800
HFC-152a	140
HFC-227ea	2,900
HFC-236fa	6,300
HFC-4310mee	1,300
CF_4	6,500
C_2F_6	9,200
C_4F_{10}	7,000
C_6F_{14}	7,400
SF_6	23,900

Table 1.1: The Global Warming Potential of several greenhouse gases (EPA, 2012)

Table 1.1 shows the GWPs of many greenhouse gases over a 100-year period. The timeframe used for calculation is important since some greenhouse gases remain in the atmosphere for greater periods of time than others. As a result the GWPs calculated for different periods of time will not necessarily be the same.

1.3 CO_2 EMISSIONS

GWP weighted global emissions of greenhouse gases increased by 70% between 1970 and 2004 (IPCC, 2007). During 2004, 49 $GtCO_2$ equivalent was emitted and CO_2 itself represented 77% of total anthropogenic emissions. The breakdown of greenhouse gas emissions by sector is provided in Figure 1.3.

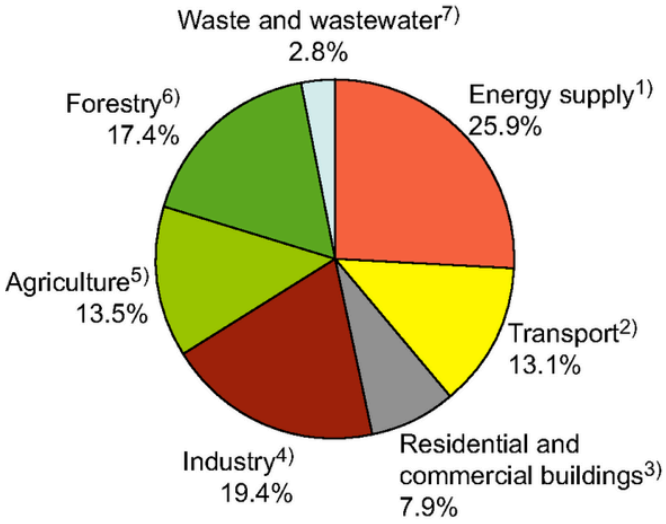

Figure 1.3: Greenhouse gas emissions by sector in 2004 (IPCC, 2007)

Figure 1.3 shows that the most significant contribution to greenhouse gas emissions is stationary energy supply, which consists primarily of fossil fuel combustion for electricity generation. The second largest contribution is that of industry, which includes cement production and iron and steel manufacturing, among others. The superscripts are from the source material and are not discussed here.

1.4 POTENTIAL OF GEOLOGIC CO_2 SEQUESTRATION

There are several possible approaches to reducing CO_2 emissions. These include energy efficiency improvements, adoption of less carbon intensive fuels, nuclear power and renewable energy among others (IPCC special report on CCS, 2005). An interim technology that may form part of a portfolio of actions to reduce CO_2 emissions is geologic sequestration. This process requires capture of CO_2 from stationary point sources, transport to the storage site and long-term isolation from the atmosphere. A summary of the worldwide point sources of CO_2 is presented in Table 1.2.

Process	Number of sources	Emissions ($MtCO_2$ yr^{-1})
Fossil fuels		
Power	4,942	10,539
Cement production	1,175	932
Refineries	638	798
Iron and steel industry	269	646
Petrochemical industry	470	379
Oil and gas processing	Not available	50
Other sources	90	33
Biomass		
Bioethanol and bioenergy	303	91
Total	**7,887**	**13,466**

Table 1.2: Number of stationary CO_2 sources and total emissions by category (IPCC, 2005)

According to the IPCC, it is likely that there is a technical potential of 2,000 $GtCO_2$ of storage capacity in geological formations. As noted above, total CO_2 emissions for 2004 were 49 $GtCO_2$, indicating that on the basis of storage capacity alone there is the potential for many years worth of storage. While there is ample pore volume available for CO_2 sequestration to be a significant part of emissions mitigation, Jain (2011) developed a metric termed the 'time weighted storage capacity' that demonstrated that this storage

capacity alone is not an adequate measure of CO_2 storage potential. Jain (2011) applied the time weighted storage capacity to a database of 1,200 depleted oil reservoirs in the US and found that on the time scale of several decades is only 10 to 20% of the nominal volumetric capacity. If the results are representative of the characteristics of worldwide possible CO_2 sequestration targets, this dramatically reduces the years worth of CO_2 emissions that could potentially be stored.

1.5 CO_2 SEQUESTRATION

The standard approach to geologic CO_2 sequestration is injection of bulk phase CO_2. There are several pilot projects of this type operating worldwide, such as Sleipner in the Norwegian North Sea and In Salah in Algeria. These projects have been operating since 1996 and 2004, respectively. Both sequester CO_2 stripped from produced hydrocarbon gas, CO_2 that would otherwise be vented to the atmosphere. At Sleipner, time lapse seismic was acquired before injection commenced and periodically since injection began (CO_2 storage Sleipner, 2012). This has demonstrated the evolution of the CO_2 plume over time and so far indicated that it is confined securely within the storage formation. Other monitoring technologies have also been used, such as high-resolution 2D seismic, seabed gravity, seabed controlled source electromagnetics and seabed imaging and bathymetry (CO_2 storage Sleipner, 2012). At In Salah, seismic, microseismic and satellite monitoring of the CO_2 plume has been used (CO_2 Storage In Salah, 2012). These are proven technologies that provide a high degree of confidence in the security of the sequestered CO_2, however continued monitoring of this type is expensive.

Several researchers have used compositional reservoir simulation to examine the movement and storage mechanisms of CO_2 during and post injection. One such study was undertaken by Kumar *et al*. (2005), who noted that the permanence of CO_2 stored as a bulk phase depends entirely on the integrity of the seal over long periods of time. As a result, Kumar *et al*. (2005) examined three other modes of CO_2 storage that avoid relying on cap rock integrity. The modes include pore level trapping, dissolution into brine and precipitation as a mineral. These mechanisms are termed permanent using the definition that CO_2 placed in the formation will not reach the surface any sooner than other species originally present in the system. Kumar *et al*. (2008) simulated typical deep saline aquifer conditions, running simulations for a number of cases of reservoir properties. The results showed that concerns about CO_2 leakage could be reduced by an injection strategy of injection in the bottom half of the aquifer. While such results are a positive development, there are still leakage risks posed by factors such as geologic uncertainty and other wellbores in the area.

Bryant (2008) studied buoyancy dominated flow of CO_2 in a storage aquifer, a further examination of the injection strategy proposed by Kumar *et al*. (2005). The objective was to examine the intrinsic instability of the displacement front and determine whether it leads to fingering. With fingers, CO_2 could reach the top seal of the aquifer and accumulate in large saturations, thereby once again relying on the integrity of the cap rock for storage security. Fine scale geostatistical realizations of permeability were considered, as were the effects of capillary pressure, anisotropy and dip angle. The conclusions drawn included that buoyant instability has only a small effect on the displacement front. However, CO_2 follow preferential flow paths because of

heterogeneity in permeability, drainage capillary pressure curve and anisotropy. As a result, reservoir characterization is critical to the injection strategy proposed.

1.6 SURFACE DISSOLUTION APPROACH TO CO_2 SEQUESTRATION

Considering the costs associated with continued monitoring of CO_2 plumes after bulk phase injection and the results of numerical simulation examining secure trapping mechanisms, alternative approaches that avoid leakage risk are desirable. One such approach is 'surface dissolution', first proposed by Burton (2008 and 2009). The surface dissolution approach involves lifting native brine from an aquifer, dissolving CO_2 in the brine on surface and re-injecting the CO_2 laden brine into the aquifer. The standard approach and the surface dissolution approach are shown in Figure 1.4.

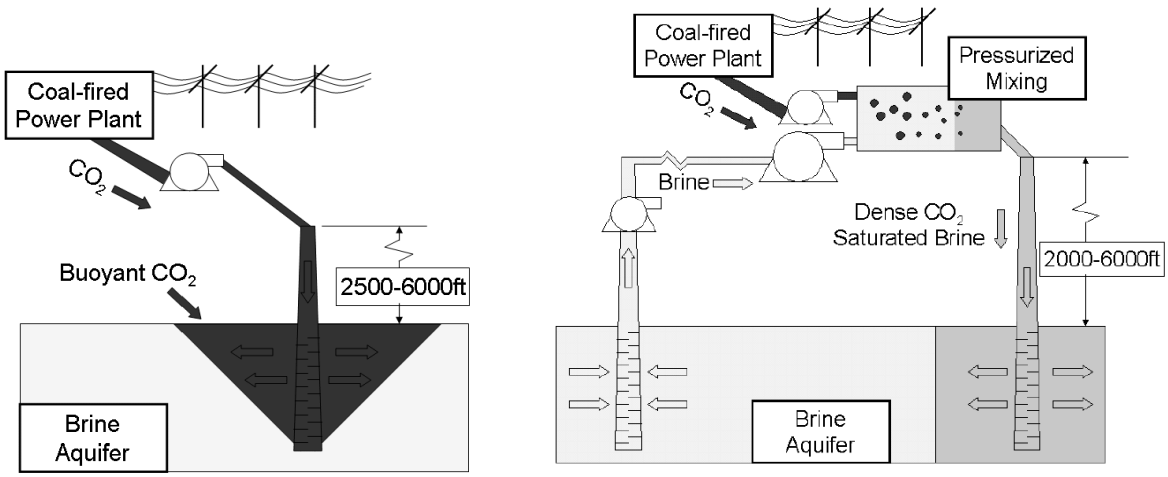

Figure 1.4: Standard approach to geologic CO_2 sequestration (left) and the surface dissolution approach (right), (Burton, 2008)

According to Song *et al*. (2005), the density of an aqueous phase increases with CO_2 concentration. Thus, CO_2 laden brine is denser than the native brine and the buoyancy driven leakage risk is eliminated by the surface dissolution approach. Single-phase flow is a result, eliminating the effects of mobility contrasts, fingering and relative permeability changes. Burton (2009) completed estimates of the capital costs for the additional facilities, along with the power requirements to determine the operating costs. When compared to the standard approach, an additional power consumption of 3 to 9% of the power plant capacity would be required and capital costs would be approximately 60% greater. The CO_2 capture process, which is required by both the standard and surface dissolution approaches, requires approximately 38% of the power plant capacity. In this context, an additional 3 to 9% is not prohibitive. The ongoing monitoring costs and liability that result from the standard approach can be significantly reduced by the surface dissolution approach.

One critical aspect of the surface dissolution process that could not be quantified by Burton (2009) was the kinetics for the dissolution of CO_2 into brine. Data on the kinetics of this process, applicable to well-mixed phases, was not available in the literature. This data is important to developing both more accurate estimates of the sizing of mixing apparatus as well as consideration of the type of mixing apparatus to be used. The research described in this thesis provides this data for a range of conditions likely to be encountered in the field.

1.7 STRUCTURE OF THE THESIS

This thesis consists of 5 chapters. Chapter 2 is a comprehensive review of the available literature pertinent to the study of the kinetics of CO_2 dissolution into brine. The results of a series of experiments conducted to quantify the mass transfer coefficient are presented in Chapter 3. Chapter 4 details application of the measured data to a number of possible configurations of surface dissolution equipment. Finally, Chapter 5 draws conclusions from the experimental data and its application, as well as covering possible future work.

1.7.1 Chapter 2: Literature Review

Review of the relevant literature leads to the conclusion that there is little data available for the mass transfer coefficient of similar fluid systems and that none is available for CO_2 and brine at the relevant temperature and wet CO_2 density. It is also discovered that in many cases experimental researchers present only the volumetric mass transfer coefficient, $k_L a$, without a means of separation into the mass transfer coefficient k_L and interfacial area a. This limits the broader applicability of the data.

1.7.2 Chapter 3: Results of Experiments

The results and analysis of a program of designed experiments to evaluate k_L across a range of synthetic brine composition, temperature and wet CO_2 density is presented. An experimental apparatus and procedure were developed specifically for this task. Before running the designed experiment, many preliminary experiments were conducted to understand the best configuration and parameters to run each experiment.

An empirical correlation is presented that demonstrates that k_L is a function of temperature, wet CO_2 density and brine composition.

1.7.3 Chapter 4: Application to Geologic CO_2 Storage

Using the experimental data presented in Chapter 3, several transport models are used to evaluate the implications to geologic CO_2 storage by the surface dissolution approach. The depth at which complete dissolution of bulk phase CO_2 is completely dissolved after co-injection with brine at the wellhead is examined, along with sizing of other surface mixing equipment.

1.7.4 Chapter 5: Conclusions and Future Work

Conclusions from the experimental data and application are presented. Possible directions for further related study are covered.

Chapter 2: Literature Review

Some aspects of the kinetics of CO_2 dissolution into liquid systems have been studied extensively. However, the approaches taken and data available are not sufficient for the efficient design of a surface dissolution facility to saturate reservoir brine with CO_2.

2.1 Kinetics of CO_2 Dissolution in Brine

2.1.1 Molecular Diffusion Governed Mass Transport

Bird *et al*. (2007) describes the movement of a species *A* through a binary mixture of *A* and *B*, due to a concentration gradient of *A*, by stating Fick's first law as follows:

$$J_{Ax} = -D_{AB}\frac{\partial C_A}{\partial x} \qquad \text{Equation 2.1}$$

with molar flux of *A* in direction *x* (m) J_{Ax} (mol/m^{2}s), diffusion coefficient of *A* in *B* D_{AB} (m^2/s) and concentration of *A* C_A (mol/m^3). Since the flux is dependent on concentration gradient, any concentration distribution other than uniform will result in mass being transferred until concentration homogeneity exists in the system.

The relationship in Equation 2.1 applies to gas, liquid and solid phases, however, the magnitude of the diffusion coefficient for the different states of matter varies greatly. Pritchard and Currie (1982) conducted experimental work using CO_2, N_2O, C_2H_4 and C_2H_6 gases injected at steady state through a tube and into a semi-infinite volume of air to determine their diffusion coefficients. For CO_2 into air, the measured value was 1.39×10^{-5} m^2/s at NTP. Tamimi *et al*. (1994) used a wetted sphere apparatus and water to measure liquid phase diffusion coefficients for H_2S, CO_2 and N_2O. For CO_2 into liquid water at 293 K, the measured value was 1.76×10^{-9} m^2/s. Comparison of the diffusion coefficients

for CO_2 in air and water demonstrates that the value in a gas is four orders of magnitude greater than in a liquid, in this case.

2.1.1.1 Prediction of Diffusion Coefficient

Diffusion coefficients are functions of temperature, pressure and the species considered. Bird *et al*. (2007) note that kinetic theory models are sufficiently accurate for calculation of binary diffusion coefficients in gases at low pressure. By contrast, kinetic models are not accurate for prediction of liquid phase binary diffusion coefficients. As such, empirical correlations are often used. One such empirical correlation was developed by Wilke and Chang (1955) and is given below:

$$D_{AB} = 7.4 \times 10^{-8} \frac{\sqrt{\psi_B M_B} T}{\mu \tilde{V}_A^{0.6}} \quad \text{Equation 2.2}$$

An 'association parameter' is used, ψ_B, which takes a value of 2.6 for water. The molecular weight of species *B* M_B (g/mol), temperature *T* (K), solution viscosity μ (cp) and molar volume of species *A* as liquid at its normal boiling point $\tilde{V}_A$ (cm^3/gmol).

2.1.1.2 Experimental Measurement of Diffusion Coefficient

Diffusion is the mechanism for CO_2 transport most commonly studied in the available petroleum engineering literature, since it is the most relevant to subsurface applications. As noted above, only empirical correlations are reliable for the prediction of diffusion coefficients in liquids. Where more accurate values of the diffusion coefficient are required for specific systems and conditions, experimental work is usually conducted.

An experimental based study was completed by Bahar and Liu (2008) to measure the diffusion coefficient of CO_2 into brine at conditions relevant to the Otway Basin,

Australia. The application was CO_2 dissolution rates during injection for sequestration or flooding for enhanced oil recovery. An evacuated PVT cell was partially filled with synthetic 2% NaCl brine and pure CO_2 gas introduced at an initial pressure of 178bar absolute. The system was closed and a constant temperature of 356K maintained. The diffusion coefficient was inferred from pressure decay with respect to time. The calculation of the diffusion coefficient was split into two regions, one unsteady state and one steady state. In the steady state region, the diffusion coefficient was considered to be constant, whereas in the unsteady state region it was found to depend on parameters such as pressure, temperature, viscosity and molecular weights. An empirical correlation was proposed for this dependency. For the specific application considered, the unsteady state diffusion coefficient was between 4.5×10^{-8} m^2/s and 4.7×10^{-8} m^2/s.

When the magnitude of the reported diffusion coefficient is compared to that reported by Tamimi *et al*. (1994) or calculated via the correlation proposed by Wilke and Chang (1955), it is an order of magnitude greater. Bahar and Liu (2008) made no comparison between the experimental value and others available in the literature and no reasons for the apparent discrepancy were cited. However, the density of an aqueous system increases as CO_2 concentration increases according to Song *et al*. (2005). Increasing brine density at the phase interface can lead to natural convection currents and increase the CO_2 dissolution rate compared to molecular diffusion alone. Density driven convection may be the mechanism responsible in the Bahar and Liu (2008) experiments for the apparent acceleration of the mass transfer process relative to molecular diffusion.

2.1.2 Molecular Diffusion and Convection Governed Mass Transport

While Bahar and Liu (2008) did not explicitly acknowledge the effect of density driven convection, Yang and Gu (2006) conducted similar experiments and identified the two different mass transport mechanisms. Experiments were designed to measure the diffusion coefficient of CO_2 into brine at conditions relevant to the Instow oil field, Canada. A PVT cell was filled with pure CO_2 gas and the temperature allowed to equilibrate. A number of initial pressures, up to 75 bar absolute, were used. Actual reservoir brine was then injected via the bottom of the cell and the system subsequently closed. Constant temperatures of 300 K and 331 K were maintained in two sets of experiments. The diffusion coefficient was inferred from the subsequent pressure decay. An effective diffusion coefficient was defined to be a constant of proportionality in the same way as defined by Fick's law, Equation 2.1. However, it was recognized that this effective diffusion coefficient takes into account mass transfer by both diffusion and density driven convection. Reported values of the effective diffusion coefficient were between 1.707×10^{-7} m^2/s and 2.698×10^{-7} m^2/s, with the smaller value measured during an experiment at the smaller temperature and the larger value determined from an experiment at the greater temperature. The concept of effective diffusion coefficient proposed by Yang and Gu (2006) is simplification of the two processes and there is a critical limitation to its application. By combining the two mechanisms in one coefficient, the effect of geometry on the natural convection currents is not accounted for. As such, their reported values are only strictly applicable to a geometrically similar system, though they may still be a useful appropriate approximation for use in other systems.

Yang and Gu (2006) combined diffusion and density driven convection in one effective coefficient. Farajzadeh *et al*. (2009) conducted a number of similar experiments

and developed a theoretical model that includes the contribution of density driven convection in a rigorous manner. Experiments were conducted to measure the diffusion coefficient of CO_2 into distilled water. A PVT cell was partially filled with distilled water and pure CO_2 gas introduced at initial pressures of 10 bar absolute to 50 bar absolute. The system was closed and a constant temperature of 303 K maintained. The diffusion coefficient was inferred from pressure decay with respect to time. The model used to determine the diffusion coefficient included both diffusion according to Fick's first law, Equation 1, and density driven convection by solving the Navier – Stokes equations numerically via COMSOL. The diffusion coefficient reported was 2.0×10^{-9} m^2/s. The rigorous separation of diffusion and natural convection allows application to various geometries, where the effect of the second mechanism may be more or less pronounced. For comparison to the work of Yang and Gu (2006), Farajzadeh *et al*. (2009) calculated an effective diffusion coefficient by their approach and found the results obtained to be similar.

2.1.3 Mass Transfer Coefficient Governed Mass Transport

Farajzadeh *et al*. (2009) demonstrated the enhancement of mass transport due to density driven convection. When comparing effective diffusion coefficients to actual diffusion coefficients, there is a two order of magnitude increase when density driven convection plays a significant role. Clearly, in cases where the liquid phase is mixed, the mass transport occurs far more quickly than in the static case. A surface dissolution facility allows the brine to be mixed by mechanical agitation or other methods. With mixing present, the systematic spatial concentration gradient assumed in Fick's law, Equation 2.1, is removed and that relationship for mass flux no longer applies.

The mass transfer coefficient is a simplified method to describe the complex boundary condition involving macroscopic bulk fluid flow and microscopic molecular scale diffusion. An empirical relationship relates the mass flux to concentration difference as follows:

$$J = k_L\left(C_{A0} - C_{A\delta}\right) \quad \text{Equation 2.3}$$

with liquid phase mass transfer coefficient k_L (m/s), concentration of A at the phase boundary C_{A0} (mol/m^3) and concentration of A at the concentration boundary layer of thickness δ (m) C_A, (mol/m^3).

Of particular interest to this application is mass transfer into a turbulent liquid phase. By definition, turbulent flow consists of chaotically fluctuating velocities, or eddies. Accompanying these chaotic velocity fluctuations are concentration fluctuations. However, since the mass transfer coefficient is a macroscopic simplification of the process, C_{A^δ} (mol/m^3) can be considered the average concentration of A in the liquid phase. At a phase boundary, the flow is laminar and predictable. According to Bird *et al*. (2007) the phase compositions at the interface can be assumed to lie on the equilibrium curve. This allows C_{A0} (mol/m^3) to be equated to the saturation concentration of A $C_{Asaturation}$ (mol/m^3).

It should be noted that when considering gas to liquid mass transfer, there are in fact two mass transfer coefficients, one for the gas phase and one for the liquid phase. Bird *et al*. (2007) includes a detailed discussion on determining whether a process is liquid phase controlled or gas phase controlled. In the case of CO_2 dissolution into brine,

the process is liquid phase controlled or equivalently, the gas phase contribution to mass transfer resistance is negligible.

There have been a number of approaches taken to quantifying the relationship between k_L and D_{AB}. However, since the mass transfer coefficient includes the effects of bulk fluid flow, different hydrodynamic regimes lead to different mass transfer coefficients. It is possible to rigorously derive a relationship between the two for cases of laminar flow. An example of such a derivation in the case of mass transfer from a gas into a falling liquid film is provided by Treybal (1980). This will not be examined further since laminar flow is not relevant to the case of a process for CO_2 dissolution into brine using a surface mixing facility. There are a number of theories relating k_L and D_{AB} for turbulent flow. The earliest is the 'film theory' proposed by Lewis and Whitman (1924). The hypothesis was that there are two stagnant films at the gas and liquid interface, one in each phase. Since the films are stagnant, or free of convection, the mass transfer across them is governed by molecular diffusion. It follows from this model that k_L is linearly proportional to D_{AB}. Experimental evidence has since shown k_L to be proportional to a power, n, of D_{AB}. The value of n has been found experimentally to vary from near 0 to 0.9, according to Treybal (1980). Higbie (1935) proposed the 'penetration theory', which recognizes that there is not a stagnant film but rather a flow at the interface, or alternatively a surface renewal. A result from this theory is that k_L is linearly proportional to $D_{AB}^{0.5}$. There have been a number of other proposals, each with application and limitations. A model recently developed by Fernando *et al*. (2010) combined elements of both the film and penetration theories. A promising aspect of the model is its theoretical development rather than simply developing a correlation to a single dataset as many

researchers have done. Nonetheless, since so far the predictions from the model have been compared to only one dataset, its more general applicability remains to be seen.

It has not generally been possible to calculate a mass transfer coefficient without experimental data. However, some important results can be drawn from the dependencies discussed so far. The empirical relationship proposed by Wilke and Chang (1955) and the results of the film or penetration theories lead to some useful results. For a particular species pair, a greater T results in a greater D_{AB}. This is due to two terms present in the expression, a larger T in the numerator and smaller μ in the denominator. In turn, a greater D_{AB} results in a greater k_L, regardless of the value of n relevant to the particular application. This qualitative result is useful but accurate quantification of k_L still heavily relies on experimental data.

2.1.3.1 Volumetric Mass Transfer Coefficient

The discussion above has been in the context of molar flux J and not net molar rate n (mol/s) across an interface. The relationship between the two is simple, though separation is not always so. The net molar rate is a product of the molar flux and the area a (m^2) across which mass transfer occurs. This is shown below:

$$\frac{dn}{dt} = Ja \qquad \text{Equation 2.4a}$$

which in combination with the definition of mass transfer coefficient provided in Equation 2.3 produces the result:

$$\frac{dn}{dt} = k_L a\left(C_{A0} - C_{A\delta}\right) \qquad \text{Equation 2.4b}$$

The importance of this result is that experimentally molar fluxes are measured indirectly via net molar rates. It is common in chemical engineering literature to see the 'volumetric

mass transfer coefficient', k_La, reported rather than k_L itself. This is adequate for particular applications, but does limit the broader applicability of the data. Obviously to separate k_L from k_La requires accurate knowledge of a, which is often difficult to obtain.

Hill (2006) conducted experiments sparging CO_2 into well-mixed water and 2.85% NaCl solutions at ambient pressure and a number of temperatures, ranging from 288K to 313K. A number of different gas flowrates and mixing speeds were used. The application was CO_2 uptake by cell cultures and CO_2 concentration was inferred from pH measurements in the liquid phase. The results were presented as an empirical correlation for k_La as a function of temperature, gas flowrate and mixing speed. There was an increase in k_La for an increase in each of the independent variables studied. The temperature correlation is broadly applicable and expected, though the other two results are really only useful for other similar apparatus. Hill (2006) did notice a reduction in k_La for the 2.85% NaCl solution when compared to the water solution, but concluded that there was not statistical significance to the trend due to the scatter observed within the pure water experiments.

2.1.3.2 Prediction of Mass Transfer Coefficient for one System Using Data from Another

The combination of Wilke and Chang's empirical prediction of D_{AB} and penetration theory has been used by a number of authors to calculate k_L for one species using data from another. The calculation is made by assuming the linear proportionality of k_L to $D_{AB}^{0.5}$ predicted by the penetration theory and taking the ratio of predictions of D_{AB} for the two species. Examining Equation 2.2, it becomes apparent that this ratio is a function of the species' molar volumes at normal boiling point.

Boogerd *et al*. (1989) used this approach to calculate the k_La for CO_2 into a dilute aqueous solution of H_2SO_4 indirectly from experimental data for O_2 into dilute aqueous H_2SO_4. The O_2 experiments were conducted in a mixed vessel. The application motivating their work was the desulfurization of coal. There was no comparison made between the results calculated for CO_2 and any other source. Talbot *et al*. (1990) examined k_La for CO_2 into distilled water in a novel triangular reactor. They were particularly interested in experimental data specific to the particular project due to the unusual shape of the reactor used and the expected resultant case of less than ideal mixing. The temperature was maintained at 303 K and ambient pressure conditions prevailed. Three different gas flow rates and diffuser configurations were considered. Similarly to Boogerd (1989), the actual experimental gas used was O_2. Pauss *et al*. (1990) studied CO_2, H_2 and CH_4 dissolution in a number of different aqueous solutions, using three different reactors. The values of k_La for CH_4 were calculated from H_2 k_La values via the approach above, only to find disagreement with experimental data. As such caution is warranted in making calculations with such an approach.

2.1.3.3 Experimental Measurement of Mass Transfer Coefficient

Experimental investigations that quantify the interfacial area for mass transfer and therefore allow separation of k_L from k_La are rare. One such study, which examined the dissolution of N_2/CO_2 into aqueous solutions of $NaCO_3$ and NaOH, was undertaken by Maalej *et al*. (2003). Using a pressure reactor, the gas was sparged through the liquid phase, in a continuous flow arrangement. Experiments were run at a number of different pressures up to 50 bar and various gas flowrates. The same temperature of 293 K was used for all experiments. The interfacial area was determined indirectly from the model

adopted for the chemical reaction in the liquid phase. The values of k_L reported range from 1.4×10^{-4} m/s to 4.8×10^{-4} m/s, across different combinations of pressure and gas flowrate. k_L was determined to be independent of pressure. Oyevaar and Westerterp (1989) completed a thorough literature review of the influence of pressure on mass transfer phenomena in gas – liquid systems. Experimental studies of many different fluid systems over a range of temperatures and pressures to 100 bar were examined. Similarly to Maalej *et al*. (2003), they concluded that pressure had no effect on k_L.

Niranjan *et al*. (1988) and later Nigam *et al*. (1993) researched the mass transfer from a moving CO_2 elongated bubble or 'slug' into the surrounding liquid phase, water or a glycerol solution. The temperature and pressure were not explicitly stated in either paper. It is assumed that the temperature was ambient as no heating or cooling systems were mentioned. The pressure may have been larger than atmospheric due to the process of creating the CO_2 bubble, though since clear tubes were used and not pressure vessels, the pressure elevation must have been limited. Experiments were conducted in a number of different diameter pipes. The global k_La was determined from the pressure decline in the closed system due to the dissolution of CO_2 into the aqueous phase. The inter phase area was determined via photography. Niranjan *et al*. (1988) proposed a correlation for the Sherwood number with the Peclet number, while Nigam *et al*. (1993) demonstrated that different values of k_L were measured for different pipe diameters. The results of a number of experiments were values of k_L of 1.5×10^{-4} m/s to 6.0×10^{-4} m/s, with larger k_L values corresponding to larger pipe diameters. Larger values of k_L were observed where entrainment was present, that is development of small bubbles from the larger elongated bubble.

Vazquez *et al*. (1995) conducted experiments whereby a CO_2 gas stream was introduced over a water or aqueous surfactant solution liquid phase. The experiments were conducted at 293 K and atmospheric pressure. Low surface tension liquids were then deposited on the gas-liquid interface. Measurement of the induced surface velocity distribution via stroboscopic photography allowed the contribution of convection to be quantified analytically and compared to experimental values. Good agreement between the predicted and experimental values was found. For CO_2 dissolution into water with ethanol as the convection inducing liquid, experimental k_L values were from 1.08×10^{-4} m/s s to 1.23×10^{-4} m/s, with larger values of k_L corresponding to larger flowrates of ethanol. A correlation of the Sherwood number to the Reynolds number was determined.

Calderbank and Moo-Young (1961) measured k_L for the dissolution of a number of gases including O_2 and CO_2 into a variety of liquids, including water and brine. The gas was sparged through the liquid phase in sieve or sintered plate columns and in mixing vessels. The temperature was 298 K, though the operating pressure was not stated. The results indicate that agitation intensity and bubble free rising velocity had no effect on k_L. There were two distinct sets of results for k_L when examining bubble size, 'small' bubbles of less than approximately 2.5×10^{-3} m exhibited smaller values of k_L than 'large' bubbles of over approximately 2.5×10^{-3} m. However, within each class of bubbles there was no influence of bubble size on k_L, except within the transition zone between small and large bubbles. The authors attribute the difference to the difference in rigidity of the bubble surface, with small rigid bubbles and large more easily deformable bubbles. For CO_2 into water, k_L was reported to be 7.0×10^{-5} m/s to 8.0×10^{-4} m/s. Two distinct correlations for k_L are provided, one for each bubble class. Both correlations provided are a function of the

Schmidt number, density difference between the gas and liquid phase, liquid phase viscosity and liquid phase density.

Robinson and Wilke (1974) measured k_L for O_2 and CO_2 sparged into an aqueous solution of KOH. The temperature was 303 K, the pressure not specified. However, a Pyrex vessel was used, suggesting that the operating pressure would not have greatly exceeded ambient. For CO_2, a range of k_L from 1.37×10^{-4} m/s s to 2.28×10^{-4} m/s for stirrer speeds between 15.00 rev/s and 26.67 rev/s was reported. k_L was shown to decrease with increasing stirrer speed. Measurements of k_La were also presented and demonstrated that there was an increase in k_La with increasing stirrer speed, that is the increase in interfacial area was greater than the decrease in k_L, resulting in a larger product for a greater stirrer speed. When this was examined in detail, the authors were able to show a linear relationship between k_L and average bubble diameter. This result clearly contradicts that of Calderbank and Moo-Young (1961) where k_L was found to be independent of bubble size, within a particular bubble class, small or large.

2.1.3.4 Experimental Measurement of Mass Transfer Coefficient for CO_2 Disposal in Seawater

There has been some research completed into CO_2 dissolution into seawater, for application to ocean disposal of CO_2. The conditions for ocean disposal are large pressure, typically over 50 bar, and low temperature, less than 288K. Teng and Yamasaki (1998) conducted experiments where a stationary CO_2 drop was photographed as it dissolved into water at a number of large pressures and low temperatures. k_L was calculated from the drop shrinkage rate and found to be between 5.5×10^{-7} m/s to 7.0×10^{-7} m/s. Ogasawara *et al*. (2001), conducted similar experiments and found k_L to be between

1×10^{-7} m/s to 3×10^{-7} m/s, as read from a plot presented in the paper. A correlation with Reynolds number was found. All experiments were conducted at Reynolds numbers for pipe flow of less than 800. Reynolds numbers over 2300 are considered to be in the transition zone between laminar and turbulent flow. Clearly the experiments of Ogasawara *et al*. (2001) are in a laminar flow regime. Under some conditions CO_2 hydrate films have been known to form on the dissolving CO_2 drop. This hydrate film reduces k_L, as studied by Mori and Mochizuki (1996). Zhang *et al*. (2005) conducted experiments with a rising, rather than stationary, CO_2 drop that they claimed more realistically represented the particular application of CO_2 disposal to the ocean. k_L was calculated to be between 5.0×10^{-6} m/s and 2.0×10^{-6} m/s, for various conditions. These results are one order of magnitude larger than those determined from the stationary drop experiments of Teng and Yamasaki (1998) or Ogasawara *et al*. (2001).

Chapter 3: Results of Experiments

The kinetics data required to efficiently design a surface facility for the dissolution of CO_2 in brine were not available in the literature. To obtain these data, an experimental apparatus was designed, tested and used to conduct a series of batch experiments with a variety of brines at different conditions. The main components of the setup were a small stirred pressure reactor, syringe pump and accumulator. The mass transfer coefficient, k_L, was calculated from the final series of experiments and an empirical correlation developed as a function of the temperature, wet CO_2 density and brine salinity.

The experimental apparatus was designed to bring CO_2 into contact with a well-mixed brine while maintaining a closed system at isothermal conditions and with a quantifiable interfacial area between bulk phases. This allowed k_L, as defined in Equation 2.4b, to be calculated from the pressure decrease observed with respect to time. The pressure decrease was a result of the system moving from two relatively pure phases to two mixed bulk phases in thermodynamic equilibrium.

3.1 Models Used

Several models were used in the various calculations made from experimental data. The Peng-Robinson equation of state was used for vapor phase volumetric calculations and flash calculations, after being tuned to experimental data for CO_2 solubility in NaCl and $CaCl_2$ brines. The liquid density model of Li *et al*. (2011) was used for calculation of the aqueous phase density.

3.1.1 Peng-Robinson Equation of State

An equation of state (EOS) provides a quantitative prediction of the volumetric behavior of a fluid, that is, a relationship between T, P and molar volume V (dm^3/mol). The Peng-Robinson (PR) EOS was developed by modifying the attractive pressure term of the semi-empirical van der Waals equation (Peng and Robinson, 1976). When applied to binary, ternary or multi-component systems, the PR EOS can be used for both phase and volumetric behavior. For a system with any number of components, the PR EOS is as follows:

$$P = \frac{RT}{V-b} - \frac{a\alpha}{V^2 + 2bV - b^2} \qquad \text{Equation 3.1a}$$

with a repulsion term a, temperature dependent function α, and attraction parameter b. For a single component system or a single component of a binary, ternary or multi-component system, each is defined below:

$$a = \frac{0.457235R^2T_c^2}{P_c} \qquad \text{Equation 3.1b}$$

$$b = \frac{0.077796RT_c}{P_c} \qquad \text{Equation 3.1c}$$

$$\alpha = \left(1 + \kappa\left(1 - T_r^{0.5}\right)\right)^2 \qquad \text{Equation 3.1d}$$

with a quadratic function κ, of the acentric factor ω. The equation for κ is shown in Equation 3.1e. The reduced temperature is T_r (K) and given by Equation 3.1f.

$$\kappa = 0.37464 + 1.54226\omega - 0.26992\omega^2 \qquad \text{Equation 3.1e}$$

$$T_r = \frac{T}{T_c} \qquad \text{Equation 3.1f}$$

where the critical temperature is T_c (K).

In a multi-component system, Equation 3.1a can be applied, though a, α and b are calculated for the phase and are therefore a function of all of the constituent components

of the phase. For a liquid phase the notation $a\alpha^L$ and b^L are used, whereas for a vapor phase $a\alpha^V$ and b^V are used. The van der Waals mixing rule for $a\alpha^L$ is given below:

$$a\alpha^L = \sum_{i=1}^{N_c}\sum_{j=1}^{N_c} x_i x_j (a\alpha)_{ij} \qquad \text{Equation 3.1g}$$

where:

$$(a\alpha)_{ij} = (1-\delta_{ij})\sqrt{(a\alpha)_i (a\alpha)_j} \qquad \text{Equation 3.1h}$$

with the liquid phase mole fraction of a component i and component j, x_i and x_j, respectively. The binary interaction parameter, δ_{ij} , is used to adjust the interactions between unlike components (Johns, 2010). In some literature δ_{ij} is termed the coupling parameter (Kwak and Mansoori, 1985). The van der Waals mixing rule for b^L is given below:

$$b^L = \sum_{i=1}^{N_c} x_i b_i \qquad \text{Equation 3.1i}$$

Analogous equations are used for the vapor phase calculations $a\alpha^V$ and b^V, where the liquid phase mole fractions x_i and x_j are replaced by the vapor phase mole fractions y_i and y_j.

Other mixing rules have been proposed, such as those proposed by Wong and Sandler (1992). The Wong-Sandler mixing rule uses a Helmholtz free energy term to ensure consistency with a requirement of statistical mechanics. The application of this alternative mixing rule to the CO_2 and H_2O system was discussed by Shyu *et al*. (1996). There may be improvements in accuracy from using the Wong-Sandler rules in place of the van der Waals rules. However, for the range of T and P relevant to this application, the van der Waals rules are sufficiently accurate. This is demonstrated by comparison to experimental data in section 3.1.1.1 'Volumetric Data Comparison'.

3.1.1.1 Volumetric Data Comparison

To check the accuracy of the PR EOS calculation of vapor phase volumetric data, reference data were obtained from the 'Thermophysical Properties of Fluid Systems' calculator on the National Institute of Standards and Technology (NIST) website (NIST, 2012). This calculator uses the most accurate EOS particular to each of the available species. For CO_2, the EOS used was developed by Span and Wagner (1996) and covers the *T* range from the triple point to 1100 K and *P* up to 8000 bar. For comparison, data from 298 K to 373 K and 5 bar to 100 bar were used. Figure 3.1 shows the percentage difference in *V* between the reference data and that calculated using the PR EOS.

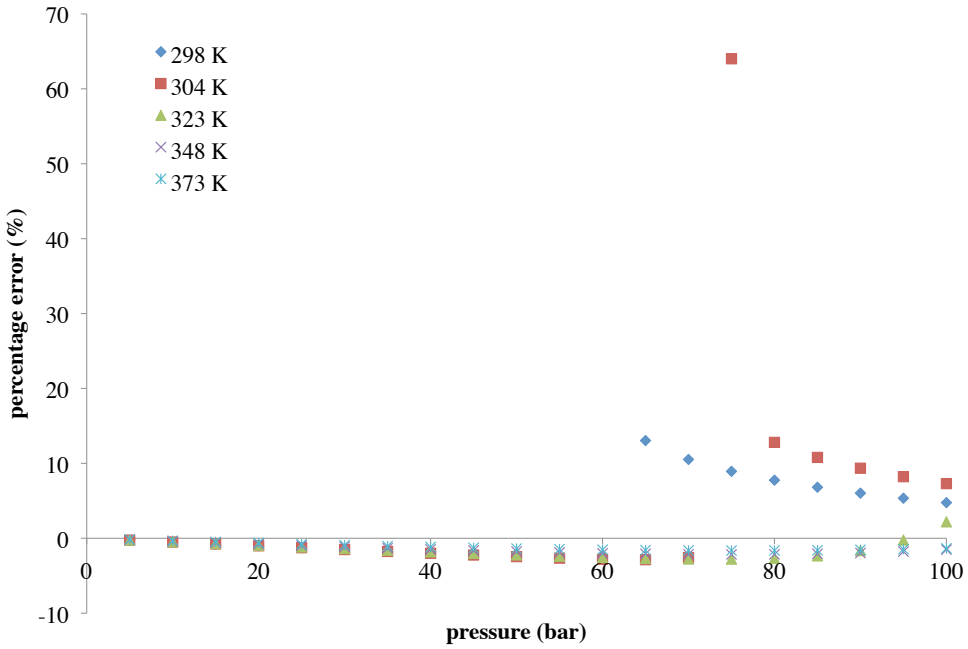

Figure 3.1: Percentage difference in *V* between reference data and PR EOS

The NIST website (see URL in 'Bibliography') provides data for components but not data for mixtures. However, the CO_2 and H_2O vapor phase under consideration is CO_2

rich across the range of T and P conditions of interest. For greater T, y_{H2O} increases, but even at the largest T of interest, 373 K, y_{H2O} is only 0.025. Since y_{H2O} is small in comparison to y_{CO2}, it was assumed that the volumetric behavior is dominated by CO_2 and that a comparison between the PR EOS calculation and reference data for pure CO_2 represents the accuracy of the PR EOS calculation for the CO_2 and H_2O vapor phase.

The comparison presented in Figure 3.1 shows that the accuracy of the PR EOS for CO_2 is quite good for most T and P conditions considered. However, it is very poor close to the critical point, 304.1 K and 73.8 bar, where there is a 64% discrepancy. It is also less accurate for liquid phase CO_2 and supercritical phase CO_2 at T_c. For this reason and another, the rapid change in P with respect to T of incompressible systems, experiments were not run at these conditions. Figure 3.2 presents the same comparison with a smaller percentage difference scale.

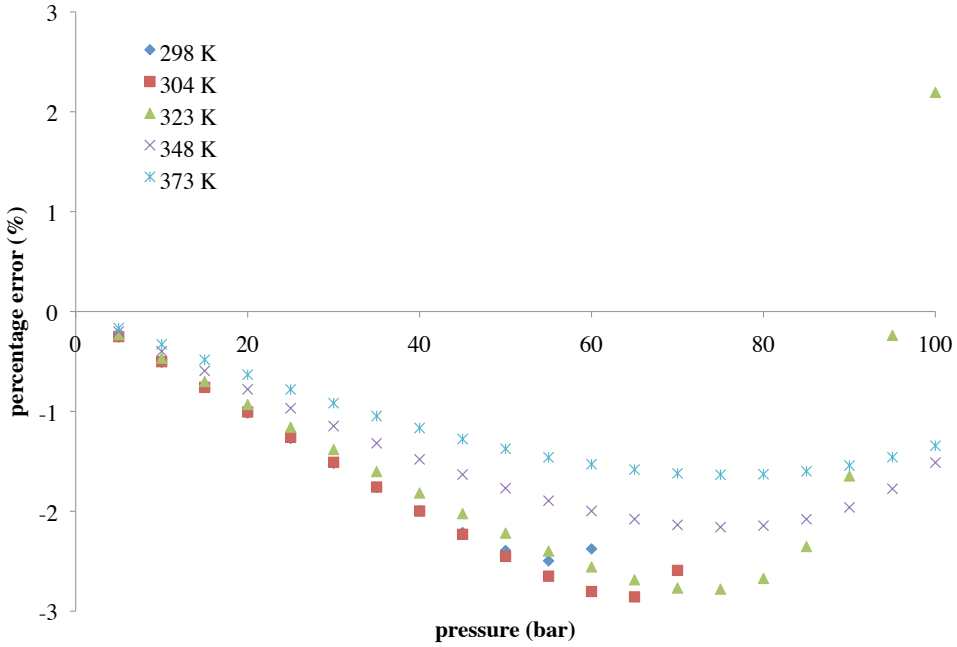

Figure 3.2: Percentage difference in V between reference data and PR EOS, plotted with a smaller percentage difference scale

Figure 3.2 shows that for vapor phase CO_2 and supercritical phase CO_2 above T_c, the accuracy is within 3%.

3.1.1.2 Flash Calculation

For two or more phases in thermodynamic equilibrium, a flash calculation allows the calculation of x_i, y_i and the mole fraction of each phase, n_L for the liquid phase and n_V for the vapor phase. In this application only two-phase equilibrium is of interest. The input to this calculation is T, P and the overall mole fractions of each component, z_i.

The CO_2 and synthetic brine system used for experiments was composed of CO_2, H_2O, NaCl and $CaCl_2$. Since the PR EOS was not developed for electrolytes, this system was simplified to a binary CO_2 and H_2O system. To account for the reduction in CO_2 solubility associated with an increase in temperature and salinity, a function was developed for $\delta_{CO_2-H_2O}$ that depends on these variables. Thus for a flash calculation, the NaCl salinity and $CaCl_2$ salinity, S_{NaCl} (m) and S_{CaCl2} (m), respectively, must be specified.

The fundamental requirement of thermodynamic equilibrium is equal component fugacity, f_i (bar), in each phase (Sandler, 2006). To solve for the equilibrium phase compositions and n_L, the process flow chart shown in Figure 3.3, below, was used.

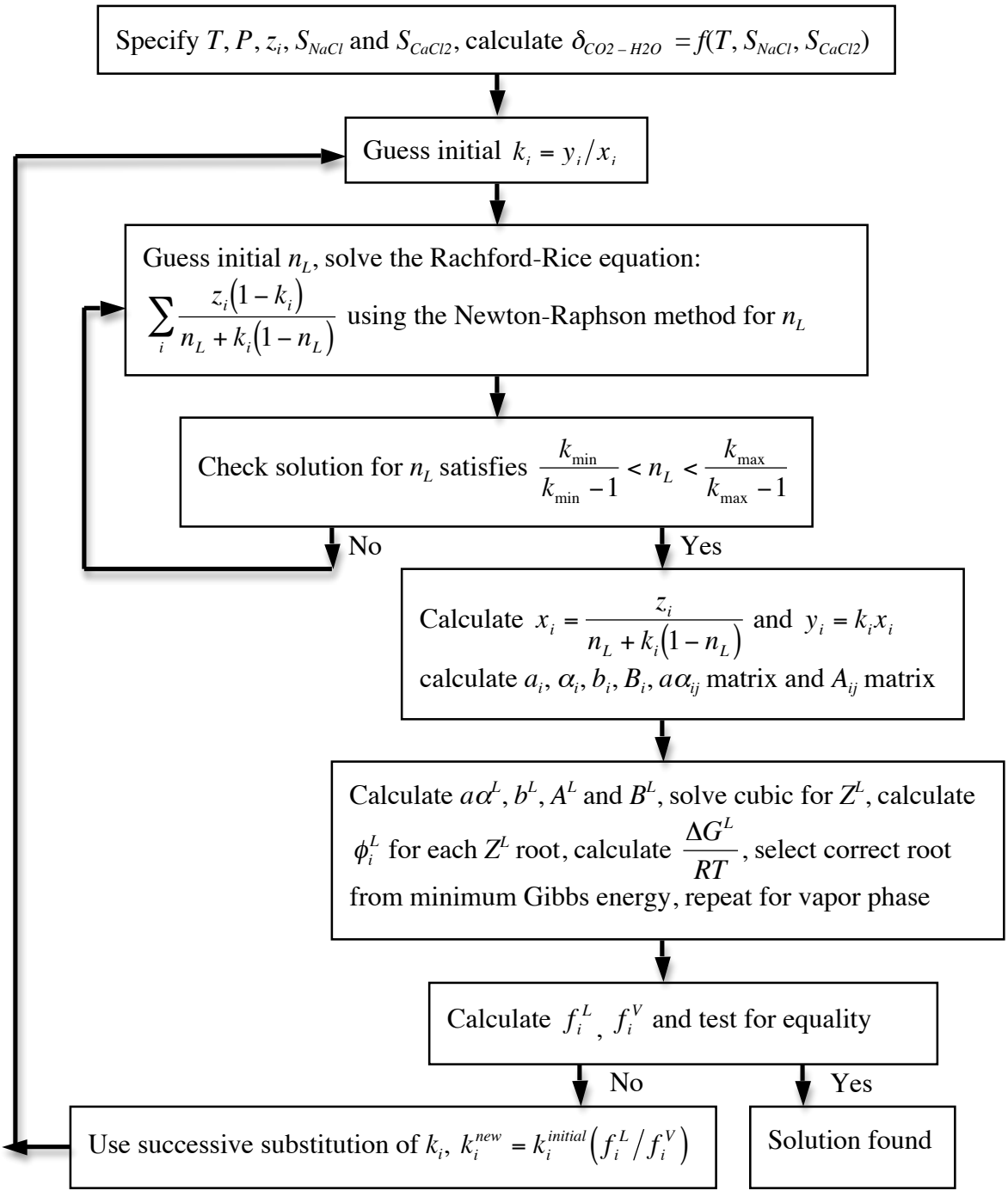

Figure 3.3: Process flow chart for PR EOS flash calculation

In Figure 3.3 the ratio of y_i to x_i is k_i and A and B are defined below:

$$A = \frac{a\alpha P}{R^2T^2} \qquad \text{Equation 3.1j}$$

$$B = \frac{bP}{RT} \qquad \text{Equation 3.1k}$$

which are used to simplify the cubic equation in compressibility factor, Z. The cubic is as follows:

$$Z^3 - (1-B)Z^2 + \left(A - 2B - 3B^2\right)Z - \left(AB - B^2 - B^3\right) = 0 \qquad \text{Equation 3.1l}$$

Compressibility factor is defined by:

$$Z = \frac{PV}{RT} \qquad \text{Equation 3.1m}$$

The component fugacity coefficient, , is defined by:

$$\phi_i = \frac{f_i}{P} \qquad \text{Equation 3.1n}$$

Finally:

$$\frac{\Delta G}{RT} = \sum_i^{N_c} x_i \ln\left(\frac{\phi_i^{\max}}{\phi_i^{\min}}\right) \qquad \text{Equation 3.1o}$$

with Gibbs energy, G. $\phi_i^{\max}$ and $\phi_i^{\min}$ are used to denote the component fugacity coefficients using the large and small roots of Z, respectively.

3.1.1.3 Flash Calculation Tuning

As noted above, the reduction in CO_2 solubility associated with an increase in temperature and salinity was accounted for by developing a function for $\delta_{CO_2-H_2O}$ in T, S_{NaCl} and S_{CaCl2}. To develop this function, experimental data on the CO_2 solubility in pure water, NaCl and $CaCl_2$ brines were collated. A similar approach was adopted by Kumar (2004), though a relatively small set of experimental data were used. Since the solubility model is of critical importance to the k_L calculation, the new model was developed using a larger set of data. Akinfiev and Diamond (2010) examined 21 publications of

experimental data for CO_2 solubility in aqueous NaCl solutions and rated each in terms of consistency with thermodynamic principles, assigning an assessment of reliability from poor to high. Data of high reliability in the *T* and *P* range of interest were selected. Data from the publications included in Table 3.1 were selected for tuning and comparison.

Author	*T* (K)	*P* (bar)	S_{NaCl} (m)	S_{CaCl2} (m)
Wiebe and Gaddy (1939)	323 to 373	25 to 710	0	0
Wiebe and Gaddy (1940)	285 to 313	25 to 510	0	0
Matous *et al*. (1969)	303 to 353	9 to 38	0	0
King *et al*. (1992)	288 to 313	60 to 250	0	0
Bamberger *et al*. (2000)	313 to 353	40 to 130	0	0
Malinin and Savelyeva (1972)	298 to 348	48	0 to 4.5	0 to 3.9
Malinin and Kurovskya (1975)	298 to 423	48	0 to 6	0 to 6
Rumpf *et al*. (1994)	348 to 394	10 to 700	0 to 6	0

Table 3.1: Published sources of experimental CO_2 solubility in brine

The first step to develop the function for $\delta_{CO_2-H_2O}$ was to quantify the dependence on *T* for pure water. Figure 3.4 shows the data used.

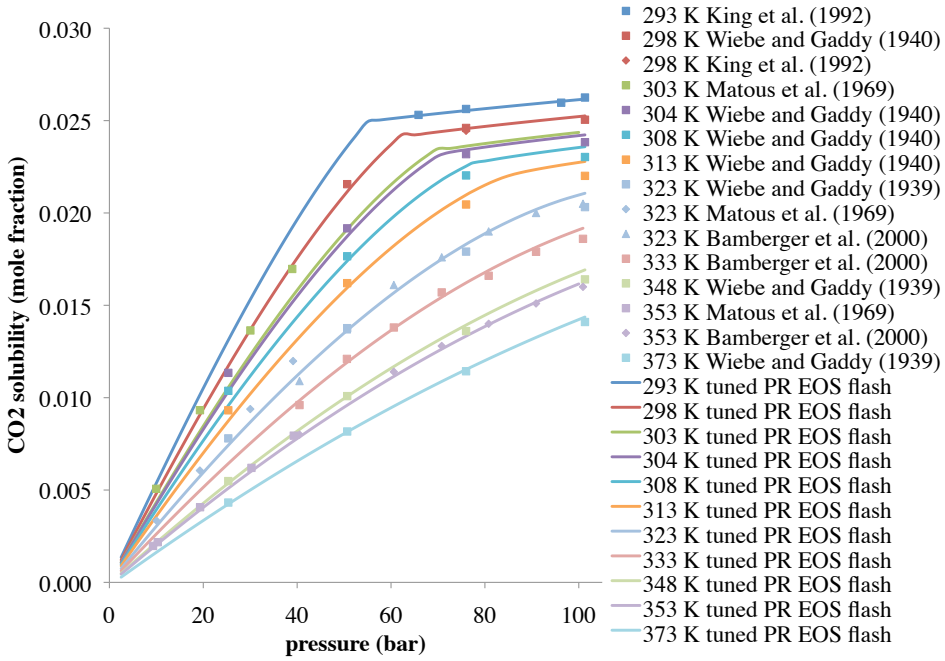

Figure 3.4: CO_2 solubility versus P, experimental data (discrete markers) and tuned PR EOS flash (continuous curves)

The $\delta_{CO_2-H_2O}$ that best matched the data of King *et al*. (1992) at the small end of the T range, 293 K, was found by manual iteration. A similar exercise was carried out to match the data of Wiebe and Gaddy (1939) at the large end of the T range, 373 K. With the endpoint values of $\delta_{CO_2-H_2O}$ established, a linear function was developed. The function is:

$$\delta_{CO_2-H_2O} = 0.00102(T - 293.15) - 0.1229 \qquad \text{Equation 3.2}$$

The remaining experimental data were not used in tuning $\delta_{CO_2-H_2O}$, but were matched very well by the tuned PR EOS flash as shown in Figure 3.3. Comparing the match between the tuned PR EOS flash and experimental data, 55 out of 66 data points were matched within 5%, 9 data points were within 5% to 10% and 2 data points were within 10% to 15%.

Examining Figure 3.4 in the range of T less than T_c = 304 K, there is a noticeably different trend for CO_2 solubility below P_c = 73.8 bar when compared to that evident above P_c. There is a larger increase in CO_2 solubility with increasing P where CO_2 is gas phase than where it is liquid phase. This results in the noticeable 'kinks'. By contrast, in the range of T greater than T_c, there is a smooth trend for CO_2 solubility increase with P below P_c and above P_c. There is a slightly larger increase in CO_2 solubility with increasing P for CO_2 in gas phase compared to supercritical phase, though the transition is not marked as it is for the gas to liquid phase transition at lower T.

The second step to develop the function for $\delta_{CO_2-H_2O}$ was to quantify the dependence on S_{NaCl} and S_{CaCl2}. The experimental data for NaCl and $CaCl_2$ of Malinin and Saveleya (1972) and Malinin and Kurovska (1975) were selected to tune to. Figure 3.5 shows the results of tuning to the data of Malinin and Savelyva (1972).

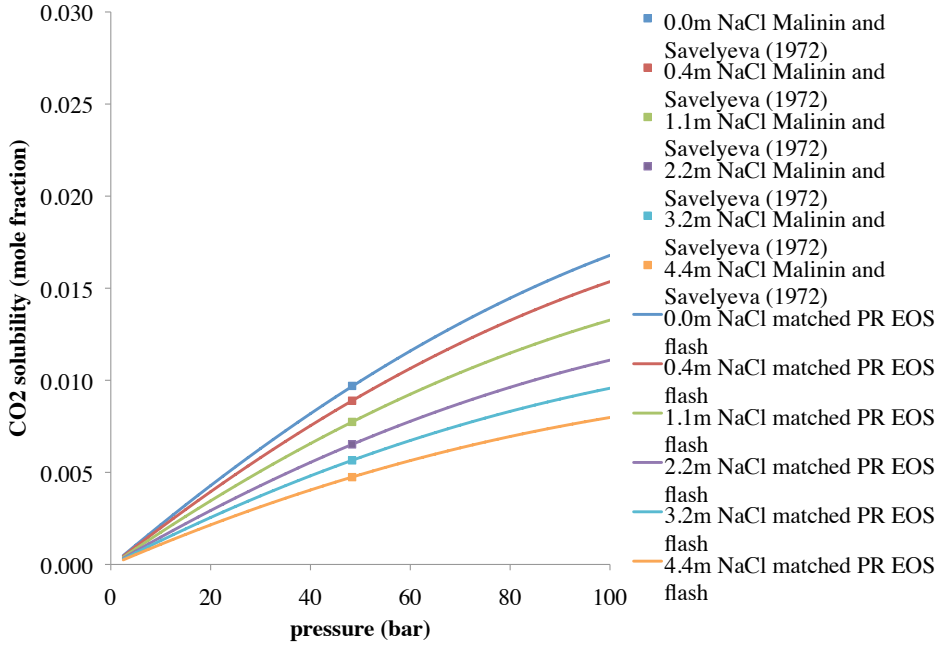

Figure 3.5: CO_2 solubility versus P, results of tuning the PR EOS to the NaCl brine data of Malinin and Savelyva (1972)

By subtracting the $\delta_{CO_2-H_2O}$ calculated by Equation 3.2 from the values required to match each data point, the S_{NaCl} dependency was established. This term is referred to as the $+BIP$. These values are plotted in Figure 3.6, below.

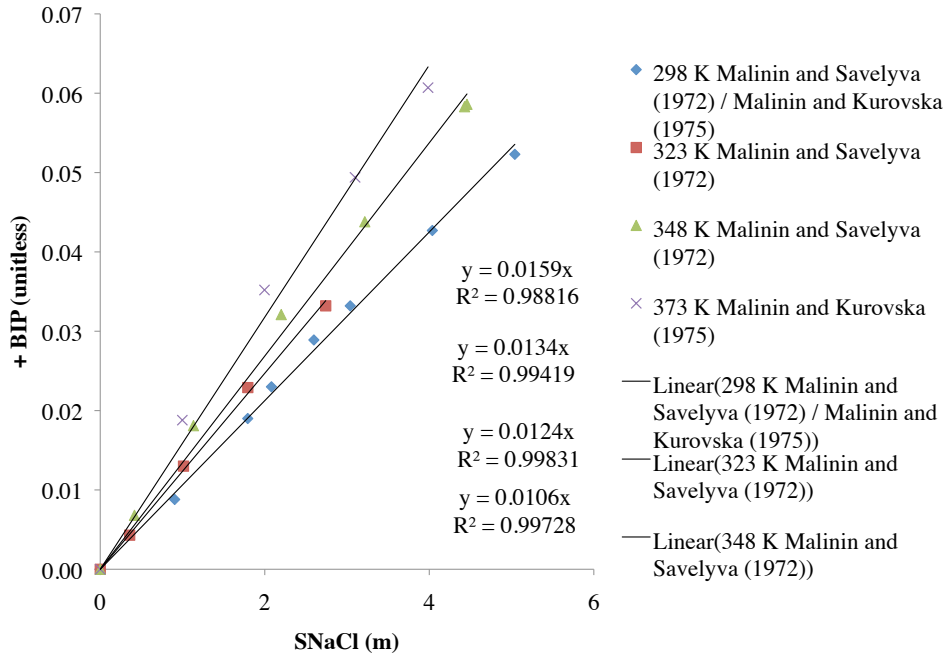

Figure 3.6: $+BIP$ versus S_{NaCl} for tuning data

It is apparent from Figure 3.6 that not only does the binary interaction parameter depend on S_{NaCl}, but that this dependency varies with T. The $+BIP$ term was found not be linear with S_{NaCl} for very large salinity brines, those approaching 6 m. The range of interest is to 4 m and a linear fit was determined to be sufficient in this range. The slope m of linear trend-lines that were fitted to the $+BIP$ versus S_{NaCl} was plotted versus T in Figure 3.7, below.

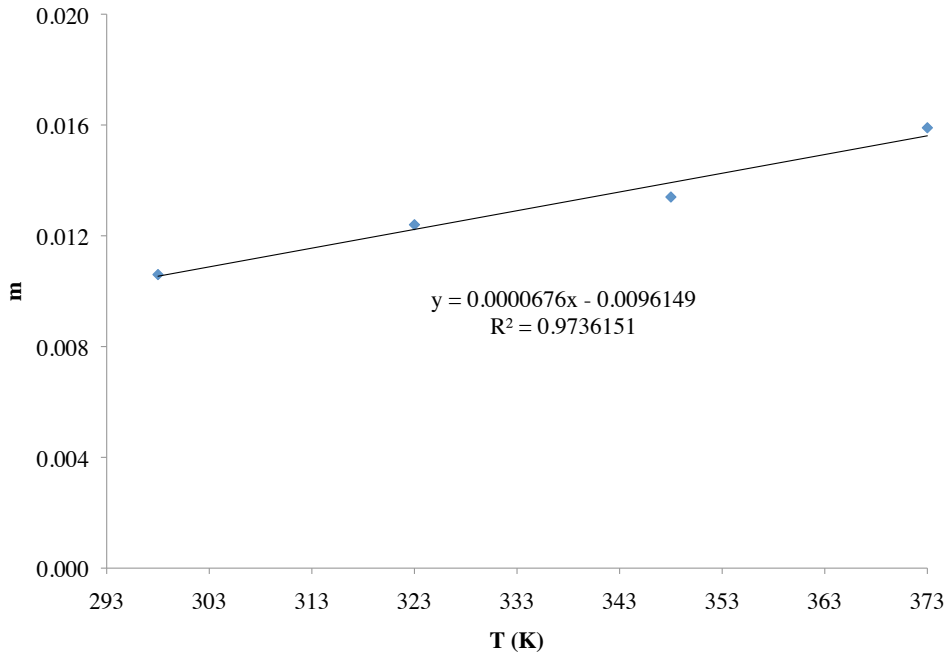

Figure 3.7: *m* versus *T* for NaCl brines

From the trend-line fits, an S_{NaCl} and *T* dependent function for the term $+BIP$ was established. This is shown in Equation 3.3.

$$+BIP_{NaCl} = S_{NaCl}\left(0.0000676\left(T - 293.15\right) + 0.010202\right) \qquad \text{Equation 3.3}$$

This function is added to the base *T* dependency given in Equation 3.3 and equals zero for pure H_2O, preserving the base *T* dependency. A similar procedure was followed for the solubility reduction due to S_{CaCl2}. The plots for tuning to the solubility data for $CaCl_2$ brines are shown in Appendix A. It was noted by Malinin and Savelyva (1972) that the solubility reduction due to the addition of NaCl and $CaCl_2$ is additive. This allows the following function for $\delta_{CO_2-H_2O}$ to be used:

$$\delta_{CO_2-H_2O} = 0.00102\left(T - 293.15\right) + BIP_{NaCl} + BIP_{CaCl_2} - 0.1229 \qquad \text{Equation 3.4}$$

with the $+BIP$ for $CaCl_2$ given by:

$$+BIP_{CaCl_2} = S_{CaCl_2}\left(0.0001496\left(T - 293.15\right) + 0.020542\right) \quad \text{Equation 3.5}$$

The accuracy of the function developed was compared to the data of Rumpf *et al.* (1994), among others. An example of the comparison made for 4 m NaCl over a range of T and P is presented in Figure 3.8.

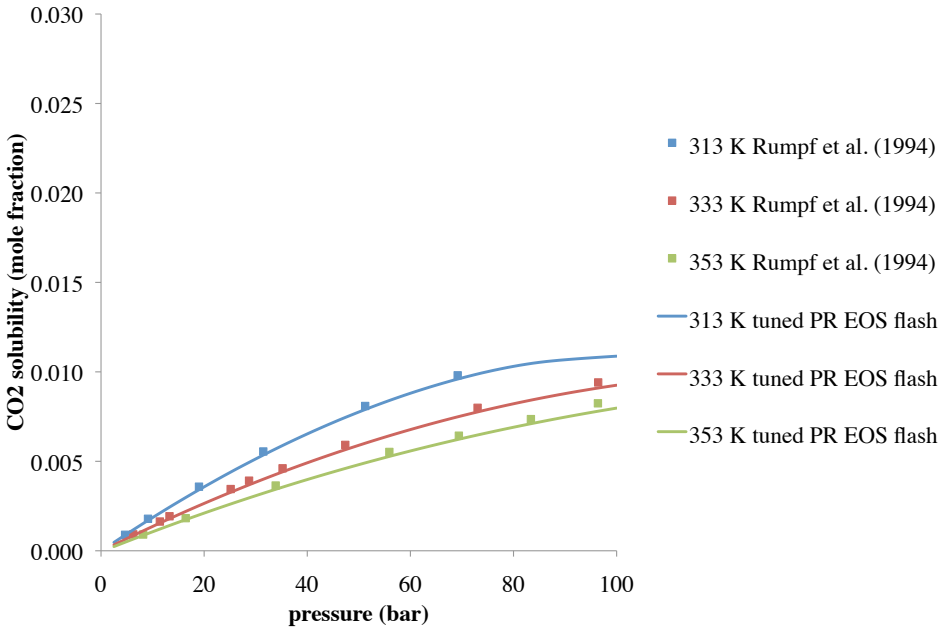

Figure 3.8: Comparison between the tuned PR EOS flash calculation and the experimental data of Rumpf et al. (1994) for 4 m NaCl solutions

The comparison made in Figure 3.8 shows good agreement across the range of P and T. When examining the match to all NaCl and $CaCl_2$ brine data considered, that is $S >$ 0 m, 49 of the 59 data points were matched within 5% and 10 data points were within 5% to 10%.

3.1.1.4 Tuned Flash Calculation Comparison to Existing Model

Duan and Sun (2003) developed a model for the calculation of CO_2 solubility in pure H_2O and aqueous NaCl solutions. Their model is valid across a range of *T* from 273 K to 533 K and *P* to 200 bar. Specific particle interaction theory was used to develop the model, allowing it to be applied to $CaCl_2$ systems with the salinity expressed in terms of ionic strength, according to Duan and Sun (2003). As would be expected to accurately match data across a larger parameter space, more fitting parameters are used by the Duan and Sun model than were necessary to tune the PR EOS flash. A virial expansion was used for each of three parameters, where each expansion contains eleven coefficients. A number of these coefficients are zero, but twenty are non-zero. In comparison, the tuned PR EOS flash uses six coefficients. A comparison was made between the tuned PR EOS flash and the Duan and Sun model for pure H_2O, shown in Figure 3.9.

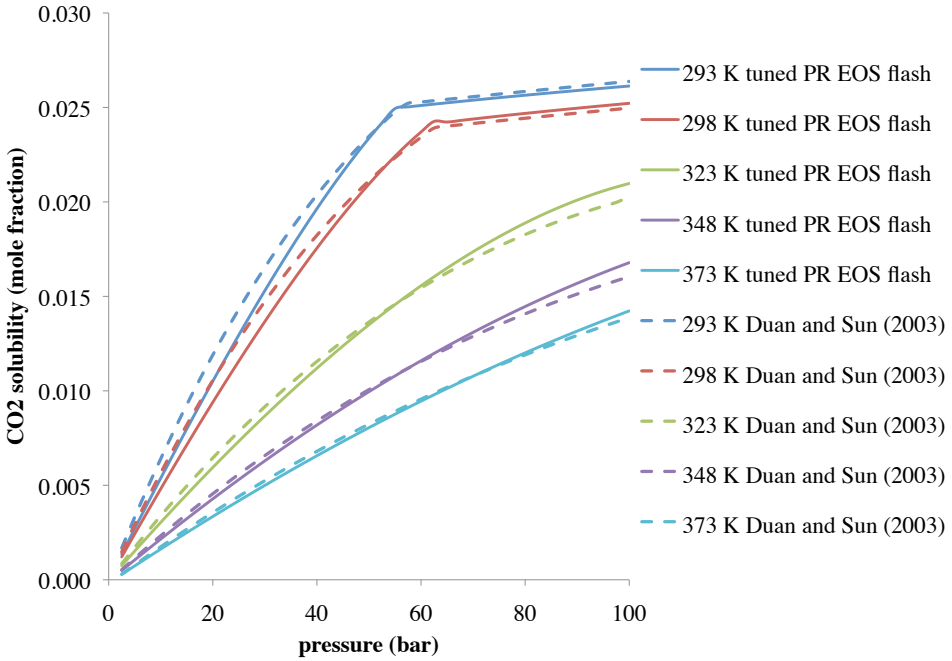

Figure 3.9: Comparison between the tuned PR EOS flash and the Duan and Sun (2003) model, for pure H_2O

The match between the two models is quite good across the range of T and P considered. A comparison was made for 4 m NaCl and is shown in Figure 3.10, below.

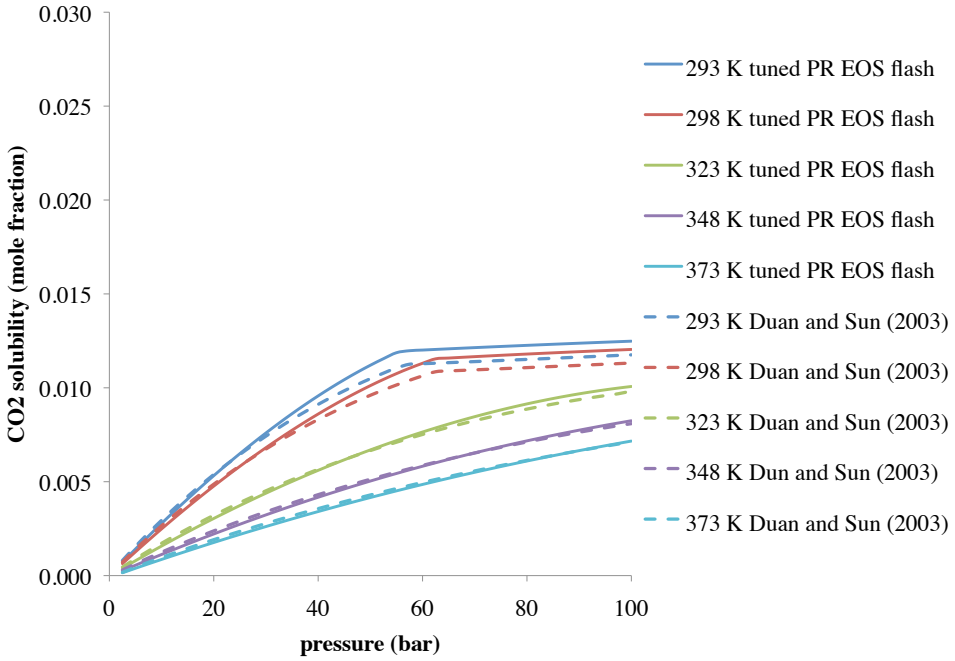

Figure 3.10: Comparison between the tuned PR EOS flash and the Duan and Sun (2003) model, for 4 m NaCl aqueous solutions

As for the pure H_2O case, the match for 4 m NaCl aqueous solutions is good across the range of T and P. When comparing Figure 3.9 and Figure 3.10, it is apparent that there is a considerable reduction in CO_2 solubility due to salinity across the entire T and P parameter space of interest. Comparisons for aqueous solutions of 0.5 m NaCl and 1.5 m NaCl are included in Appendix B.

3.1.2 Liquid Density Model

The PR EOS was not developed for use with electrolytes. The density of brine with a large value of S_{NaCl} or S_{CaCl2}, compared to that of pure H_2O is considerably larger. Using the data of Bourgoyne *et al*. (1986) for brines at atmospheric P and T of 341 K, the density of brine with S_{NaCl} of 4.3 m is 15% greater than that of pure H_2O at the same conditions. Clearly a model that includes the effect of electrolytes is necessary for accurate density prediction. Dissolved CO_2 in brine also increases its density.

The model proposed by Li *et al*. (2011) allows calculation of the density of an aqueous phase containing CO_2, H_2O and NaCl. The applicable range is 273 K to 573 K, 0.001 bar to 1000 bar and 0 m to 6 m NaCl. Using this model, in conjunction with a formulation of Mao and Duan (2008) for the density of the binary H_2O and NaCl and binary H_2O and $CaCl_2$ systems, the density of solutions of CO_2, H_2O, NaCl and $CaCl_2$ were calculated. The density calculation of the binary H_2O and NaCl as well as H_2O and $CaCl_2$ systems is, in turn, based on a density model for pure H_2O, the International Association for the Properties of Water and Steam Industrial Formulation (IAPWS-IF97).

The IAPWS-IF97 is valid over the T range 273 K to 1073 K for P < 1000 bar and from T of 1073 K to 2273 K for P < 500 bar. The T and P parameter space is divided into a number of regions. Of interest in this application is region 1, from T of 273 K to 623 K and at P over that of the saturation curve. In region 1, a fundamental equation for the Gibbs free energy, g, is provided in dimensionless form. Many thermodynamic properties can be calculated from the fundamental equation, such as specific volume, specific

internal energy and specific entropy, among others. Using the original notation as it appears in IAPWS-IF97, the equation is:

$$\frac{g(pT)}{RT} = \gamma(\pi,\tau) = \sum_{i=1}^{34} n_i (7.1-\pi)^{I_i} (\tau - 1.222)^{J_i} \qquad \text{Equation 3.6a}$$

where $\pi = p/p^*$ and $\tau = T^*/T$ with $p^* = 165.3$ bar and $T^* = 1386$ K. The coefficients n_i and exponents I_i and J_i are provided. By definition, the specific volume:

$$v = \left(\partial g/\partial p\right)_T \qquad \text{Equation 3.6b}$$

Mao and Duan (2008) developed a density model for binary aqueous chloride solutions up to T of 573 K and P of 1000 bar. The systems covered are H_2O and LiCl, NaCl, KCl, $MgCl_2$, $CaCl_2$, $SrCl_2$ and $BaCl_2$. Of interest in this application are NaCl and $CaCl_2$. To calculate the density for a particular solution, the solution volume at reference molality, $V(m_r)$, as well as the second and third virial coefficients, B_V and C_V respectively, are calculated from functions of T and P using the following equations:

$$V(m_r) = c_1 + c_2 T + c_3 T^2 + c_4 T^3 + P\left(c_5 + c_6 T + c_7 T^2 + c_8 T^3\right) \qquad \text{Equation 3.7a}$$

$$B_V = \frac{c_9}{T-227} + c_{10} + c_{11} T + c_{12} T^2 + \frac{c_{13}}{647-T} + P\left(\frac{c_{14}}{T-227} + c_{15} + c_{16} T + c_{17} T^2 + \frac{c_{18}}{647-T}\right)$$

Equation 3.7b

$$C_V = \frac{c_{19}}{T-227} + c_{20} + c_{21} T + c_{22} T^2 + \frac{c_{23}}{647-T} \qquad \text{Equation 3.7c}$$

The coefficients c_1 to c_{23} are unique to each binary system.

Using $V(m_r)$, B_V and C_V, along with the pure H_2O density, ρ_{H2O} (g/cm^3), calculated from IAPWS-IF97, the binary system density, ρ_{sol} (g/cm^3) is calculated with Equation 11d.

$$\frac{1000 + mM_s}{m\rho_{sol}} = \frac{V(m_r)}{m_r} + \frac{1000}{\rho_{H_2O}}\left(\frac{1}{m} - \frac{1}{m_r}\right) + v|z_+ z_-|A_V\left[h(I_m) - h\left(I_{m_r}\right)\right]$$
$$+2 v_+ v_- RT\left[B_V(m - m_r) + v_+ z_+ C_V\left(m^2 - {m_r}^2\right)\right] \qquad \text{Equation 3.7d}$$

with the molality of salt, m (mol/kg) and molar mass of chlorides M_s (g/mol). The charge

of anion and cation are z_+ and z_-, respectively. The number of anion and cation charges are v_+ and v_-, respectively. The sum of v_+ and v_- is v. The volumetric Debye-Huckel limiting law slope is A_V. The ionic strength is I and the function of I, $h(I)$ is given in Equation 3.7e.

$$h(I) = \frac{\ln\left(1 + bI^{0.5}\right)}{2b} \qquad \text{Equation 3.7e}$$

with b a constant equal to 1.2 $kg^{0.5}/mol^{0.5}$.

The calculation of A_V requires calculation of the dielectric constant of pure H_2O, which is done using the equation of Bradley and Pitzer (1978).

In this application, small $CaCl_2$ salinities were used (0.2 m). $CaCl_2$ was one component of the two-salt brine used, the other salt being NaCl. To calculate the density of the two-salt brine, the density increase of 0.2 m $CaCl_2$ brine was compared to that of pure H_2O at the T and P of interest, using the formulations of Mao and Duan (2008) and IAPWS-IF97. The density increase was small, in all cases less than 2%. The density increase was applied to the calculated NaCl brine density, in cases where $CaCl_2$ was present. This simple model was compared to a sample of experimental data measured in this research and found to be accurate.

The model of Li *et al*. (2011) relies on the calculation of the density of a component of a mixture, as the binary model of Mao and Duan (2008) used a pure component model of IAPWS-IF97; it also relies upon republishing the previously available model of Duan *et al*. (2008) for the perturbation of the density of a binary H_2O and NaCl brine by the addition of CO_2. Where the model of Duan *et al*. (2008) for a CO_2, H_2O and NaCl system used the model of Rogers and Pitzer (1982) for the calculation of

the binary H_2O and NaCl system density, Li *et al*. (2011) uses the model of Mao and Duan (2008). The main development of the model of Mao and Duan (2008) over that of Rogers and Pitzer (1982) is its applicability to many aqueous chloride systems, as discussed above, rather than only H_2O and NaCl. As a result, the original contribution of Li *et al*. (2011) is small compared to that of Duan *et al*. (2008).

The model of Li *et al*. (2008) presents a density perturbation of the binary H_2O and NaCl system, K:

$$K = a_1T^2 + a_2T + a_3 + a_4T^{-1} + a_5T^{-2} + \left(a_6T^2 + a_7T + a_8 + a_9T^{-1} + a_{10}T^{-2}\right)P \quad \text{Equation 3.8a}$$

with a_1 to a_{10} provided.

The density of the CO_2, H_2O and NaCl system is then given by:

$$\rho = \left(1000 + 58.4428m_{NaCl} + 44.0098m_{CO_2}\right) \Big/ \left(\frac{1000 + 58.4428m_{NaCl}}{\rho_B} + \frac{18.0153(1+K)m_{CO_2}}{\rho_W}\right)$$

Equation 3.8b

with the molality of NaCl and CO_2 in solution m_{NaCl} and m_{CO2}, respectively. The density of NaCl brine is ρ_B (g/cm^3), whereas the notation ρ_{sol} was used in Equation 3.7d. The density of pure H_2O from IAPWS-IF97 is ρ_W (g/cm^3).

3.2 Calculation of Expected Pressure Drop

Before conducting experiments to quantify the kinetics of CO_2 dissolution into brine, the expected P drop between initial conditions, P^o (bar), and equilibrium, $P^{equilibrium}$ (bar), was calculated. This calculation was primarily made to see if the expected result would be sufficiently large to be measured. Secondly, the calculation was performed to understand the effect of various z_{CO2} and z_{H2O}, providing a guide to the amount of brine to displace from the vessel during the establishment of initial conditions. The calculations

were made for various values of P^o, 20 bar, 40 bar, 70 bar and 100 bar. In all cases T was 293 K. Various values of S_{NaCl} were considered.

The first step in the calculation was to determine the equilibrium phase compositions. This was completed using the tuned PR EOS flash calculation. The equilibrium vapor phase V was calculated using the PR EOS. Since this was a preliminary calculation, the equilibrium aqueous phase density was approximated rather than implementing the highly accurate but lengthy aqueous phase density model of Li *et al*. (2011). This approximation was made from measured NaCl brine density versus S_{NaCl} data from Bourgoyne *et al*. (1986). The increase in brine density due to CO_2 dissolution is relatively small and was neglected. By specifying the volume of the vessel, nominally 0.6 dm^3, the moles of each CO_2 and H_2O were calculated. The calculation assumes that at initial conditions there are two pure phases. That is, there is no CO_2 in the aqueous phase and no H_2O in the vapor phase. Using the PR EOS for the CO_2 phase V and the approximation for brine density, P^o was calculated. The pressure drop reported is the difference between P^o and $P^{equilibrium}$.

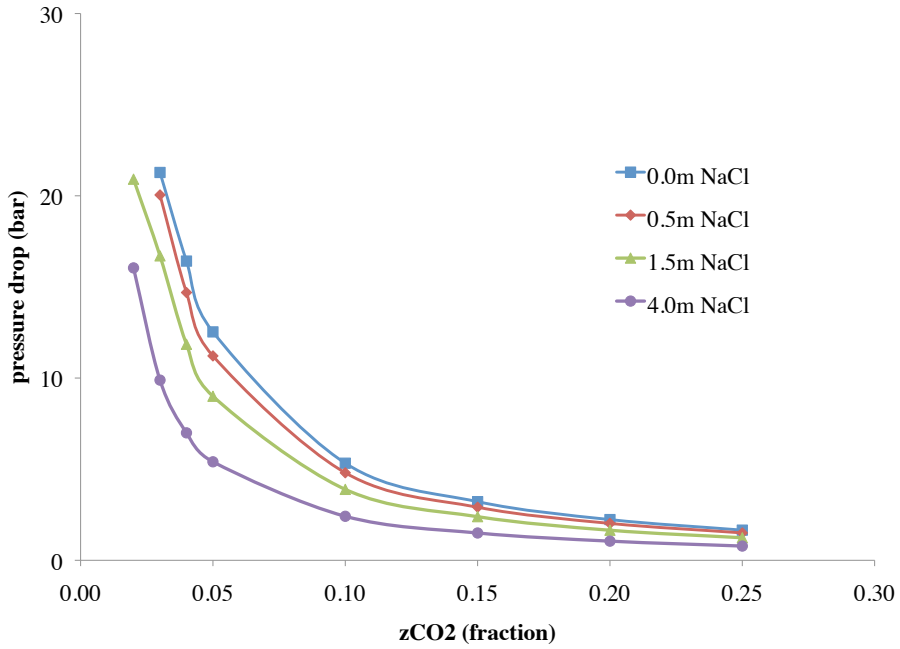

Figure 3.11: Calculated P drop (= $P^{o} - P^{equilibrium}$) versus z_{CO2}, $P^{equilibrium}$ = 40 bar, T = 293 K

Figure 3.11 shows that for a larger z_{CO2}, there is a smaller pressure drop between the initial pressure and final pressure. There is a smaller pressure drop in between initial and equilibrium for greater salinity brines, due to the reduced CO_2 solubility for larger NaCl salinity. In all cases considered and those presented in Figure 3.11, the pressure drop is of sufficient magnitude to be measured.

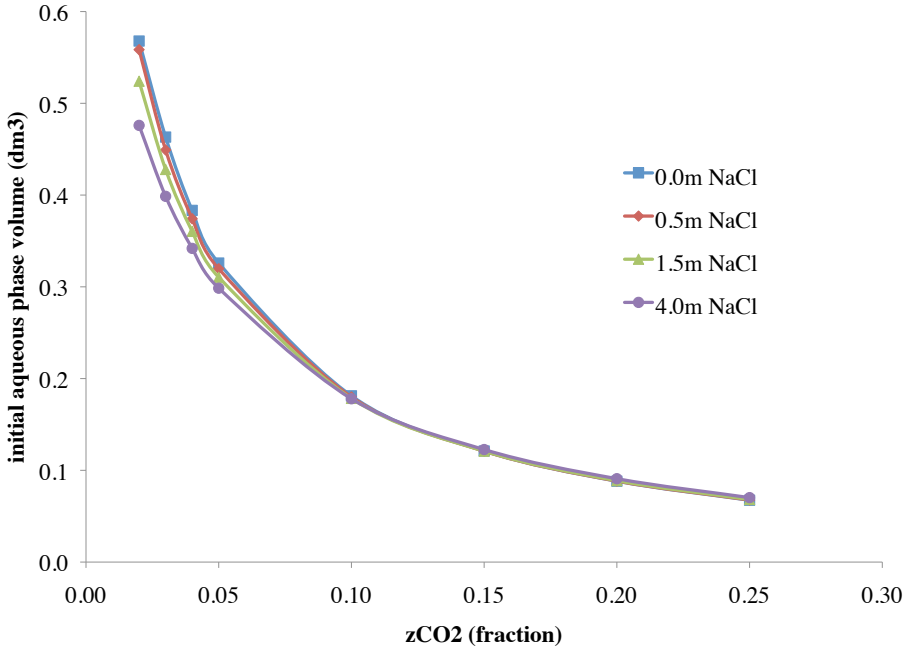

Figure 3.12: Initial aqueous phase volume versus z_{CO2}, $P^{equilibrium}$ = 40 bar, T = 293 K

Figure 3.12 demonstrates that for a larger z_{CO2}, a smaller initial aqueous phase volume is required. This is of practical importance due to two critical requirements for the application of Equation 2.4b, that the brine is well mixed and that a is quantifiable. A very small aqueous phase volume may lead a very unstable interface, whereas a very large aqueous phase may not be well mixed by the impeller. A choice of z_{CO2} of 0.05 results in an initial aqueous phase volume of approximately 0.33 dm^3. This is a reasonable selection to provide a stable interface and to allow the aqueous phase to be well mixed. For 0.0 m S_{NaCl}, the P drop was calculated to be 12.5 bar, see Figure 3.11.

Results for the 20 bar, 70 bar and 100 bar $P^{equilibrium}$ cases are included in full in Appendix C. With an aqueous phase volume similar to that selected above, the pressure

drop is measureable. Early experiments were conducted on the basis of z_{CO2} of 0.05, while later experiments, including the designed experiment, were conducted with an initial aqueous phase volume half the measured actual volume of the vessel.

3.3 EXPERIMENTAL APPARATUS

3.3.1 Equipment

The main component of the apparatus was a 600 cm^3 Parr Instrument Company 4560 Mini Bench Top Reactor. The vessel was made from Hastelloy C-276. This material was selected to resist corrosion from large salinity brines at great *T* and *P*. The maximum working *P* and *T* for the vessel was 207 bar and 623 K, respectively. Teflon seals were specified to resist damage from CO_2. The reactor was equipped with a 780 W heating unit and a cooling loop that allowed circulation of cold water. Laboratory tap water was used for cooling, the flow switched on and off by means of a solenoid controlled valve. The *T* inside the reactor was measured with a J-type thermocouple housed in a thermowell. A second J-type thermocouple was fitted to the heating unit. A magnetically coupled stirrer was fitted to the pressure vessel. The magnetic coupling provided transfer of torque to the stirrer without the need for a rotating seal that may be prone to leakage. A T316 stainless steel Bourdon tube pressure gage and safety rupture disc were fitted to the reactor. The pressure reactor and pressure controller are shown in Figure 3.13, while Figure 3.14 shows the pressure vessel internals.

Figure 3.13: Parr Instrument Company 4560 pressure reactor (disassembled) and 4848 reactor controller (Parr Instrument Company)

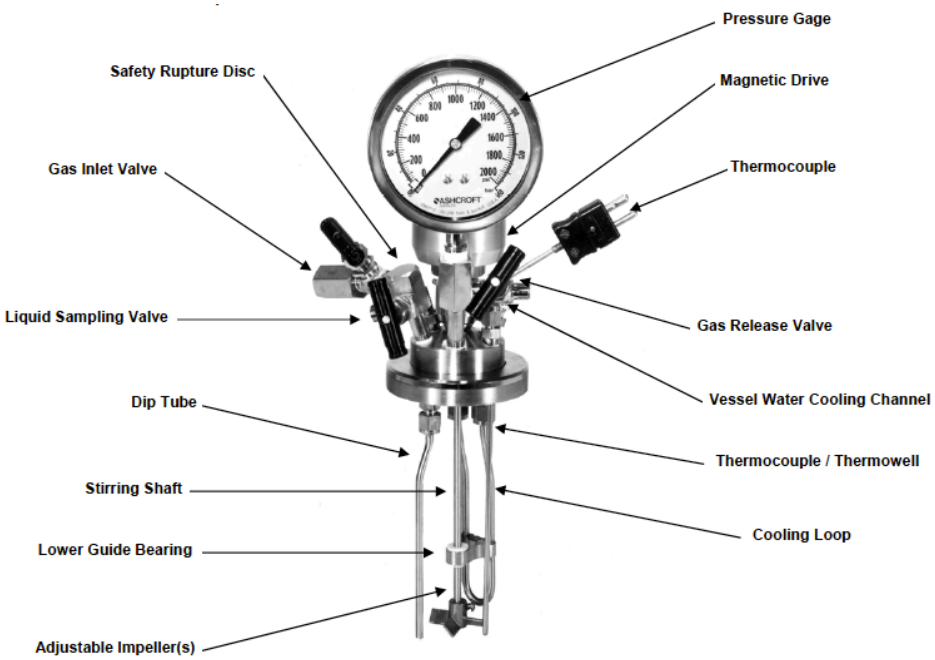

Figure 3.14: Internals of the Parr Instrument Company 4560 pressure reactor (Parr Instrument Company)

A Parr Instrument Company 4848 reactor controller was used. The unit provided full PID control of *T* and stirrer speed and auto tuning of PID parameters. The reactor controller also provided a local visual display of the current values of *T*, stirrer speed and *P*. Interface with a computer via a proprietary Parr Instrument Company software package allowed *T* measured by the primary and secondary thermocouples, stirrer speed and *P* to be recorded periodically with time.

A Teledyne ISCO 500D syringe pump was selected. The pump had a volume of 500 cm^3 and could provide flowrates up to 200 cm^3/min at up to 259 bar. The wetted materials used were Nitronic 50, Teflon and Hastelloy C-276. The pump controller provided two different operating modes, pressure mode and volume mode. In pressure mode a target pressure is achieved, where possible, by a change in flowrate. In volume mode a programmed flowrate is provided, regardless of the *P* up to a limit.

A Core Laboratories 1000 cm^3 floating piston accumulator was used. The wetted material used was 316 stainless steel. 1/8'' outer diameter stainless steel tubing and Swagelok two and three way valves were used for the hydraulic connections. Two Swagelok metering valves were also used. A Sartorius CPA3202S balance and Haskel compressor were also used. The equipment was connected as shown in Figure 3.15.

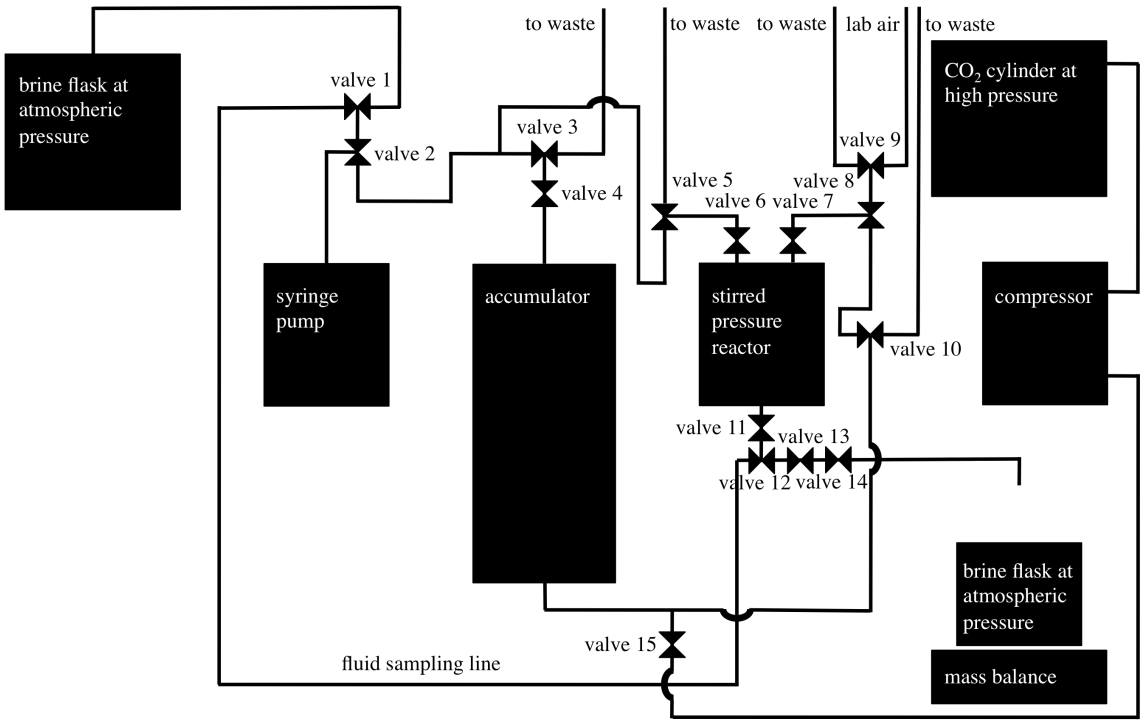

Figure 3.15: Experimental equipment schematic

A 720 W BriskHeat BSAT 101010 heat tape was wrapped around the accumulator. The heat tape was equipped with a time percentage controller, however this rudimentary control system was disabled by use in the 100% setting. For improved *T* control, a thermostatic *T* control system was used. Based on the *T* measured by a thermocouple placed between the tape and the accumulator, the heat tape was turned on and off by a Mantle Minder 104A PL512. The accumulator was wrapped with fiberglass insulation to maintain isothermal conditions at elevated *T* with less energy input and less heating cycles. A groove was machined into a steel rod, which was placed on the stainless steel pressure line between the accumulator and pressure reactor. The steel rod served to increase the thermal mass heated by another BriskHeat heat tape, identical to

the first, wrapped around it. The heat tape was controlled via a similar system as used for the accumulator, in this case the control T was measured by a thermocouple placed between the tape and the steel rod. The steel rod was then insulated with closed cell foam plumbing insulation. The CO_2 side of the accumulator was plumbed to a stand-alone pressure transducer and display unit. The complete experimental setup is shown in Figure 3.16.

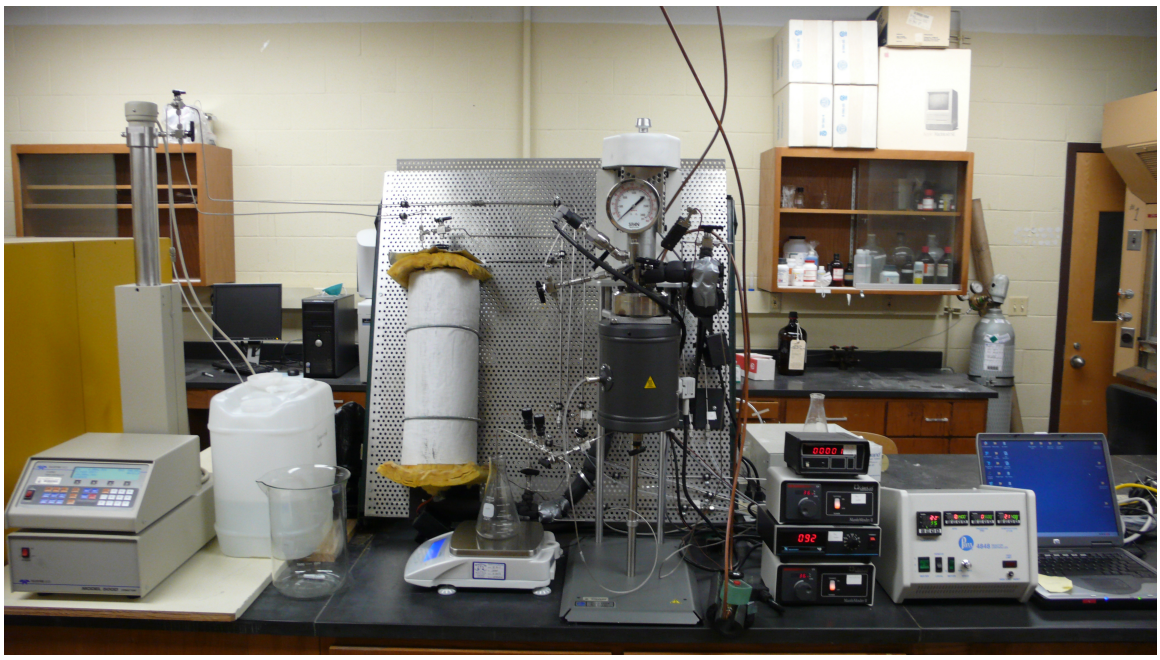

Figure 3.16: The complete experimental setup

From left to right, Figure 3.16 shows the syringe pump, a low P water vessel, large glass beaker for brine preparation, accumulator wrapped with heat tape and insulation, balance, stirred P reactor, stack of heat tape controllers and CO_2 side P transducer, reactor controller and logging computer. The CO_2 compressor and bottle are not shown in Figure 3.16.

3.3.2 Experimental Procedure

The experimental procedure developed consisted of the four main steps outlined below:

1. Filling the pre heated accumulator with CO_2:

• The syringe pump was filled with water.

• The CO_2 side of the accumulator was purged by pumping water into the water side of the accumulator while the CO_2 side was open to the atmosphere.

• The CO_2 side of the accumulator was switched to the CO_2 compressor, the compressor turned on while water was withdrawn from the water side of accumulator by the syringe pump.

• The accumulator was closed except for venting as necessary to adjust the *P* to the desired P^o. This venting typically needed to be completed a number of times as the *T* of the CO_2 was equilibrated with the accumulator.

2. Filling the heated pressure reactor with synthetic brine:

• The fluids from the previous experiment were displaced from the bottom of the reactor to the beaker. The syringe pump was filled with de-ionized water and used to flush any residual brine from the vessel.

• The required synthetic brine was prepared in the glass beaker from de-ionized water and NaCl and/or $CaCl_2$, a magnetic stirrer was used for mixing.

• The syringe pump was filled with synthetic brine.

• The synthetic brine was pumped into the *P* reactor, displacing air to the atmosphere. The reactor was filled via the liquid fill valve while the air exited the gas release valve on the top of the vessel. When brine was seen flowing out the gas release valve, the pressure reactor was known to be full.

• The *P* reactor was closed except for a connection to the syringe pump, which was set to the desired P^o. The magnetic stirrer was turned on and the brine *T* increased to the desired level.

3. Displacing half of the volume of synthetic brine with CO_2:

• Once the CO_2 and synthetic brine had each reached steady state at the desired *T* and P^o, the magnetic stirrer was turned off and the *P* reactor closed.

• The synthetic brine was dumped from the syringe pump and it was filled with water. The syringe pump was switched to the water side of the accumulator.

• The CO_2 side of the accumulator was opened to the stirred reactor. The bottom drain valve was opened and half of the volume of the synthetic brine was displaced to a beaker on the balance. The actual measured pressure vessel volume with the single impeller in place was 591 cm^3. The Swagelok metering valves were adjusted, prior to the displacement, to allow the brine displacement to occur in approximately the same amount of time for each experiment. For experiments at larger *P*, the metering valves were placed in a setting with a small flow coefficient and vice versa.

4. Recording the pressure decay with time:

• The *P* reactor was closed.

• The magnetic stirrer was turned on.

• The *P*, primary and secondary *T*, and stirrer speed continued to be recorded periodically with time.

The data sheet completed for traceability purposes for each experiment is included in Appendix D.

3.3.3 Mechanical Configuration

A number of different mechanical configurations were used. A single downward pumping 45° pitched four-blade impeller, referred to as the impeller, was used to mix the aqueous phase, while maintaining a known a. between aqueous and CO_2-rich phases. A small number of experiments were conduced with two identical impellers on the same stirrer shaft. The experiments using the impeller were designed to allow the accurate calculation of k_L. A small number of experiments were conducted with a gas entrainment impeller, which allowed the increase in a to be quantified for this particular stirred pressure reactor. Both mixers are shown in Figure 3.17.

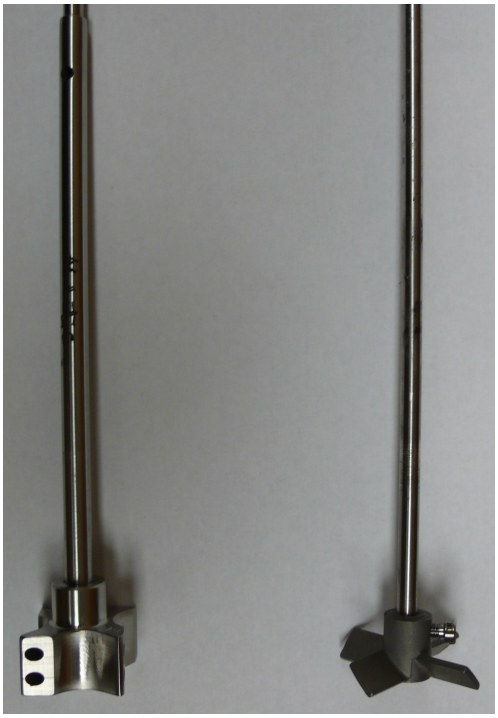

Figure 3.17: Gas entrainment impeller (left) and impeller (right)

A baffle unit was used for some experiments. The baffles are four plates that are fitted to the *P* vessel to break up the large central vortex that may form in an un-baffled vessel. The baffle unit is shown in Figure 3.18.

Figure 3.18: The baffle unit

3.4 EXPERIMENTAL INVESTIGATION RESULTS

3.4.1 Unstirred Experiment

To examine the time scale of an unstirred experiment, one was conducted. The experiment was conducted at ambient *T*, that is, there was no heating or cooling of the apparatus. P^{o} and $P^{equilibrium}$ were 52.7 bar and 39.9 bar, respectively. De-ionized water

was used. Approximately 274 g of water was displaced from the pressure vessel, leaving a z_{CO2} of 0.05. Data were recorded every 30 s.

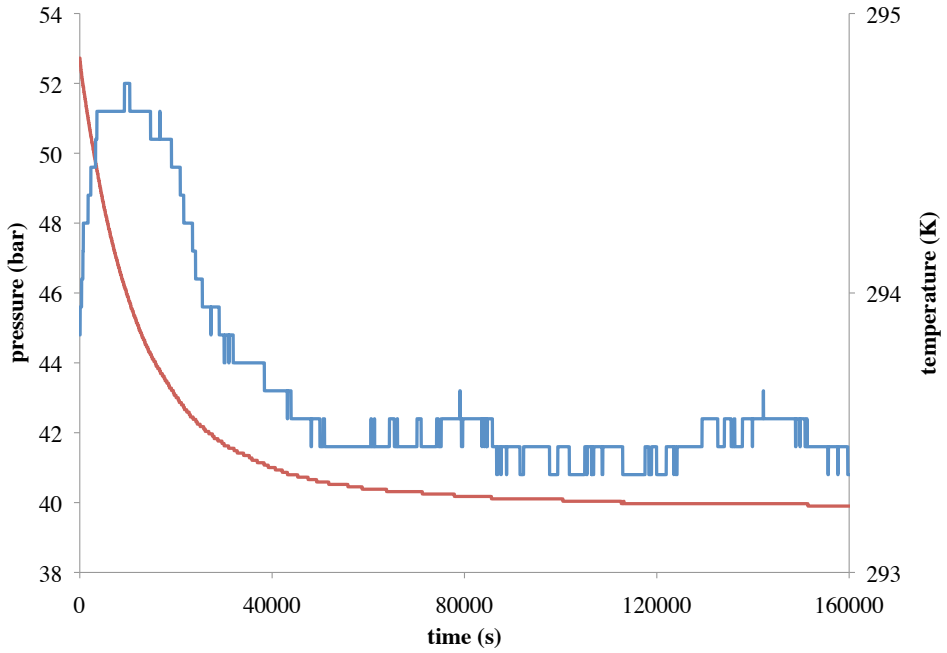

Figure 3.19: *P* (red curve) and *T* (blue curve) versus time for an unstirred experiment

The mechanism for mass transfer in the unstirred experiment is a combination of diffusion and density driven natural convection, similar to systems studied by Yang and Gu (2006) and Farajzadeh *et al*. (2009). It is apparent that it takes a considerable amount of time to reach equilibrium. Most of the *P* decline has occurred by 80 000 s or approximately twenty-two hours. At 160 000 s the *P* is 39.9 bar, the experiment was run to 349 290 s and the *P* remained unchanged at 39.9 bar. The *P* change was 12.8 bar, which is very close to the 12.5 bar calculated. The difference between the two is only 2.4%. This validates the calculation method used for the prediction of *P* drop. The fact

that mass transfer is so slow in the unstirred vessel is useful; it is exploited in fluid sampling experiments discussed below.

Data for the heat of solution of CO_2 in H_2O at 288 K indicates that 19.4 kJ/mol of heat is generated in an exothermic process (Martinez, 2012). Data at 293 K is not readily available. Using the tuned PR EOS flash calculation for CO_2 solubility at 40 bar and 293 K, it was calculated that a 5.2 K increase in T could be expected. This calculation assumes the specific heat capacity of the H_2O and CO_2 solution is the same as pure H_2O and uses data from NIST (2012). Critically it also assumes no heat dissipation to the surrounding vessel. Figure 3.19 shows that in an actual unstirred experiment, the heat generated results in a T increase of approximately 1 K.

3.4.2 Repeatability

In developing the experimental procedure, a particular experiment was repeated a number of times to gauge repeatability. The T and P conditions were the same as for the unstirred experiment. That is, the experiment was conducted at ambient temperature. P^o and $P^{equilibrium}$ were 52.7 bar and 41.1 bar to 41.3 bar, respectively. De-ionized water was used. The centerline of the impeller was approximately 1.6×10^{-2} m from the bottom of the vessel. A stirrer speed of 16.7 rev/s was used. Approximately 274 g of water was displaced from the pressure vessel, leaving a z_{CO2} of 0.05. Data were recorded every 1 s.

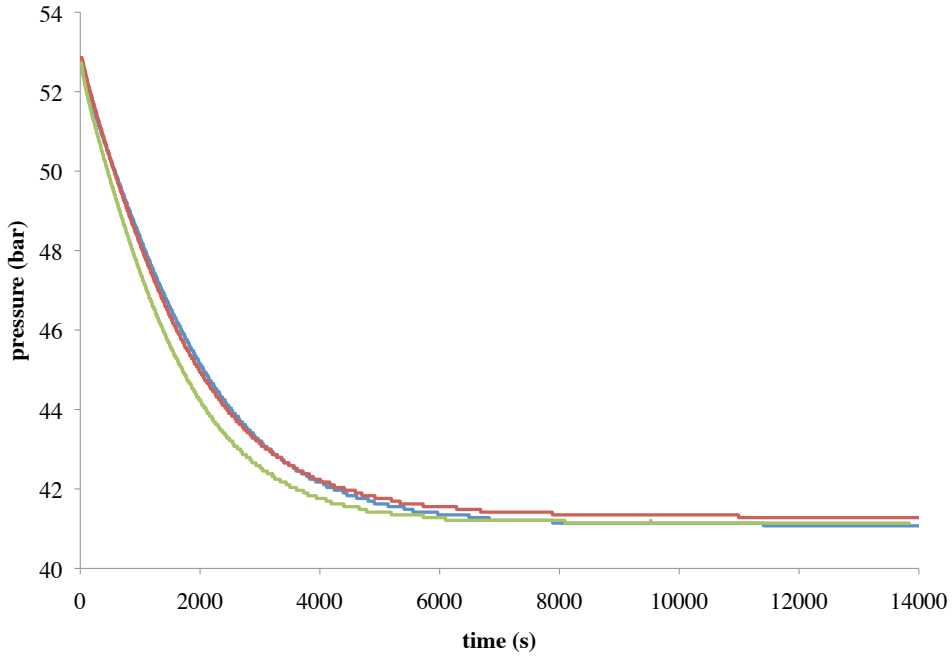

Figure 3.20: *P* versus time for three repeats of a particular experiment

As expected, mixing the aqueous phase greatly reduces the time taken to reach equilibrium. Most of the *P* decline occurred by 8 000 s or approximately two hours, a factor of ten reduction in time compared to the unstirred case.

The *P* decline rates of the three repeats were similar though not identical. The data shown in green shows that this particular experiment reached equilibrium faster than the other two. $P^{equilibrium}$ was 41.1 bar for two experiments and 41.3 bar for the other. One possible reason for the difference in the equilibrium pressures is the amount of CO_2 that was transferred to the aqueous phase during the displacement. If there is a greater amount of CO_2 transported to the aqueous phase during the displacement, less CO_2 will be

transported from the vapor phase while the system is closed and stirred, resulting in a larger $P^{equilibrium}$.

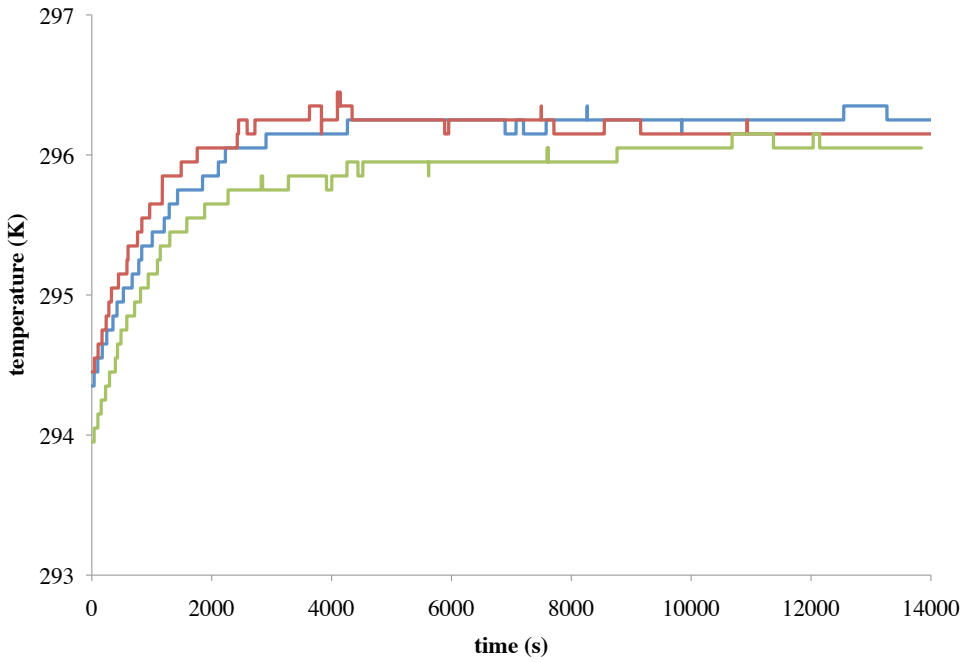

Figure 3.21: T versus time for three repeats of a particular experiment (for each experiment the colors used correspond to those used in Figure 3.20)

It is apparent from Figure 3.21 that the temperature rise for all three experiments was very similar. The same heat of dissolution is produced for the stirred and unstirred experiments. In the stirred experiments above, the temperature rise is approximately 2.5 K, rather than the 1 K observed during the early stage in the unstirred case. This is consistent with the faster heat generation rate from faster dissolution and similar rate of heat dissipation. After dissolution is complete the temperature in the stirred vessel remains at a plateau above the initial (ambient) value, while the temperature in the unstirred vessel declines to initial (ambient) temperature. This is because some of the

mechanical energy of stirring is dissipated as heat. A more comprehensive repeatability study is included in the final set of experiments, covered in section 3.5 'Designed Experiment Results'.

3.4.3 Effect of NaCl Salinity and Stirrer Type on Time to Equilibrium

A series of experiments was conducted to quantify the effect of NaCl salinity on time taken to reach equilibrium. The experiments were run at ambient T. The $P^{equilibrium}$ was approximately 41 bar, though slightly different for each experiment. With the same z_{H2O} and $P^{equilibrium}$ used for each experiment, the larger the NaCl salinity, the smaller the P^{o} required since greater salinity brines have a smaller CO_2 solubility. Values of P^{o} from 45.6 bar to 52.7 bar were used for 4 m NaCl and 0 m NaCl, respectively. The P^{o}s used in the other two tests were between these values. Brine masses of 274g to 344g were displaced from the pressure vessel initially for 0 m and 4 m NaCl, respectively, leaving z_{CO2} of 0.05. Data were recorded every 1 s.

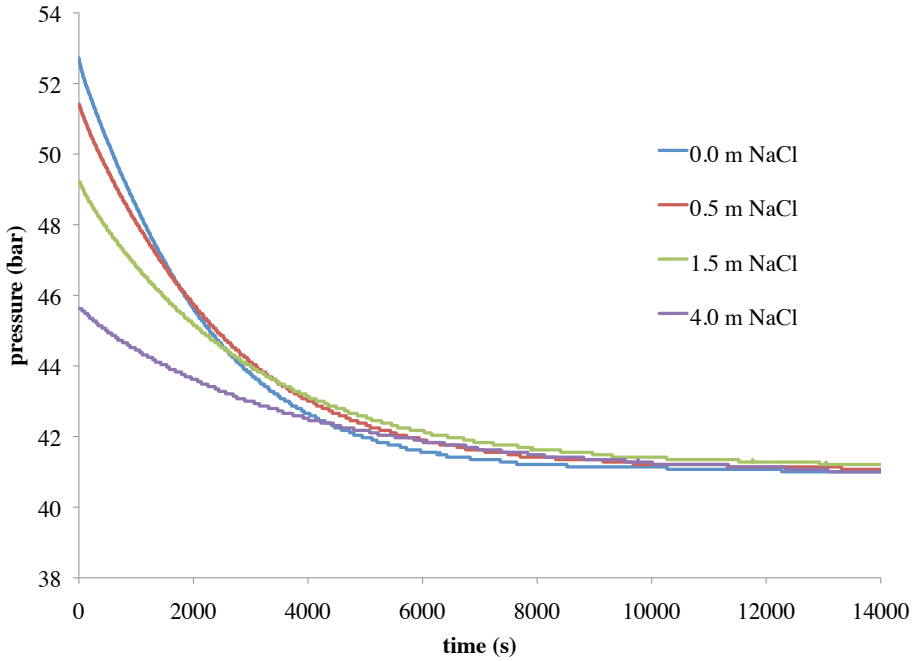

Figure 3.22: P versus time for experiments with different S_{NaCl}

From Figure 3.22, it is apparent that the time taken to equilibrium is very similar for all four experiments, approximately 10 000 s. It is not immediately obvious from this result whether the k_L for each experiment would be different. For greater salinity brine, the driving force for mass transfer is smaller due to reduced CO_2 solubility. Since greater salinity brine experiments commenced at smaller values of P^o, CO_2 solubility is further reduced. However, while there are two factors reducing the driving force, the reduced CO_2 solubility also reduces the amount of CO_2 that must be transported to reach equilibrium. These competing effects are analyzed quantitatively in section 3.5.4 'Discussion of Results'.

The experiments were repeated with the gas entrainment impeller fitted. The results are shown in Figure 3.23.

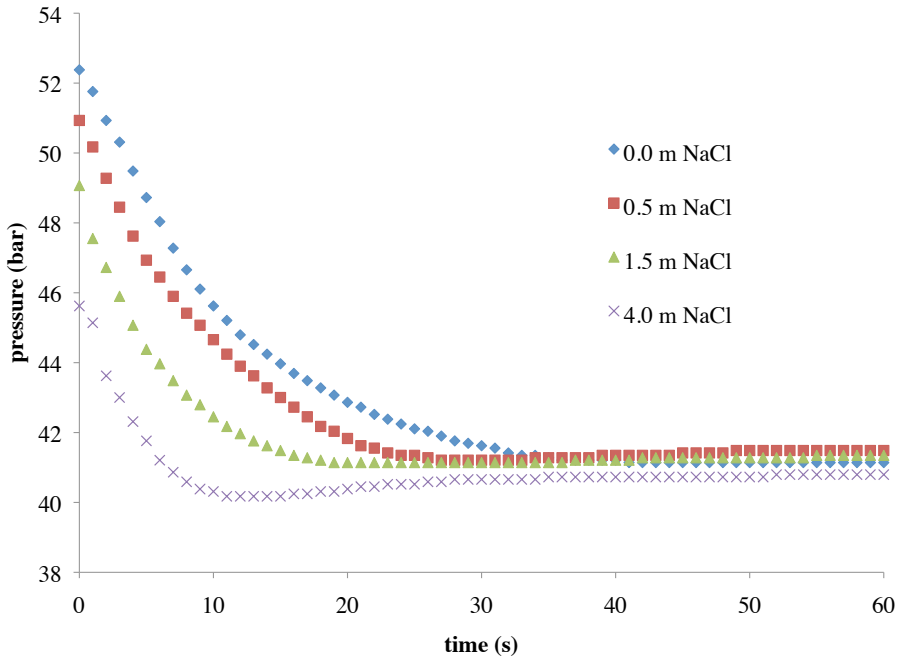

Figure 3.23: P versus time for gas entrainment experiments with different S_{NaCl}

Figure 3.23 demonstrates that the time taken to equilibrium using the gas entrainment impeller, for the given conditions, is between 10 s and 35 s. The greater salinity brines reach equilibrium in less time than the smaller salinity brines. The time taken to reach equilibrium for the impeller experiments was approximately 10 000 s. With the gas entrainment impeller fitted, the longest time taken to equilibrium is 35 s, which is approximately 300 times smaller. With the assumption that k_L is the same in both cases, a must be close to 300 times greater in the gas entrainment cases over the stirred only case. This is plausible; the CO_2-brine interface has area approximately equal to the cross section of the vessel in the impeller experiments, or 31.7 cm^2, while 50,000 bubbles of radius 0.12 cm would have a volume of 74.0 cm^3 (a modest fraction of the volume of either phase) and an area of 9,500 cm^2.

3.4.4 Flow Visualization Experiments

The deliberate introduction of gas bubbles clearly increases the rate of mass transfer dramatically. Thus inadvertent introduction of bubbles by entrainment during stirring with the impeller would greatly affect the interpretation of the experiments. Quantifying the interfacial area of bubbles is difficult, so to meet the objectives of this research gas entrainment was to be avoided. Correlations for the onset of gas entrainment are available in the literature. Such correlations have been published by Sverak and Hruby (1981), Joshi *et al*. (1981), Heywood *et al*. (1985), Tanaka *et al*. (1986), Veljkovic (1991), Bhattacharya *et al*. (2007) and Mali and Patwardhan (2009). All were produced from experiments using larger vessels than the one used for this research. Since their applicability to a smaller vessel is uncertain, a series of experiments was conducted using an appropriately sized vessel. A transparent acrylic vessel was constructed with the same dimensions as the *P* vessel used for *P* decay experiments. The acrylic vessel was filled with water, then 300 g of the water displaced by air, leaving an aqueous phase volume half of the nominal volume of the vessel, similar to the arrangement in most of the dissolution experiments. A number of difference mechanical configurations and stirrer speeds were used:

- Single impeller, placed close to bottom of vessel, vessel baffled
- Single impeller, placed close to bottom of vessel, no baffles fitted to vessel
- Double impeller, no baffles fitted to vessel
- Double impeller, vessel baffled
- Single impeller, placed further from bottom of vessel, no baffles fitted to vessel
- Single impeller, placed further from bottom of vessel, vessel baffled

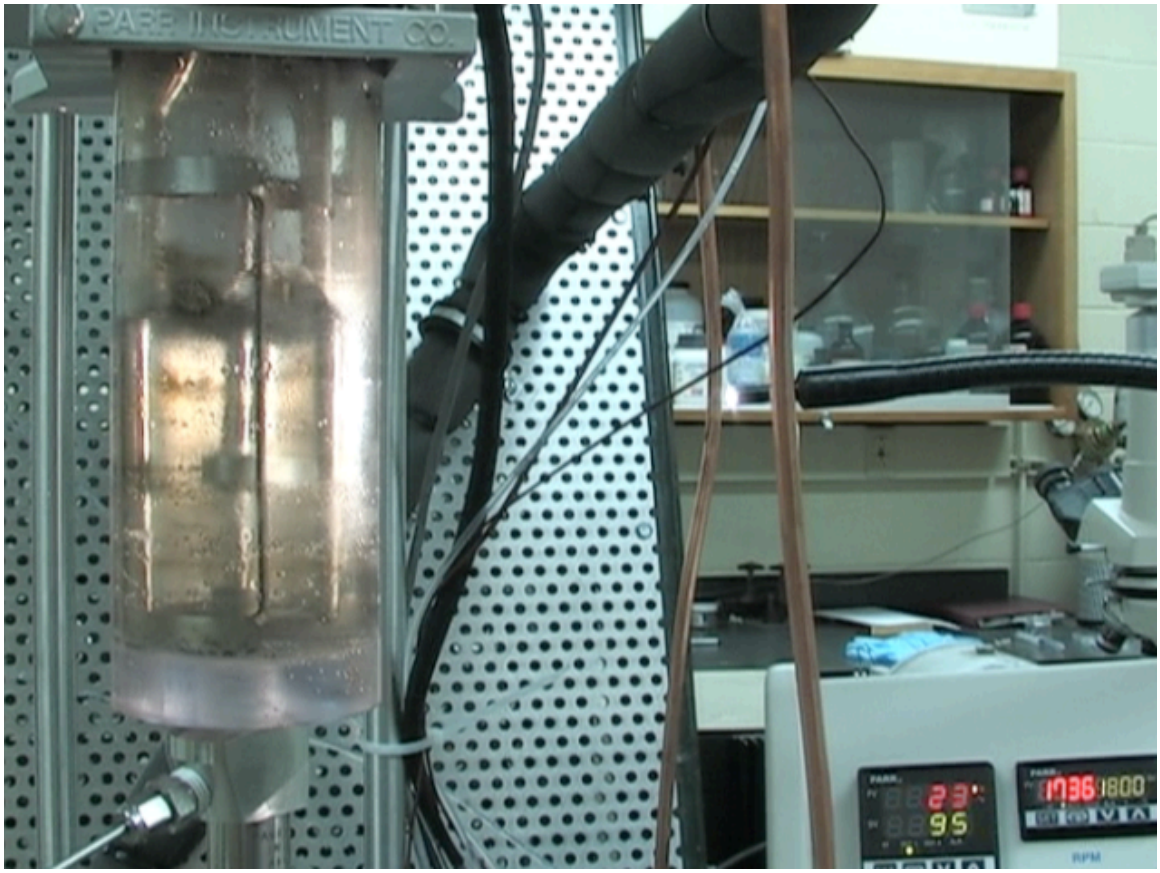

Figure 3.24: Single impeller at 28.9 rev/s, placed close to bottom of vessel, vessel baffled, no gas entrainment

Figure 3.24 shows the acrylic vessel with the baffle unit fitted and a single impeller placed close to the bottom. The centerline of the impeller was approximately 1.6×10^{-2} m from the bottom of the vessel. Stirrer speeds of 3.3 rev/s to 29.0 rev/s were used with 3.3 rev/s increments. No visible gas entrainment was observed at any of the operating speeds. The surface of the water was not completely flat, but no large central vortex was formed, as expected for a baffled vessel.

Figure 3.25: Single impeller at 29.0 rev/s, placed close to bottom of vessel, no baffles fitted to vessel, no gas entrainment

Figure 3.25 shows the acrylic vessel without the baffle unit fitted and a single impeller placed close to the bottom. Again, the centerline of the impeller was approximately 1.6×10^{-2} m from the bottom of the vessel. Stirrer speeds of 3.3 rev/s to 29.0 rev/s were used with 3.3 rev/s increments. No visible gas entrainment was observed at any of the operating speeds. Since the vessel is un-baffled, a large central vortex was expected to be present, such as that first described mathematically by Nagata (1975) and subsequently studied by Markopoulos and Kontogeorgaki (1995) and Smit and During

(1991). However, a large central vortex did not form during the experiment. It can be concluded that the vessel internals, such as the cooling loop, thermowell and liquid fill tube effectively baffle the vessel. The water surface was not completely flat.

Figure 3.26: Double impeller at 8.3 rev/s, no baffles fitted to vessel, no gas entrainment

Figure 3.26 shows the acrylic vessel without the baffle unit fitted and a double impeller configuration. The centerline of the lower impeller was approximately 1.6×10^{-2} m from the bottom of the vessel, the upper impeller was approximately 6.6×10^{-2} m from the bottom of the vessel. Stirrer speeds of 3.3 rev/s to 29.0 rev/s were used with 3.3 rev/s

increments. Visible gas entrainment was observed at 10.0 rev/s and above. Figure 3.26 shows no gas entrainment with a stirrer speed of 8.3 rev/s. No large central vortex was formed, again demonstrating that the vessel was effectively baffled by the internals. The water surface was not completely flat.

Figure 3.27: Double impeller at 25.9 rev/s, no baffles fitted to vessel, continuous gas entrainment

Figure 3.27 shows considerable ongoing gas entrainment with a stirrer speed of 25.9 rev/s. It is apparent that to avoid gas entrainment with this mechanical configuration, the stirrer speed would be limited to less than 10.0 rev/s. The double impeller

configuration was tested with baffles fitted to the vessel and while again there was no large central vortex produced, there was visible gas entrainment at 10.0 rev/s and above. The baffles made no difference to the onset of gas entrainment.

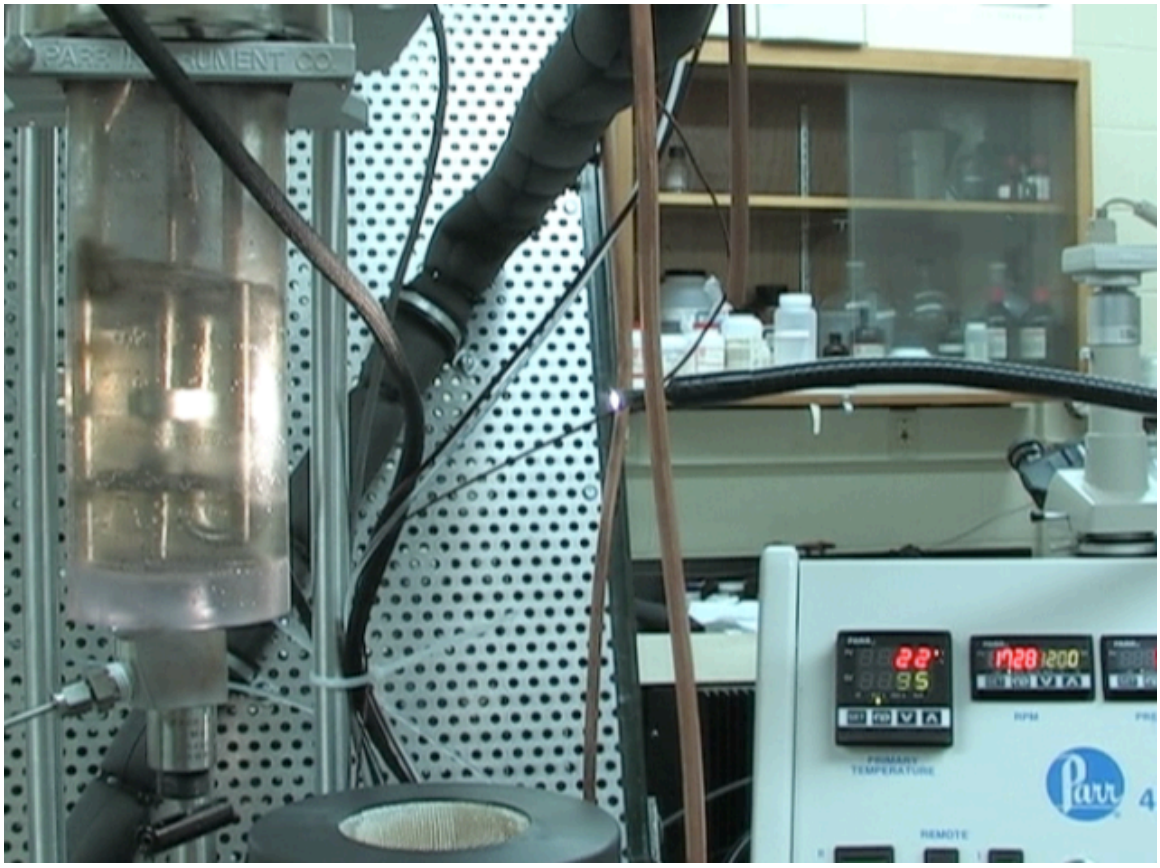

Figure 3.28: Single impeller at 28.8 rev/s, placed further from bottom of vessel, no baffles fitted to vessel, occasional air bubble circulated through water

Figure 3.28 shows the acrylic vessel without the baffle unit fitted and a single impeller placed further from the bottom than in previous experiments. The centerline of the impeller was approximately 3.4×10^{-2} m from the bottom of the vessel. Stirrer speeds of 3.3 rev/s to 29.0 rev/s were used with 3.3 rev/s increments. An occasional air bubble

was observed to be circulated through the water at stirrer speeds over 23.3 rev/s, though there was not continuous gas entrainment for any stirrer speeds. The water surface was not completely flat, though once more no large central vortex was formed, demonstrating that the vessel was effectively baffled by the internals.

Figure 3.29: Single impeller at 28.9 rev/s, placed further from bottom of vessel, baffles fitted to vessel, occasional air bubble circulated through water

Figure 3.29 shows the acrylic vessel with the baffle unit fitted and a single impeller placed further from the bottom than in previous experiments. The centerline of the impeller was approximately 3.4×10^{-2} m from the bottom of the vessel. Stirrer speeds

of 3.3 rev/s to 29.0 rev/s were used with 3.3 rev/s increments. Similarly to the setup shown in Figure 3.28, an occasional air bubble was observed to be circulated through the water at stirrer speeds over 23.3 rev/s, though there was not continuous gas entrainment for any stirrer speeds. Again the baffles made no difference to the onset of gas entrainment.

3.4.5 Mechanical Configuration Experiments

From the flow visualization experiments it was concluded that the baffle unit made no difference to the onset of gas entrainment as the vessel internals effectively baffle the vessel. It was also determined that there is a critical speed over which continuous gas entrainment occurs for a double impeller configuration. For the single impeller configuration there was no continuous gas entrainment, though an occasional air bubble may be circulated through the water when the impeller is further from the bottom of the vessel and closer to the phase interface. Of course it should be noted that the flow visualization experiments were conducted with a water/air system at small P, not a brine/CO_2 system at large P. With a large P brine and CO_2 system, there is a smaller difference in the density of the phases, which may lead to gas entrainment at slower stirrer speeds.

To confirm insights from the visualization experiments, a number of P decay experiments were conducted in the Parr reactor using the same mechanical configurations examined in the flow visualization experiments. The double impeller configuration was operated at a stirrer speed of 8.3 rev/s, which is below the critical speed of 10.0 rev/s where gas entrainment is observed. A number of tests with the single impeller

configuration were conducted. A stirrer speed of 30.0 rev/s used with the impeller close to the bottom of the vessel, 23.3 rev/s with the impeller further from the bottom of the vessel.

The experiments were all conducted at ambient T. De-ionized water was used. P^o was 49.8 bar for the experiment with the single impeller with centerline approximately 1.6×10^{-2} m from the bottom of the vessel and no baffles fitted. For the experiment with the single impeller with centerline approximately 1.6×10^{-2} m from the bottom of the vessel and baffles fitted to the vessel, P^o was 50.5 bar. Data were recorded at 1 s intervals for both these experiments. For the experiment with the double impeller and no baffles fitted to the vessel, P^o was 50.5 bar. For the single impeller with centerline approximately 6.6×10^{-2} m from the bottom of the vessel and no baffles fitted, P^o was 50.3 bar. In each of the experiments, approximately 274 g of water was displaced from the pressure vessel, leaving a z_{CO2} of 0.05. Data were recorded every 10 s for these two experiments.

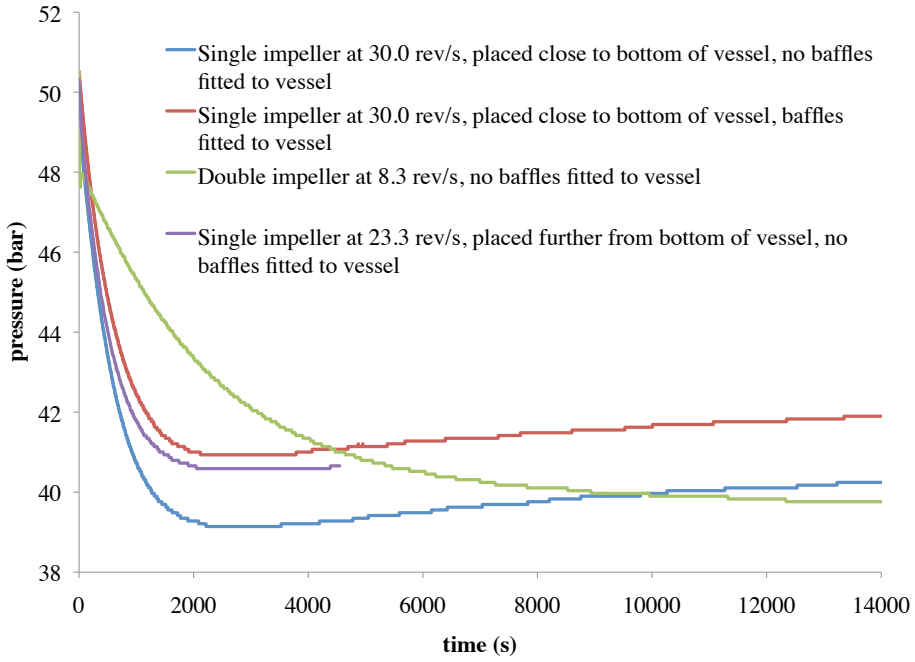

Figure 3.30: *P* versus time for various mechanical configurations

The results in Figure 3.30 show that with the double impeller operated below the critical stirrer speed at which gas entrainment occurs, the time to equilibrium is much longer (about 12 000s) than any of the single impeller experiments (about 2000 s). The single impeller experiments were operated at greater stirrer speed but still below the speed at which gas entrainment was observed (recall that only the occasional air bubble was observed for the greatest operating speeds in the flow visualization experiments). There was no difference in the time to reach equilibrium with baffles fitted and without baffles fitted to the pressure vessel, indicating no change in the mixing achieved. The placement of the impeller does make a difference. With the impeller placed further from the bottom of the vessel a smaller stirrer speed, 23.3 rev/s, produced the same time to equilibrium as operating the stirrer at 30.0 rev/s with the impeller closer to the bottom of the vessel.

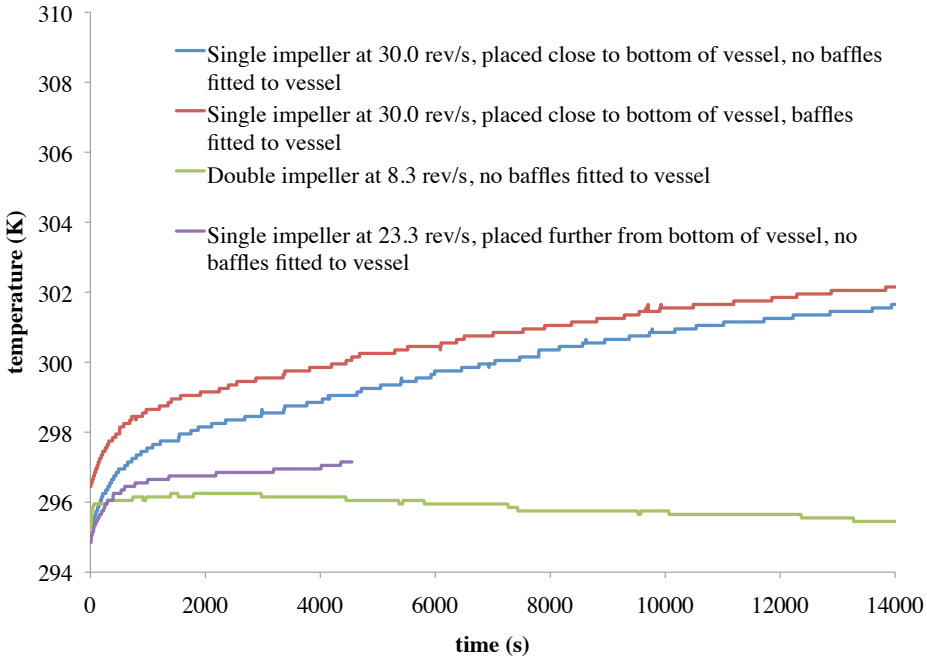

Figure 3.31: *T* versus time for various mechanical configurations

While the single impeller experiments operated at 30 rev/s reached equilibrium in approximately 2100 s, *P* subsequently increased. When examining Figure 3.31, it is apparent that *T* continued to increase after reaching equilibrium. There is a *T* increase associated with the viscous dissipation from stirring, which accumulates as the duration of the experiments is tens of minutes. The greater the stirrer speed the larger the rate of viscous dissipation and, in turn, the larger the rate of *T* increase. The increased *T* due to CO_2 dissolution and stirring reduces the solubility of CO_2, which causes a net movement of CO_2 to the vapor phase. The increased number of moles of CO_2 in the vapor phase, combined with the larger *T* leads to the increase in *P*. This result highlights the importance of *T* control. No *T* control was applied during these experiments, so some of the heat generated by stirring and by CO_2 dissolution is transferred from the vessel to the surroundings. This is apparent in the double impeller experiment of Figure 3.31, in which

the T decreases after dissolution is complete. The smaller rate of viscous dissipation in this experiment leads to a smaller equilibrium T than the experiments with large stirrer speeds.

3.4.6 Effect of Stirrer Speed on Time to Equilibrium

The mechanical configuration experiments demonstrated that for stirrer speeds below that which causes the onset of gas entrainment in a small-pressure water and air system, the single impeller configurations reached equilibrium in less time. Further, with the impeller placed further from the bottom of the vessel, a slower stirrer speed produced the same time to equilibrium as a faster stirrer speed with the impeller closer to the bottom of the vessel. Subsequent experiments were conducted with the single impeller configuration, placed further away from the bottom of the vessel.

The calculated mass transfer coefficient, k_L, is related to the time to equilibrium inferred from the recorded P versus time data. When comparing otherwise identical experiments, the apparent k_L calculated from an experiment with a shorter time to equilibrium will be greater than apparent k_L calculated from an experiment with a longer time to equilibrium. A series of experiments was conducted to quantify the effect of stirrer speed on the time taken to reach equilibrium. The experiments were conducted at nine stirrer speeds from 3.3 rev/s to 30.0 rev/s, in 3.3 rev/s increments. The experiments were conducted with de-ionized water and no active heating or cooling used. In each of the experiments, approximately 301 g of water was displaced from the pressure vessel. Data were recorded every 1 s for these nine experiments. Chronologically, these were completed prior to the mechanical configuration experiments. Thus the effect of impeller

placement had not yet been studied and these were conducted with the impeller placed close to the bottom of the pressure vessel. The trends from these experiments are assumed to be directly transferable to the case of the impeller placement further from the bottom of the pressure vessel.

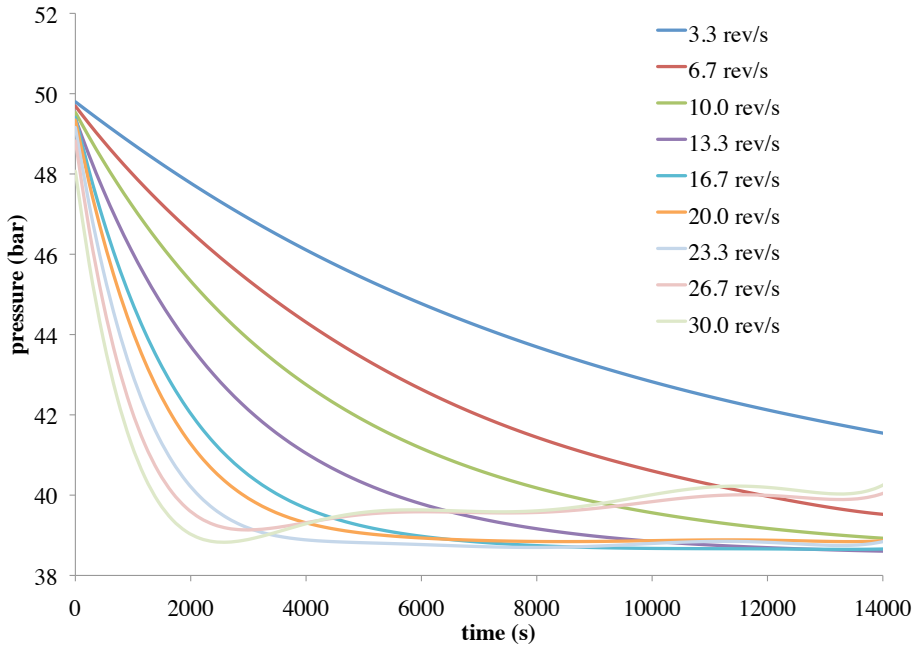

Figure 3.32a: *P* versus time for a series of experiments with different stirrer speeds

Figure 3.32a presents high order polynomial trend lines fitted to the data. Since the raw data was recorded at 1 s, it cannot be displayed on one plot due to limitations of the spreadsheets used to display data. The worst fit between the polynomial trend line and recorded experimental data was observed for the experiment at 30.0 rev/s. The data and trend line for this experiment are presented in Figure 3.32b.

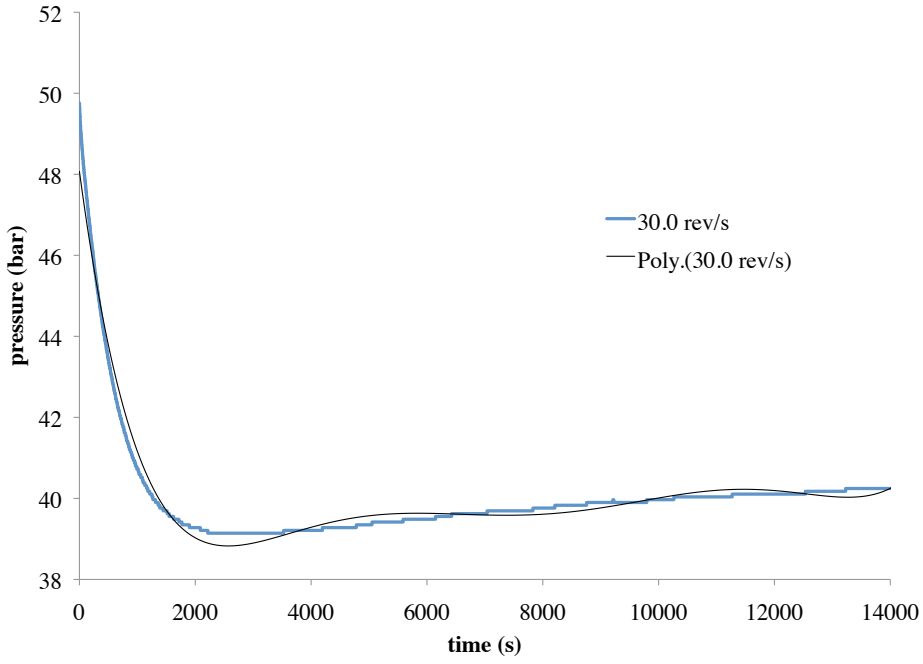

Figure 3.32b: experimental *P* data and trend line fitted for experiment at 30.0 rev/s

Figure 3.32b demonstrates that the trend lines fitted adequately represent the experimental data for the purposes of a qualitative comparison.

Returning to Figure 3.32a, it is apparent that the faster the stirrer speed used, the shorter the time taken to reach equilibrium. Therefore, the faster the stirrer speed, the larger the apparent value of k_L. The question that arises from this result is what stirrer speed is appropriate to use for subsequent experiments. There are a number of possible reasons for the trend observed in Figure 3.32a. One is that the aqueous phase is mixed more effectively with increasing stirrer speed. A second possibility is that there is more gas entrainment with increasing stirrer speed. A third possibility is that there is a

combination of mixing effectiveness and gas entrainment factors present. It is not possible to conclusively identify the mechanism from these series of experiments alone.

It also apparent from Figure 3.32a that P actually increased in two of the experiments, after reaching a minimum, rather than remaining constant as expected when dissolution is complete. This is due to the T rise from viscous dissipation effect at large stirrer speeds discussed earlier.

3.4.7 Aqueous Phase Sampling Experiments

The stirrer speed experiments demonstrated that increased stirrer speed reduced time to equilibrium, but did not explain the mechanism responsible. Improved mixing, gas entrainment (which increases a) or a combination of both could be responsible. To test the hypothesis that improved mixing of the aqueous phase was responsible, a series of aqueous phase sampling experiments was conducted at different stirrer speeds.

The series of experiments compared different stirrer speeds used for otherwise identical experiments. A P^o of 50.7 bar was selected. No heating or cooling was used, so ambient temperature conditions prevailed. De-ionized water was used, with 296g displaced from the pressure vessel. If left to continue to equilibrium, $P^{equilibrium}$ was found to be approximately 40.7 bar, with slight variation between experiments.

Sampling was conducted at 45.6 bar, half way between P^o and $P^{equilibrium}$. By sampling at the same pressure for each experiment, the total moles of dissolved CO_2 were the same for each experiment. Experiments at faster stirrer speeds reached this point in a

shorter period of time than those conducted at slower stirrer speeds. To limit further CO_2 dissolution during the process of fluid sampling, the stirrer was turned off before withdrawing a sample. This effectively changed the flow regime to that of an unstirred experiment. As shown in section 3.4.1 'Unstirred Experiment', mass transfer is much slower in this regime, so turning off the stirrer should have the effect of quenching the experiment. To confirm this expectation, four experiments were conducted with a stirrer speed of 23.3 rev/s. Data were recorded every 10 s. For one of the four experiments, the stirrer was turned off when the pressure reached 45.6 bar. After a period of time the stirrer was turned on at 23.3 rev/s once more.

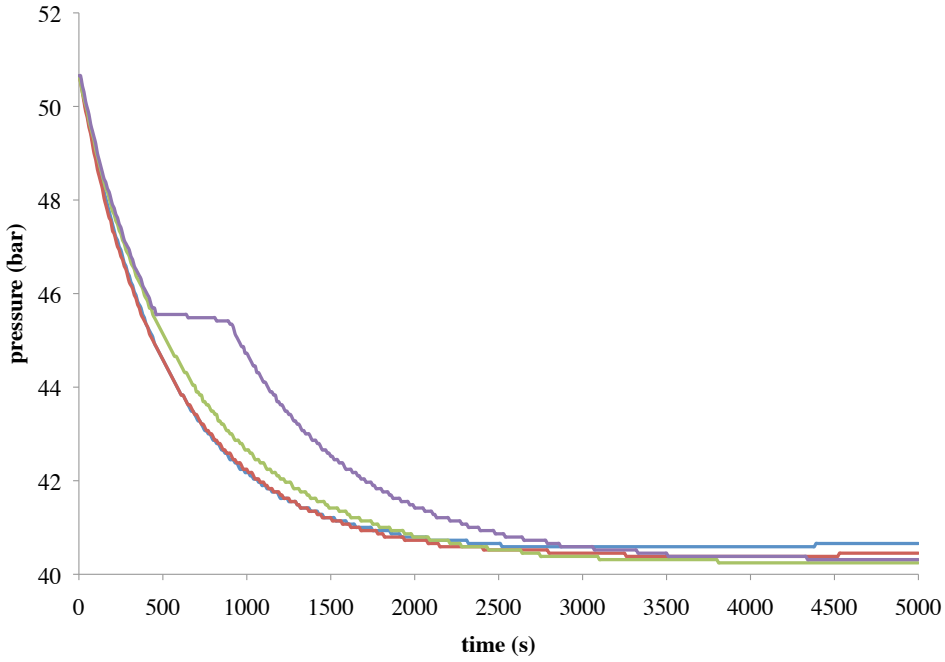

Figure 3.33: *P* versus time for four repeats of the same experiment, one with a period of no stirring

Figure 3.33 shows the data recorded for the experiment where the stirrer was turned off in purple. The stirrer was turned off at 460 s and turned on once more at 920 s. During this time the reduction in *P* was only 0.3 bar. For the other three experiments, where the stirrer was operated continuously, the *P* drop over the same period was 2.4 bar, 2.4 bar and 2.5 bar. This series of experiments demonstrated that it was possible to change from a mixed to a diffusion and density-driven convection system by simply turning off the stirrer. The 0.3 bar *P* drop occurred over 460 s, which is approximately a 0.04 bar per 60 s rate of *P* decline, if a linear decline with time is assumed.

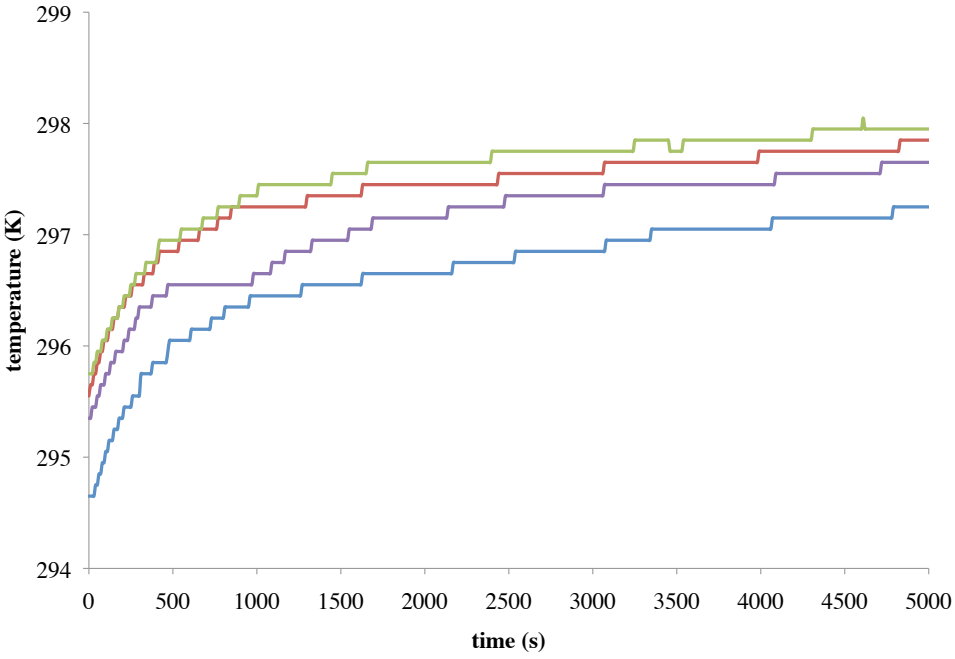

Figure 3.34: *T* versus time for the experiments discussed above

T recorded for the four experiments is shown in Figure 3.34. This shows that for the time period where the stirrer was turned off, 460 s to 920 s, the previous trend of *T* increase (purple curve) caused by dissolution and viscous dissipation also halted. Thus

the *P* change in this interval is due only to dissolution of CO_2, confirming that the mass transfer is slow enough to be neglected during the sampling procedure described next.

Prior to sample withdrawal, the fluid line was purged with de-ionized water and the pump piston run to the end of the cylinder, leaving zero volume remaining in the pump chamber. Samples were withdrawn from two locations in the *P* vessel. One location was from the bottom drain valve, sampling the bottom 30 cm^3, or 10%, of the aqueous phase. To sample close to the top of the aqueous phase, the liquid fill dip tube was modified. A small hole was drilled in the dip tube, 1.27×10^{-1} m from the top of the pressure vessel. This placed the sample point 2.5×10^{-2} m from the top of the aqueous phase. Assuming that the sample is drawn from the liquid above the sample point only, it sampled from the bottom portion of the top 25% of the aqueous phase, again samples of nominally 30 cm^3 were withdrawn. A choice was made to not sample the top of the aqueous phase, as this may have resulted in withdrawing vapor phase along with aqueous phase. Doing so would make the calculation of the CO_2 concentration very difficult.

Once an experiment reached 45.6 bar, the stirrer was turned off and the appropriate valves were opened to connect the selected sampling location of the *P* vessel to the syringe pump. The syringe pump was then run in refill mode at a constant rate of 30 cm^3/min. This process expanded the total system volume by approximately 5%, which resulted in a decrease in *P*. A calculation was made to check if this decreased *P* placed the aqueous phase above the bubble point; it did not. At the reduced *P* the CO_2 concentration was considerably below saturation and therefore it was assumed that CO_2 did not leave the aqueous phase during the sampling process. Once the 30 cm^3 samples were withdrawn, the valve on the pump was closed. Since the time taken to withdraw the

fluid (about one minute) could be expected to lead to only 0.04 bar of *P* decline due to continued CO_2 dissolution, it was assumed that no further CO_2 entered the aqueous phase during the sample acquisition. The volume in the pump was left unchanged for four hours to equilibrate the *T* of the fluid sample with that of the equipment. The 30 cm^3 sample remained a single phase under-saturated with CO_2. At four hours, the pump was again run in refill mode at a constant rate of 30 cm^3/min to expand the chamber volume to 60 cm^3. During this process the *P* was observed to decrease, then increase once more. The *P* was recorded each half hour for a period of two hours, at which time it was observed to have stabilized. With the syringe pump chamber expanded to 60 cm^3, two phases are present. There is a CO_2 saturated phase aqueous phase, for the small pressure prevailing, and a CO_2 rich vapor phase.

The calculation of the CO_2 concentration of the sample was made from the steady state *P* and volume, along with the volume of the sample withdrawn. The equilibrium CO_2 saturation of the aqueous phase of the sample at steady state *P* was determined using the tuned PR EOS flash calculation. The equilibrium aqueous phase volume was assumed to be equal to that of the sample drawn into the syringe pump, before expansion to evolve CO_2. This assumption neglects the small decrease in aqueous phase volume expected from the CO_2 evolving. Also neglected is the effect of *T* and *P* change on aqueous phase volume. The *T* change is small, a decrease of approximately 1 K. The *P* change is greater, 45.7 bar to a value in the range of 5 bar to 7 bar. This is a significant *P* change, though since water liquid is relatively incompressible, its effect on brine density can be neglected. For example, using the IAPWS-IF97 formulation for liquid water density, the reduction in density for liquid water at 45.7 bar to 5 bar is 0.2%. The density of the aqueous phase was therefore assumed to be 1 g/cm^3.

The equilibrium CO_2 saturation (calculated from the tuned PR EOS) and the aqueous phase mass (calculated from the measured sample volume) enabled calculation of the moles of CO_2 present in the aqueous phase. The vapor phase was assumed to be pure CO_2 since at ambient *T* the vapor *P* of H_2O is small. The *V* of CO_2 was calculated from the tuned PR EOS. The vapor phase volume was assumed to be the difference between the volume at nominally 60 cm^3 and the nominally 30 cm^3 volume of sample withdrawn. The *V* of CO_2 at the prevailing conditions and the phase volume allowed the moles of CO_2 in the vapor phase to be calculated. Adding the moles of CO_2 in the aqueous phase and the moles of CO_2 in the vapor phase determined the total number of moles in the sample at the conditions of withdrawal.

Before the CO_2 concentration in the sample could be calculated, a correction was made for the dilution of the sample by the dead volume. The dead volume is the internal volume of the *P* line that connects the reactor vessel and the syringe pump, plus the volume of the fittings. These volumes were calculated from the engineering drawings for the fittings and the line internal diameter. For samples withdrawn from the bottom of the pressure reactor, the dead volume was 6.4 cm^3. For samples withdrawn near the top of the aqueous phase, the dead volume was 5.8 cm^3. It was assumed that there was slug flow during sample withdrawal. Thus the nominally 30 cm^3 sample in the syringe pump was made up of 30 cm^3 minus the dead volume of CO_2 laden H_2O, plus the dead volume of pure H_2O.

The CO_2 concentrations calculated for each sample were then normalized to the ideal CO_2 concentration. The ideal CO_2 concentration was defined as that which would occur if the aqueous phase in the Parr vessel were perfectly mixed, that is, if there was

uniform concentration. To determine this ideal uniform CO_2 concentration at the intermediate sampling P, the moles of each CO_2 and H_2O in the system were calculated as follows. $P^{equilibrium}$ was taken from the average of the three experiments allowed to run to equilibrium with continuous stirring. At $P^{equilibrium}$, the equilibrium phase compositions were calculated using the tuned PR EOS flash calculation. The equilibrium vapor phase molar volume was calculated using the tuned PR EOS. The equilibrium aqueous phase density was determined using the model of Li *et al*. (2010). The volume of the vessel, measured to be 591 cm^3, and the mass of H_2O displaced were used to quantify the moles of H_2O in the reactor. This calculation is discussed in detail in section 3.5.3 'Data Processing Technique'.

Three repeats of the same experiment, using a stirrer speed of 23.3 rev/s were conducted. Samples were withdrawn from the bottom of the pressure reactor. The normalized CO_2 concentration calculated for these experiments was 87%, 93% and 90%. The range calculated from these repeats was used as a measure of the error in subsequent experiments.

Experiments were conducted at number of stirrer speeds from 3.3 rev/s to 30.3 rev/s in 6.7 rev/s increments. Two experiments were run for each stirrer speed, one where aqueous phase was sampled from the bottom of the pressure reactor and one where sampling was from near the top.

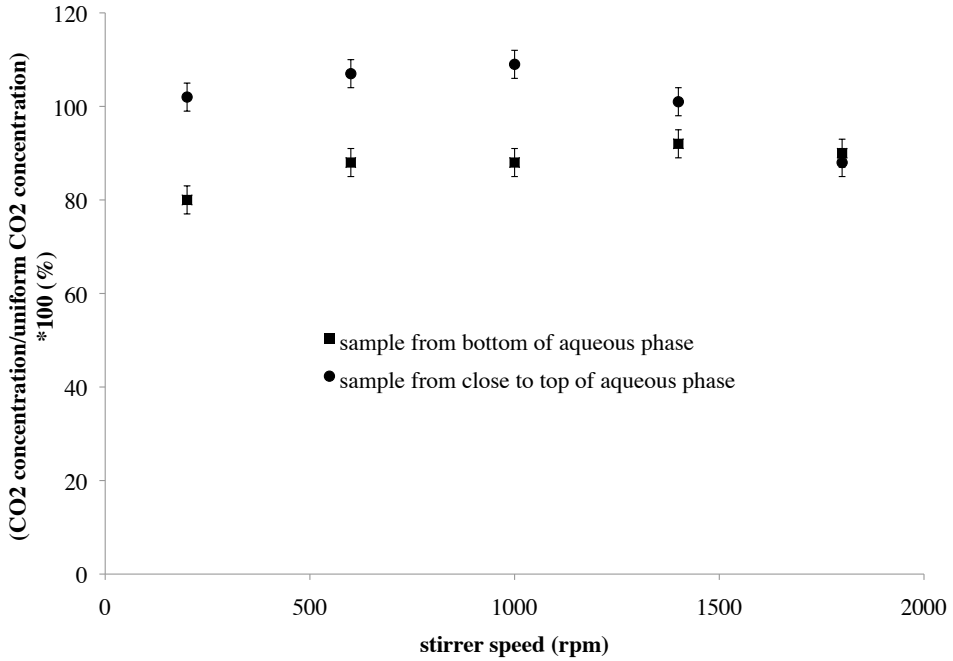

Figure 3.35: CO_2 concentration, normalized by ideal CO_2 concentration (see text), for aqueous phase samples withdrawn from the bottom and close to the top of the aqueous phase for various stirrer speeds during CO_2 dissolution experiments

It is apparent from Figure 3.35 that there is less difference in normalized concentration and thus more uniform mixing with increased stirrer speed. For a faster stirrer speed there is a reduced CO_2 concentration close to the top of the aqueous phase. Larger CO_2 concentration close to the top of the aqueous phase reduces the rate of mass transfer as it reduces the difference between the saturation value and the aqueous phase concentration at the CO_2/brine interface, which is the driving force for mass transfer. This result does not preclude the presence of gas entrainment. However, it does let us conclude that improved mixing does play a part in the observed shorter time to equilibrium of experiments conducted with a faster stirrer speed.

3.4.8 Effect of Wet CO_2 Density on Time to Equilibrium

Initially, a set of experiments was planned to quantify the effect of T, P, S_{NaCl} and S_{CaCl2} on k_L. A number of T controlled experiments was conducted at 308 K using de-ionized water. A range of P^o was selected to give $P^{equilibrium}$ of 20 bar to 100 bar. Approximately 295g of H_2O was displaced to establish initial conditions of equal phase volumes. A stirrer speed of 23.3 rev/s was used. The centerline of the impeller was approximately 3.4×10^{-2} m from the bottom of the vessel. Data were recorded every 10 s.

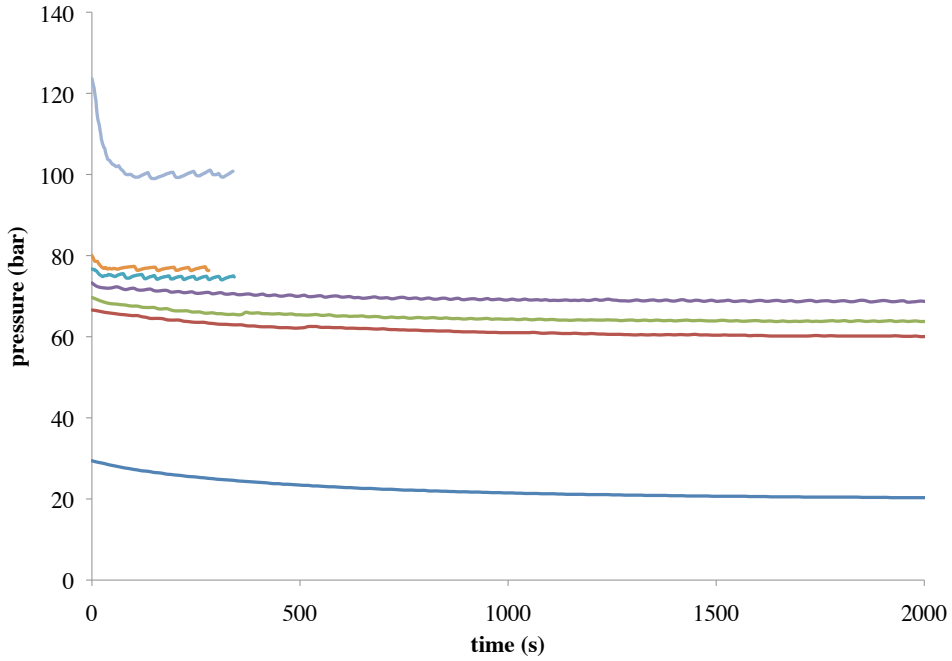

Figure 3.36: P versus time for experiments with various P^o values, T = 308 K

It is apparent from Figure 3.36 that the time to equilibrium is similar, approximately 1600 s, for experiments below a certain P of approximately 75 bar. Above this P, the experiments reach equilibrium in less than 100 s. The simplest explanation for this sudden decrease in time to equilibrium is that gas entrainment occurred. The

entrainment is presumed to happen more readily as the density of the vapor phase increases and thereby leads to a smaller difference between the aqueous and vapor phase densities. For the experiments above 75 bar, the wet CO_2 density was in excess of approximately 0.25 g/cm^3. An alternative explanation for the sudden decrease in time to equilibrium is that a pure CO_2 phase would exist as a supercritical phase at P above 75 bar but as a gas phase at smaller P. This distinction in itself is not thought to be the cause, however. Further evidence supporting this conclusion is presented below with the discussion of experiments conducted at 373 K.

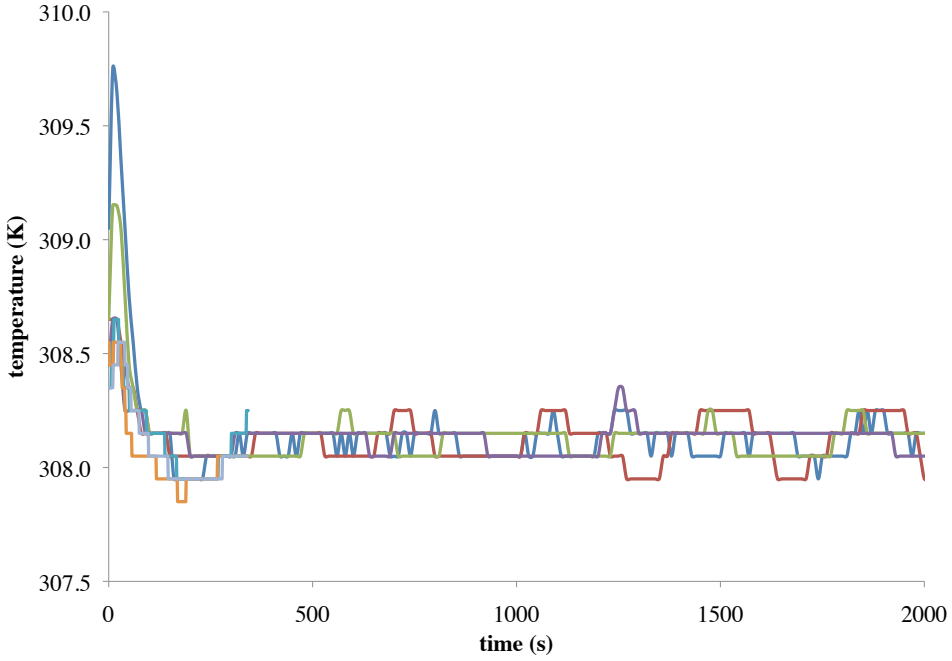

Figure 3.37: T versus time for experiments with various P^o values, T = 308 K

It is apparent from Figure 3.37 that there was an initial departure from isothermal conditions of approximately 2 K from the set point of 308 K. However, after a period of approximately 200 s, temperature control within approximately 0.5 K was achieved.

A number of T controlled experiments was conducted at 341 K and using de-ionized water. A range of P^o was selected to give $P^{equilibrium}$ of 20 bar to 100 bar. Approximately 292 g of water was displaced to establish initial conditions of equal phase volumes. A stirrer speed of 23.3 rev/s was used. The centerline of the impeller was approximately 3.4×10^{-2} m from the bottom of the vessel. Data were recorded every 10 s.

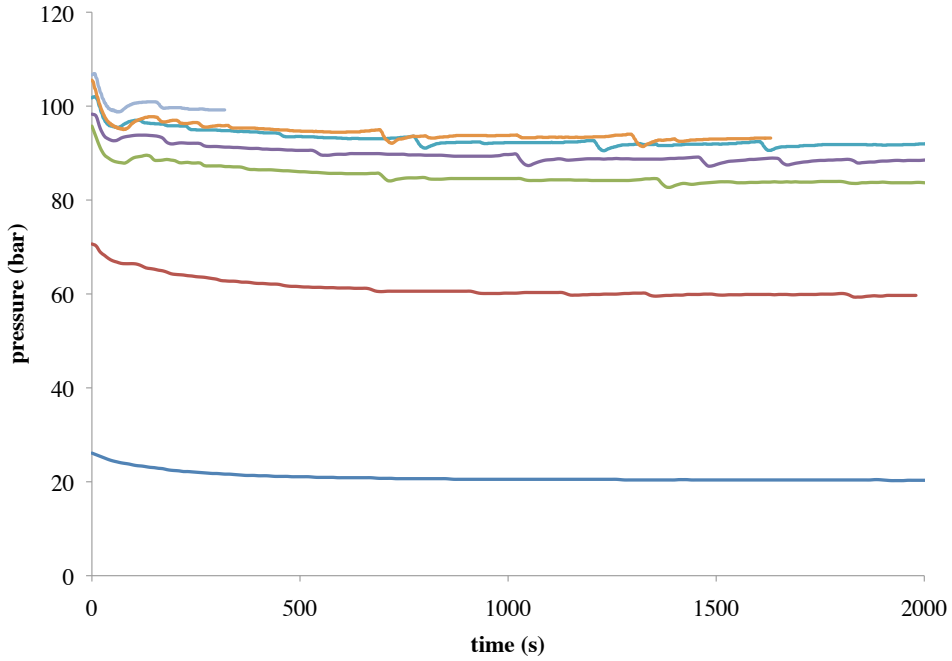

Figure 3.38: P versus time for experiments with various P^o values, T = 341 K

It is apparent from Figure 3.38 that the time to equilibrium is similar, approximately 1600 s, for all experiments. The density of wet CO_2 is 0.25 g/cm^3 for P greater than approximately 100 bar, conditions which prevail for only a small portion of time for the largest P experiments. For experiments at P over 90 bar there is an observable initial fast P drop and recovery, followed by a slow P drop over the remainder

of the experiment. The experiments at greater P also have intermittent periods of fast P drop and recovery.

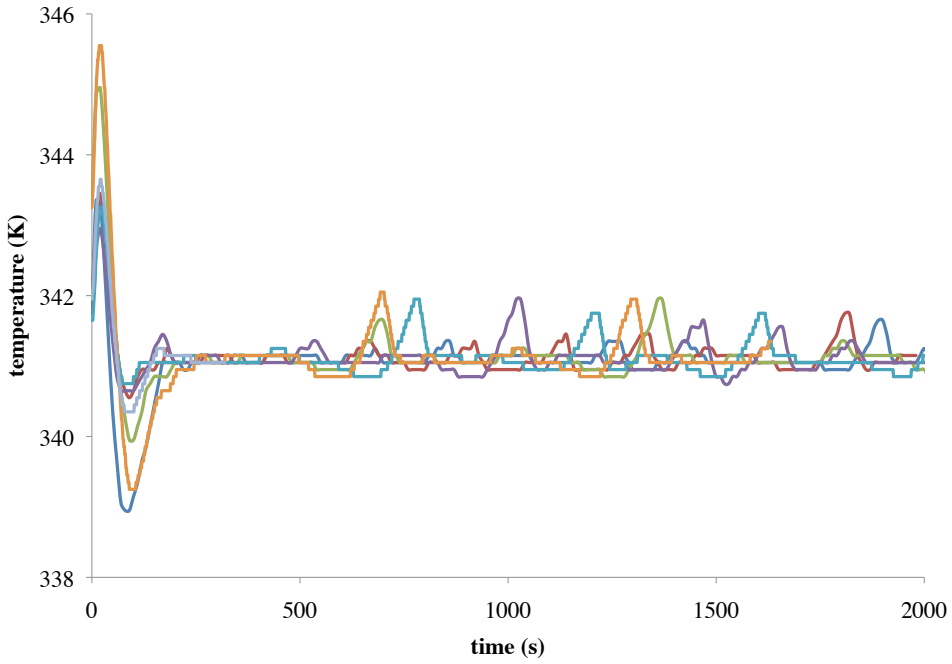

Figure 3.39: T versus time for experiments with various P^o values, T = 341 K

Similarly to the T versus time results for experiments conducted at 308 K presented in Figure 3.37, it is apparent from Figure 3.39 that there was an initial departure from isothermal conditions. The magnitude of the initial T disturbance was greater, approximately 6 K from the set point of 341 K. Again, after a period of approximately 200 s temperature control was achieved, though within larger limits, approximately 1 K. In the experiments conducted at greater P, there is a correlation between the fast P drop and recovery events and the deviations from isothermal conditions. Making the simplifying assumption that the aqueous phase is incompressible and of constant volume, the system P is governed by the vapor phase P. For a vapor

phase of constant volume, an increase in T will produce an increase in P for a constant V. Of course, prior to reaching equilibrium there is a net rate of CO_2 leaving the vapor phase and dissolving into the aqueous phase, which increases V and reduces P. Thus P is a function of competing factors; mass transfer of CO_2 driving a decrease and increased T driving an increase. If the system P increased, the T effect must have been dominant.

A number of T controlled experiments was conducted at 373 K and using de-ionized water. A range of P^o was selected to give $P^{equilibrium}$ of 20 bar to 100 bar. Approximately 284 g of water was displaced to establish initial conditions of equal phase volumes. A stirrer speed of 23.3 rev/s was used. The centerline of the impeller was approximately 3.4×10^{-2} m from the bottom of the vessel. Data were recorded every 10 s.

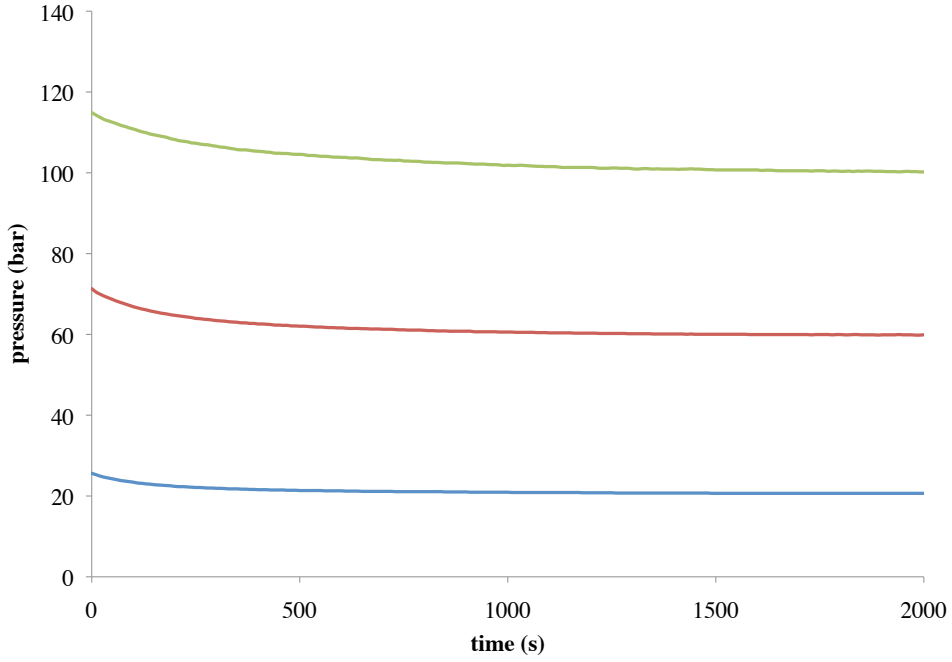

Figure 3.40: P versus time for a experiments with various P^o values, T = 373 K

Figure 3.40 shows the results of three experiments. For the two experiments conducted at smaller pressures, pure CO_2 would be in vapor phase. For the experiment at the largest pressure, pure CO_2 would be in supercritical phase. All three experiments reached equilibrium in approximately 1600 s. In contrast to the experiments conducted at 308 K, there was not the step change in the time to equilibrium coincidental with a change from vapor to supercritical phase CO_2. The wet CO_2 density was less than 0.25 g/cm^3 for all three experiments, reinforcing the conclusion that the inferred flow regime change at T = 308 K was the result of a reduced density difference between the phases.

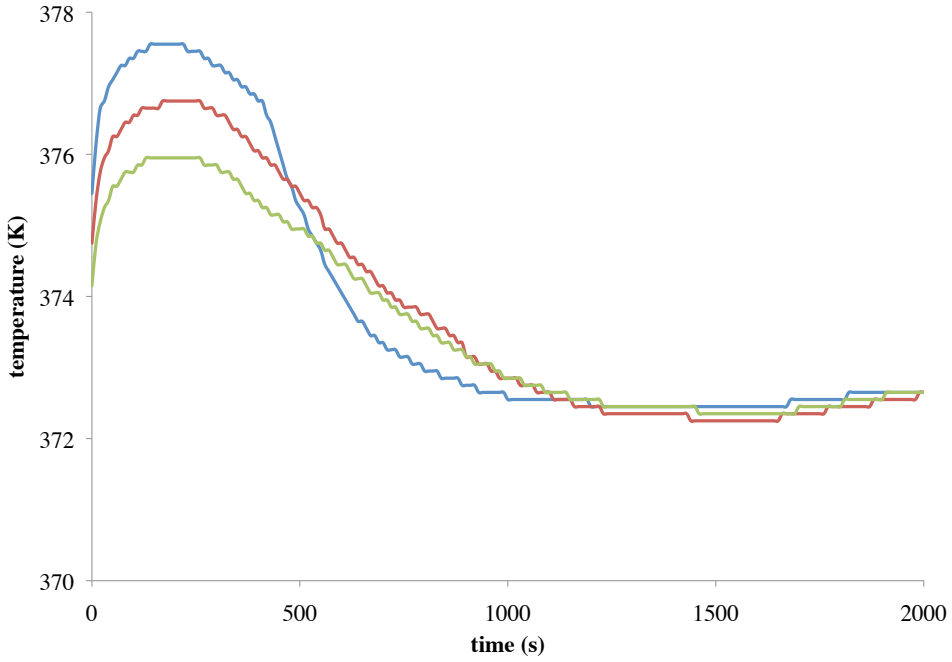

Figure 3.41: T versus time for experiments with various P^o values, T = 373 K

Figure 3.41 shows that despite operating the stirred reactor with the heating and cooling systems activated, T control was very poor. It appears that the cooling loop did not switch on at all. The experiments could not be accurately described as taking place at

isothermal conditions. Since isothermal conditions were required for the designed experiment, an upper limit of 363 K was found where sufficient heating and cooling were available from the stirred reactor and its control system.

3.4.9 Conclusions From Scoping Experimental Investigation

Stirred experiments were found to be repeatable and a stirrer speed of 16.7 rev/s reduced the time taken to reach equilibrium by approximately a factor of ten over an unstirred experiment. For experiments conducted at ambient T, there was a measureable T increase observed due to the heat of dissolution for CO_2 in H_2O. For larger stirrer speeds, there was also a measureable increase in T due to viscous dissipation. The time taken to reach equilibrium was found to be approximately equal for S_{NaCl} of 0.0 m to 4.0 m.

Use of a gas entrainment impeller was found to reduce the time to equilibrium by approximately a factor of 300 over the impeller. When comparing the gas entrainment impeller and impeller experiments in isolation, an increase in a of 300 would be inferred. However, the experiments were conducted at 16.7 rev/s, which is considerably lower than the 30.0 rev/s shown to produce a uniform CO_2 concentration in the fluid sampling experiments. At 16.7 rev/s the experiments with the stirrer would not be expected to have a uniform CO_2 concentration. The experiments with the gas entrainment impeller would likely have produced a uniform CO_2 concentration since CO_2 bubbles were sparged through the aqueous phase from the bottom. If this is the case, the inference made of the 300-fold increase in a is not accurate. Examining the P versus time for different stirrer speeds in Figure 3.31 indicates that the time to equilibrium for an experiment at 16.7 rev/s is approximately 2.5 times as long as an experiment at 30.0 rev/s. With this factor

taken into account, the difference in the time taken to equilibrium between the stirrer and gas entrainment impeller experiments would be of the order of 100.

The flow visualization experiments demonstrated that for an air and H_2O system at small *P* and stirred by a dual impeller, gas entrainment was observed at 10.0 rev/s and above. With a single impeller placed close to the bottom of the vessel and stirrer speeds up to the maximum available, 30.0 rev/s, there was not visible gas entrainment. With the impeller further away from the bottom of the vessel, an occasional gas bubble was observed at 30.0 rev/s. The baffle unit was shown to have no effect on gas entrainment. Without the baffle unit fitted, the vessel was observed to be effectively baffled by other hardware within the vessel, and no large central vortex was formed under any conditions.

A stirrer speed conservatively below the 10.0 rev/s for the onset of gas entrainment, 8.3 rev/s, was selected for a CO_2 and H_2O dual impeller stirred experiment. The time to equilibrium for this experiment was far longer than single impeller configurations, which could be operated at faster stirrer speeds. A single impeller further from the bottom of the vessel operated at 23.3 rev/s reached equilibrium over the same time period as a single impeller close to the bottom of the vessel operated at 30.0 rev/s.

A faster stirrer speed was shown to lead to a shorter time to equilibrium than a slower stirrer speed for otherwise identical CO_2 and H_2O experiments. Fluid sampling demonstrated that a faster stirrer speed led to a more uniformly mixed aqueous phase. There was elimination of CO_2 concentration gradient within the aqueous phase at 30.0 rev/s. Experiments across the *T* and *P* sample space indicated that in cases where the wet CO_2 density exceeded 0.25 g/cm^3, there was a change of flow regime to one of gas

entrainment. Attributing this observation to the phase density is reasonable, because the only other factor was the change from vapor phase to supercritical phase CO_2, and supercritical phase CO_2 experiments at $T = 373$ K did not show evidence of a step change decrease in time to equilibrium compared to vapor phase experiments.

3.5 Designed Experiment Results

3.5.1 Parameters

Considering the application to surface dissolution, several operating parameters are particular to each specific site. These are T, P and brine composition. In most cases the brine composition is fixed. That is, the brine available would not be altered by desalination or dilution, for example. One case where there may potentially be some flexibility to alter the salinity of brine is the use of effluent from a desalination plant. Within limits, the T and P are variable operating parameters.

As discussed by Burton (2008), to ensure that CO_2 remains in solution when stored, the CO_2 concentration produced at the mixing facility must be less than or equal to the solubility at conditions in the target aquifer. Across the range of interest in most applications, CO_2 solubility in brine increases with increasing P and decreasing T. However, there is a trend reversal for very large T and P conditions, as shown in the plot below, produced from the model of Duan and Sun (2003).

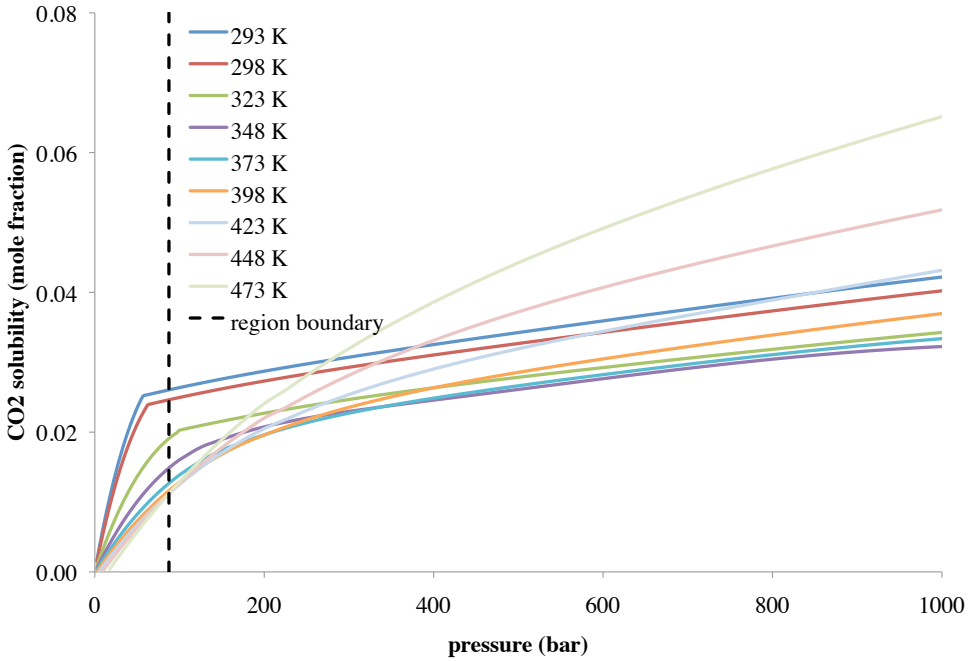

Figure 3.42: CO_2 solubility in pure H_2O versus P for various T, model results from Duan and Sun (2003)

Figure 3.42 shows CO_2 solubility in pure water. The trends show that at conditions at or greater than 87.5 bar, the CO_2 solubility is reduced with greater T, but only to 348 K, at T over 348 K the CO_2 solubility then increases with increasing T. The trend is the same for NaCl brines, for which data were included in Appendix E. It should be noted that the precise T and P where this trend reversal occurs was not determined. Rather, the calculated CO_2 solubility for discrete values of T and P, as shown in Figure 3.42, were compared. Increments in P were 2.5 bar to 100 bar and 25 bar from 100 bar to 1000 bar. The increments in T were 25 K. This trend would only need to be taken into account in the most extreme reservoir conditions. For the present discussion, we will consider only the T and P range where CO_2 solubility increases with increasing P and decreasing T. For large T reservoirs this region is limited to a P of 87.5 bar, as observed in Figure 3.42. Alternatively, for reservoirs at less than 348 K, Figure 3.42 shows that

there is no reversal of the CO_2 solubility trend even up to a P of 1000 bar, which corresponds to the hydrostatic pressure of the deepest wells yet drilled (BP, 2012). At surface, after lifting from the target aquifer, it is reasonable to assume that brine will be at a smaller T relative to the subsurface. This allows the mixing facility to be operated at a smaller P to achieve the same solubility. There is a further constraint, the wellhead P is limited by the downhole injection P that would cause fracture of the storage formation. To quantify the effect that each of the parameters P, T and S has on k_L, appropriate ranges of each were selected to define the parameter space for experiments.

To reflect the range of brine and effluent composition that may be available for the application, a simplified approach to the preparation of synthetic brines was taken. The presence of monovalent and divalent cations was considered. Monovalent cation concentration representative of seawater, through to that of the concentrated effluent from a desalination plant was replicated by the range of S_{NaCl} selected. To account for brines that do and those that do not have divalent cations present, a representative concentration of $CaCl_2$ was used in the preparation of some brine. The composition of formation brines published by Xu *et al*. (2010), Xu *et al*. (2006) and Cipolli *et al*. (2004) was used to establish a realistic upper limit. The T range selected was determined from the expected range of surface conditions and practical considerations related to the temperature control system of the pressure reactor (described in section 3.4.8 'Effect of wet CO_2 Density on Time to Equilibrium'). Initially, a P range of interest was defined between 20 bar and 100 bar, reflecting the range of depths likely to be used for storage by surface dissolution. Investigative experiments (covered in section 3.4.8) led to the conclusion that for a wet CO_2 density in excess of 0.25 g/cm^3, there was a change in flow regime to the onset of gas entrainment. As a result, wet CO_2 density was used as an independent variable in

place of P, and an upper limit selected to avoid the range in which the flow regime was different. The values for each parameter are shown in Table 3.2.

Parameter	Symbol	Small value	Large value
Temperature (K)	T	308	363
Wet CO_2 density (g/cm^3)	$\rho_{wet\ CO2}$	0.041	0.187
NaCl salinity (m)	S_{NaCl}	0.6	4.0
$CaCl_2$ salinity (m)	S_{CaCl2}	0.0	0.2

Table 3.2: Range of experimental parameters

3.5.2 Designed Experiment

To evaluate the response of k_L to changes in each of the parameters considered, a designed experiment was conducted. With four factors to each be evaluated at two levels, a full factorial approach required sixteen experiments. Six centerpoint repeats were conducted to allow for a measure of repeatability. Each of these experiments is shown in Table 3.3, below.

Experiment	T (K)	$\rho_{wet\ CO2}$ (g/cm^3)	S_{NaCl} (m)	S_{CaCl2} (m)
1	308	0.041	0.6	0.0
2	308	0.041	0.6	0.2
3	308	0.041	4.0	0.0
4	308	0.041	4.0	0.2
5	308	0.187	0.6	0.0
6	308	0.187	0.6	0.2
7	308	0.187	4.0	0.0
8	308	0.187	4.0	0.2
9	363	0.041	0.6	0.0
10	363	0.041	0.6	0.2
11	363	0.041	4.0	0.0
12	363	0.041	4.0	0.2
13	363	0.187	0.6	0.0
14	363	0.187	0.6	0.2
15	363	0.187	4.0	0.0
16	363	0.187	4.0	0.2
17 (center point)	336	0.114	2.3	0.1

Table 3.3: Designed experiment parameters for each experiment

The experiments were run in a randomized order, with the exception of *T*. Since the accumulator required a considerable period of time to reach the *T* set point, experiments at each *T* were run in groups before changing the *T* setting.

3.5.3 Data Processing Technique

To calculate k_L for each of the twenty-two experiments, a numerical approach was used, employing the models discussed above. That is, a tuned PR EOS was used for vapor phase volumetric data calculation and flash calculation, while the aqueous phase density was calculated using the model of Li *et al*. (2011).

The calculation was made assuming isothermal conditions, with the *T* calculated from an average of that recorded during the particular experiment. The brine density in the vessel prior to displacement was calculated from the model of Li *et al*. (2011). From the brine density calculated and the measured volume of the vessel, 591 cm^3, the mass of brine in the vessel prior to displacement was calculated. The mass of brine remaining in the vessel after displacement was determined by subtracting the mass displaced to the beaker on the balance during establishment of initial conditions. From the weight percent of each component of the brine, as prepared, the mass and moles of H_2O in the system was calculated. The notation N_{H2O} was used for the number of moles of H_2O in the system.

A high order polynomial trend-line was fitted to the *P* versus time data for each experiment. This was done to reduce noise effects that may result from taking a

derivative of the raw data. An example of this process is shown for Experiment 1 in Figure 3.43.

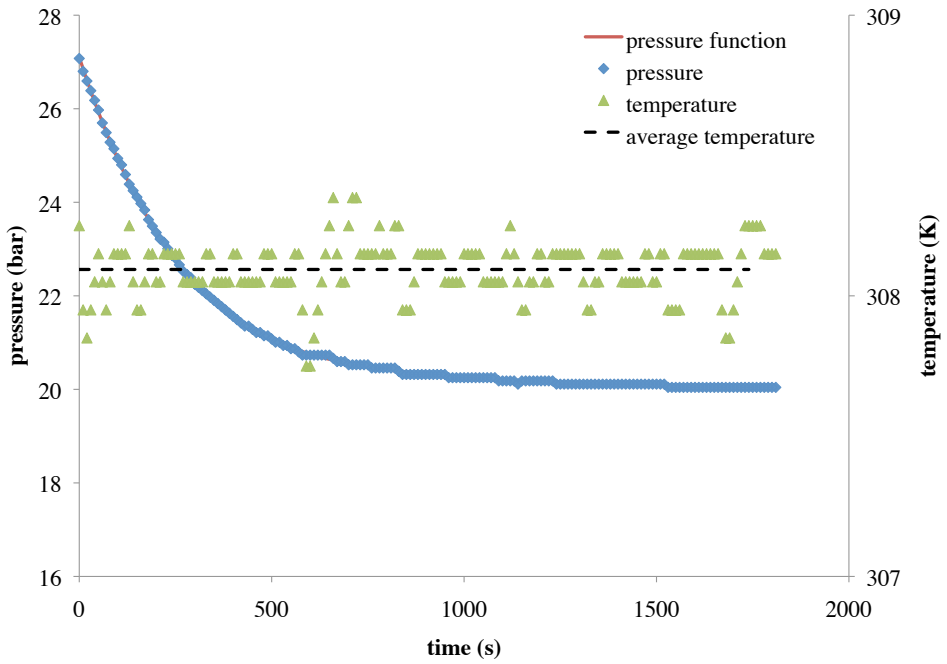

Figure 3.43: *P* and *T* versus time for Experiment 1. The smooth red curve is the *P* trend-line, while the dashed black line is the average *T*.

From the *P* trend-line fitted to the data of each experiment, *P* was calculated versus time at discrete intervals of 10 s. This calculated *P* is shown by the trend 'pressure function' in Figure 3.43.

A tuned PR EOS flash calculation was done at $P^{equilibrium}$ to determine x_{CO2}, x_{H2O}, y_{CO2} and y_{H2O}. N_{H2O} was known from the mass balance calculation described above. The equilibrium vapor phase molar volume V_V was calculated from the tuned PR EOS. The equilibrium aqueous phase density was calculated via the model of Li *et al*. (2011). This

allowed the calculation of the number of moles of CO_2 in the vessel N_{CO2}. For a two-phase system, two equally valid equations for the number of moles of vapor phase N_V are given by Equation 3.9a and 3.9b.

$$N_V = \frac{Volume_V}{V_V} \qquad \text{Equation 3.9a}$$

with vapor phase volume $Volume_V$ (dm^3).

$$N_V = (1 - n_L)N_{total} \qquad \text{Equation 3.9b}$$

with the total moles of CO_2 and H_2O in the system N_{total}. A function was defined as the quotient of N_V calculated by each Equation 3.9a and 3.9b, as a percentage. This was set to 100 % by changing N_{CO2} via the Excel 'goalseek' function. $Volume_V$ in Equation 3.9a is calculated from Equation 3.9c:

$$Volume_{total} = Volume_V + Volume_L \qquad \text{Equation 3.9c}$$

with total system volume $Volume_{total}$ (dm^3) (measured and fixed at 591 cm^3) and aqueous phase volume $Volume_L$ (dm^3). $Volume_L$ is by definition the quotient of the mass of the aqueous phase and density of the aqueous phase. The mass of the aqueous phase is the sum of the mass of all components, H_2O, CO_2, NaCl and $CaCl_2$ (if present). There is assumed to be no transfer of salt to the vapor phase. Thus the mass of each salt is known from the molality of the prepared synthetic brine. The mass of H_2O and CO_2 in the aqueous phase are determined from the moles of each N_{iL}, which in turn are calculated from Equation 3.9d:

$$N_{iL} = N_{total} n_L x_i \qquad \text{Equation 3.9d}$$

with moles of component i in the aqueous phase N_{iL}. For a two-phase system, the following relation between mole fractions holds by definition:

$$z_i = n_L x_i + n_V y_i \qquad \text{Equation 3.9e}$$

which can be rearranged to yield Equation 3.9f using CO_2 mole fractions:

$$n_L = \frac{z_{CO_2} - y_{CO_2}}{x_{CO_2} - y_{CO_2}}$$ Equation 3.9f

The definition of z_{CO2} is given in Equation 3.9g.

$$z_{CO_2} = \frac{N_{CO_2}}{N_{CO_2} + N_{H_2O}}$$ Equation 3.9g

An assumption was made that the small quantity of H_2O that moves to the vapor phase occurs instantaneously on the establishment of initial conditions. This assumption is based on the order of magnitude difference between diffusion coefficients in vapor phase and liquid phase, as shown by comparing the results of Pritchard and Currie (1982) to Tamimi et al. (1994). As a result of this assumption, the pressure drop observed between P^o and $P^{equilibrium}$ was attributed to only the net mass transfer of CO_2 to the aqueous phase, with no contribution from net mass transfer of H_2O to the vapor phase. It was also assumed that there was a uniform concentration of CO_2 in the aqueous phase at all times, which is based on experiments detailed in section 3.4.7 'Aqueous Phase Sampling Experiments'. It follows that the kinetics were governed by Equation 2.4b.

At each discrete time step, for which the measured *P* is known, a tuned PR EOS flash calculation was made. The *T* versus time data for each experiment were examined to select the time at which the *T* had returned to the set point after the initial departure from isothermal conditions, as shown for the investigative experiments in Figures 3.37 and 3.39. To avoid eliminating a large portion of the *P* drop data for a number of experiments, the point selected was often before the complete return to isothermal conditions. However, the point selected was always after the minimum *T* and as such there is a portion of data included in the analysis where *T* increases back to the set point. This heat transfer effect is a competing effect, which reduces the *P* drop that would be

otherwise apparent from the mass transfer process alone at isothermal conditions. As a result, the k_L calculated from this portion of the data is conservative or smaller than it would be if an ideal experiment at precisely isothermal conditions could be conducted. This criteria was used to select the time = 0 s point for each experiment and data were presented from this time. The complete raw data for the twenty-one experiments not presented in Figure 3.4.3 is included in Appendix F.

Using the liquid phase density model of Li *et al*. (2011), the saturation CO_2 concentration at each time step was calculated. x_{CO2} at equilibrium for the instantaneous P was determined from the tuned PR EOS flash. There was assumed to be a fixed N_{H2OL}, calculated from Equation 16, throughout the experiment as per the assumption discussed above. N_{CO2L} at equilibrium for the instantaneous P is calculated by Equation 3.9h:

$$N_{CO_2L} = \frac{N_{H_2OL}}{\frac{1}{x_{CO_2}} - 1} \qquad \text{Equation 3.9h}$$

The total mass and volume of the aqueous phase are calculated as above for equilibrium conditions. Finally, the saturation CO_2 concentration $C_{CO_2saturation}$ is calculated by definition using Equation 3.9i.

$$C_{CO_2saturation} = \frac{N_{CO_2L}}{Volume_L} \qquad \text{Equation 3.9i}$$

As an experiment progresses and P declines, $C_{CO_2saturation}$ also declines.

The number of moles of CO_2 that is in each phase is calculated at each time step as described in preceding paragraphs. From the number of moles of CO_2 in the aqueous phase and the liquid density model of Li *et al*. (2011), the instantaneous CO_2 concentration $C_{CO_2\delta}$ was calculated. As the experiment progresses the instantaneous CO_2

concentration increases. The difference between the instantaneous CO_2 concentration and saturation CO_2 concentration, $C_{CO_2 saturation} - C_{CO_2 \delta}$, is the driving force for the mass transfer. As an experiment progresses this difference declines to zero. An example of this calculation for Experiment 1 is shown in Figure 3.44a.

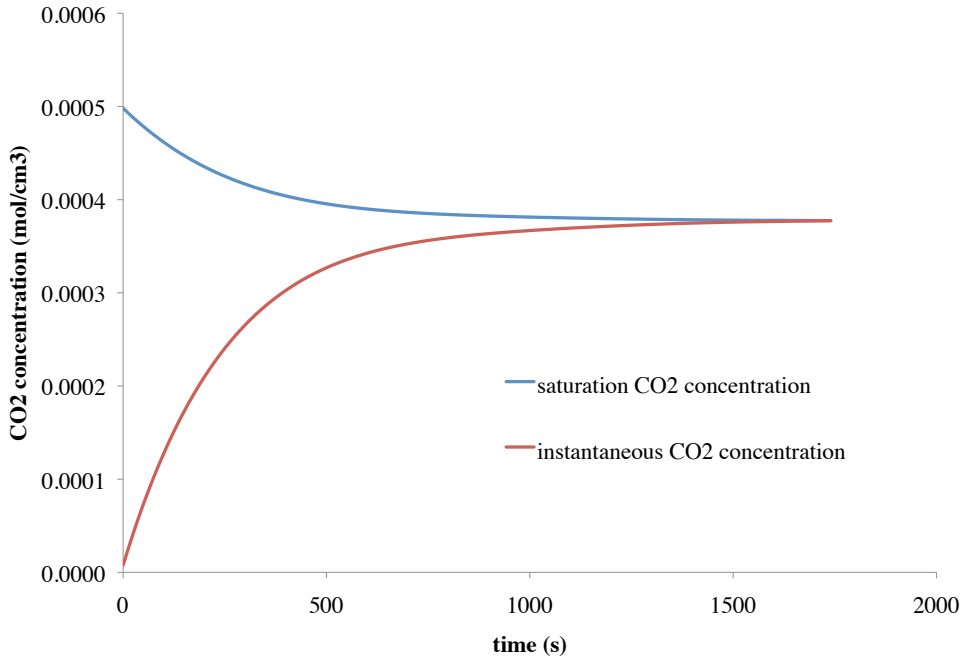

Figure 3.44a: Saturation and instantaneous CO_2 concentration versus time for Experiment 1. "Saturation" refers to the equilibrium value at the T of the experiment and the P at any given time; "instantaneous" refers to the concentration of CO_2 in the aqueous phase at that time, assuming well-mixed aqueous phase and computed from the P at that time.

As discussed in detail above, $C_{CO_2 saturation}$ is calculated from a *P* taken from the smoothed 'pressure function' at the relevant time step and the average *T*, along with the other required inputs. Both the 'pressure function' and average *T* are shown for each experiment in Figure 3.43 and Appendix F. At the point in each experiment where the

representative k_L was selected, as per the method discussed below, the variation in actual measured P and T was examined to identify which experiment exhibited the greatest departure from the 'pressure function' and average T, and was closest to equilibrium in terms of percentage of CO_2 dissolved. Experiment 5 was identified and a calculation of $C_{CO_2 saturation}$ made using the actual P and T for nine points, four before, one at and four after the point at which the representative k_L was selected. Comparison of Figure 3.44b with the data recorded for the experiment (see Appendix F) shows that this interval corresponds to one cycle of the 'sawtooth' pattern in the P-T history. The $C_{CO_2 saturation}$ calculated by this approach is shown in Figure 3.44b.

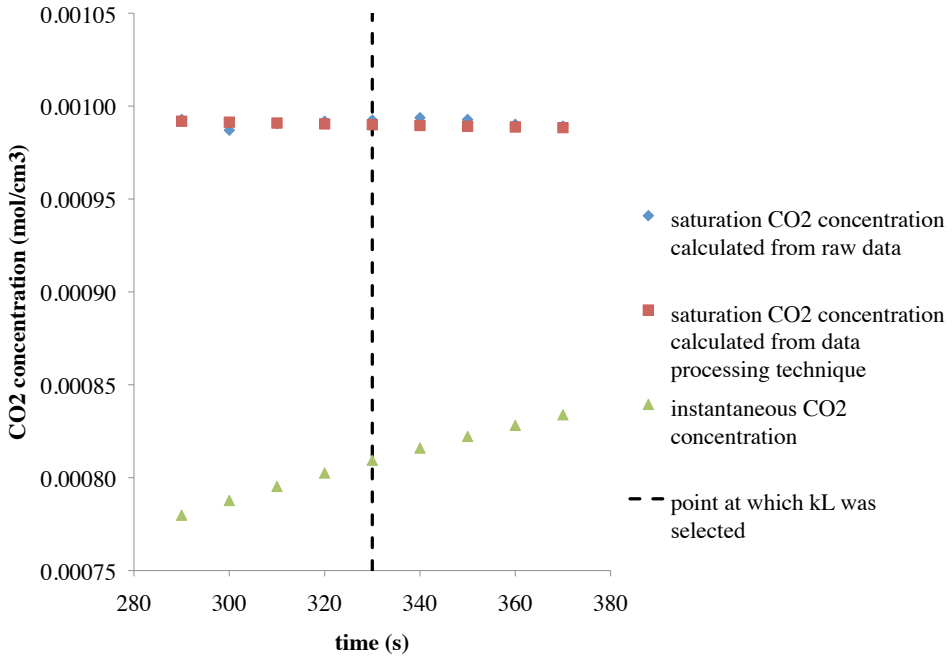

Figure 3.44b: Saturation CO_2 concentration calculated from raw data (blue points) and via data processing technique (red points) versus time for Experiment 5. Instantaneous CO_2 concentration also shown (green points).

Figure 3.44b shows that $C_{CO_2 saturation}$ calculated using the raw data and alternatively by the data processing technique described match very well. Further, using either approach always results in a CO_2 concentration greater than $C_{CO_2 \delta}$, which means the mass transfer is always of CO_2 from the vapor to the aqueous phase. This result demonstrates that the smoothing of the *P* data and averaging of the *T* data adequately reflects the true data.

The net rate of CO_2 mass transport versus time, $\frac{dn}{dt}$, was calculated from the numerical derivative of the number of moles of CO_2 in the aqueous phase. An example of this calculation for Experiment 1 is shown in Figure 3.45.

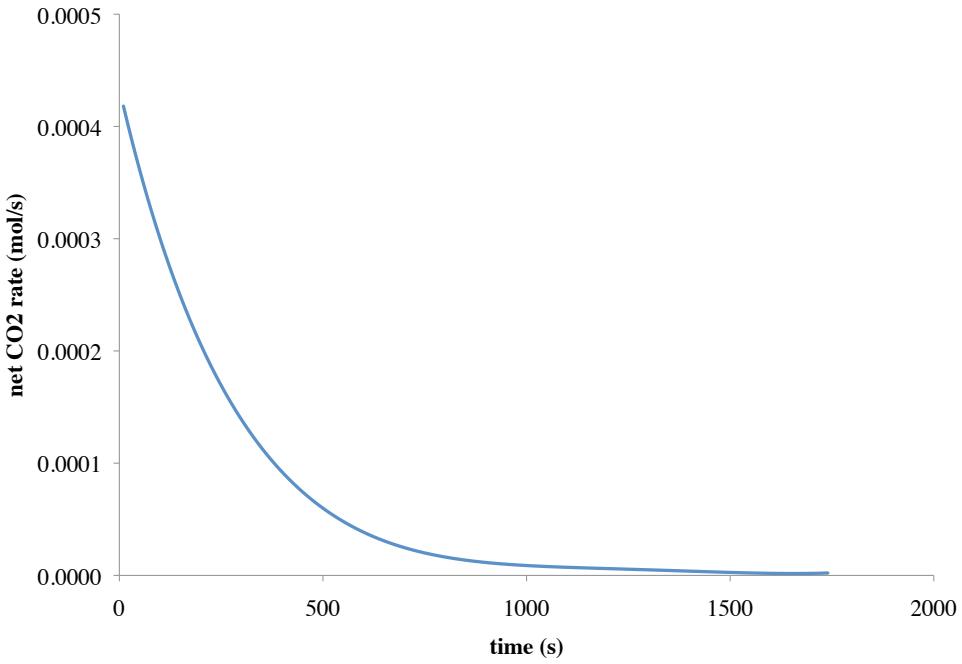

Figure 3.45: Net rate of CO_2 dissolution versus time for Experiment 1

With $\frac{dn}{dt}$ and $C_{CO_2 saturation} - C_{CO_2 \delta}$ calculated, rearrangement of Equation 2.4b allows for calculation of k_L. An example of this for Experiment 1 is shown in Figure 3.46.

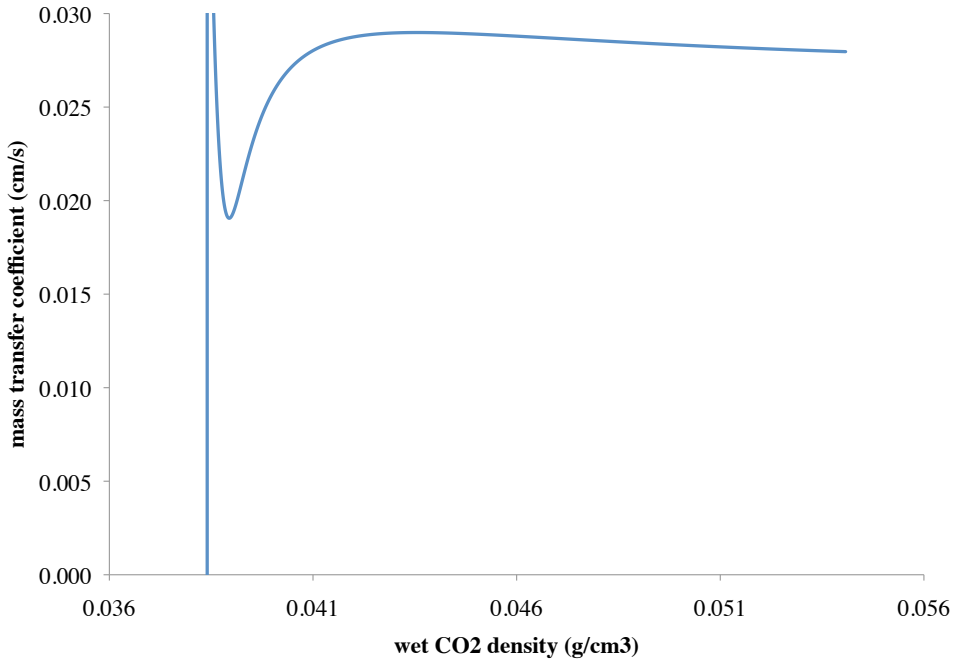

Figure 3.46: k_L versus $\rho_{wet\ CO2}$ for Experiment 1

Density decreases with time, so the progress of the experiment is from right to left in Figure 3.46. At first glance Figure 3.46 indicates that k_L is relatively constant with respect to $\rho_{wet\ CO2}$, though it becomes very large then very small for small changes in CO_2 density toward the end of the experiment. This behavior was observed processing each experiment, which ended at different values of $\rho_{wet\ CO2}$. The erratic changes occur only in

the part of experiment where both $\frac{dn}{dt}$ and $C_{CO_2 saturation} - C_{CO_2 \delta}$ are very small and can be considered noise.

A number of calculations are made in the data processing of each experiment, for example the values of the aqueous phase density and volume, vapor phase molar volume and CO_2 dissolved as a percentage of the equilibrium CO_2 concentration. These are shown below for Experiment 1.

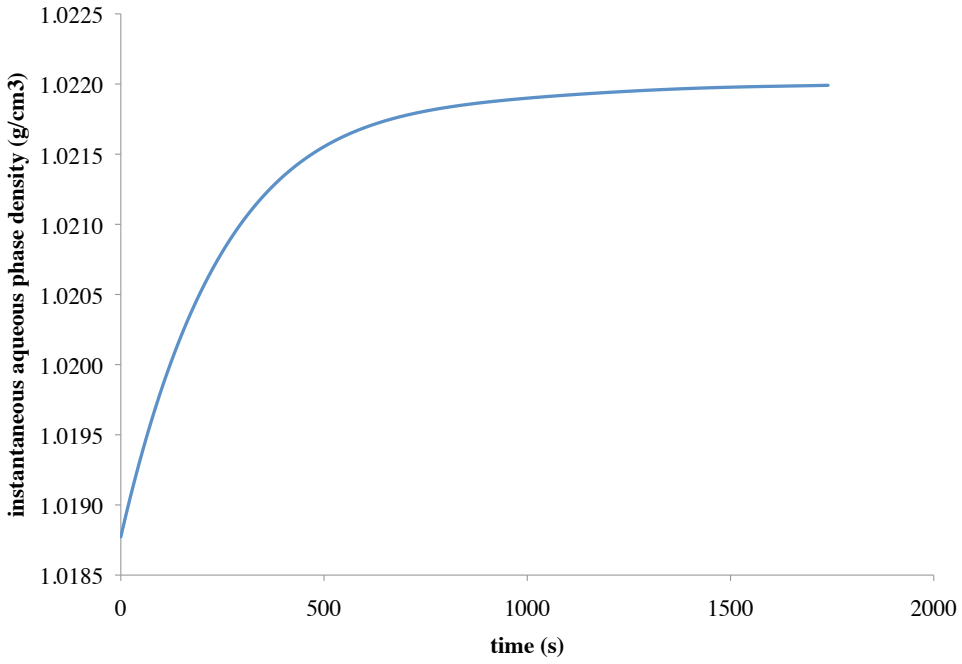

Figure 3.47: Instantaneous aqueous phase density versus time for Experiment 1

The increase in aqueous phase density over the duration of Experiment 1 is very small, only 0.3%, as shown in Figure 3.47. Two competing factors contribute to the density change, the change in P and the change in x_{CO2}. As the experiment progresses, there is a decrease in P. If all other factors were equal, this would lead to a very small

decrease in density. However, the accumulation of CO_2 over the duration of the experiment, an increase in x_{CO2}, would lead to an increase in density if all other factors were equal. Since there is a net increase in density, it can be concluded that the x_{CO2} effect dominates the P effect.

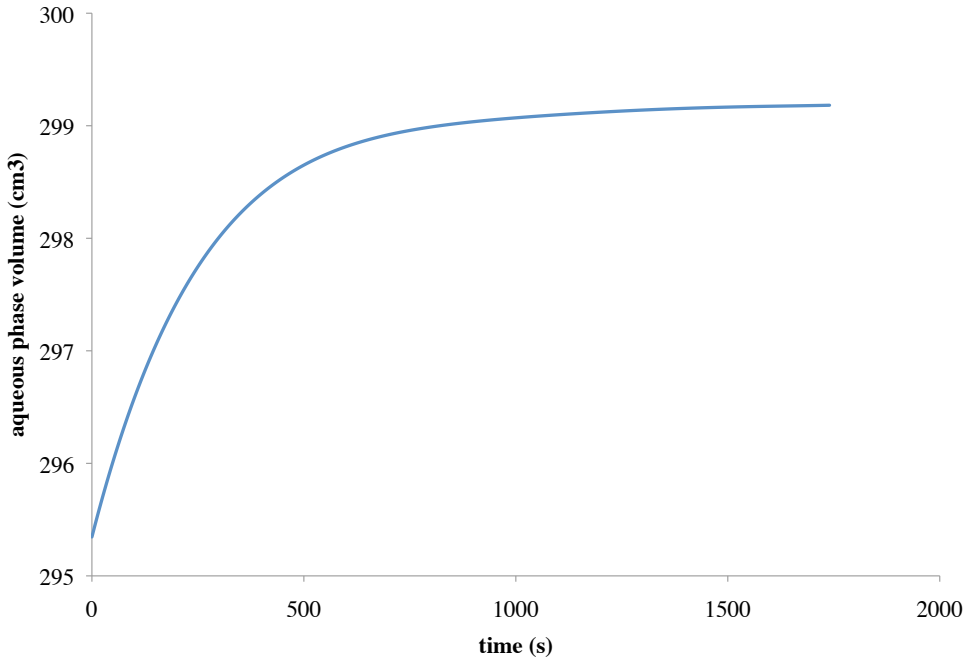

Figure 3.48: Aqueous phase volume versus time for Experiment 1

Figure 3.48 demonstrates that the increase in aqueous phase volume over the duration of Experiment 1 is 1.3%. There are two effects contributing to this change, the change in aqueous phase density and the change in amount of the phase. While the aqueous phase density is slightly reduced, as shown in Figure 3.47, there is an increase in

the number of moles of CO_2. The number of moles of CO_2 increases from 0.002 mol to 0.113 mol, an addition of 4.87 g.

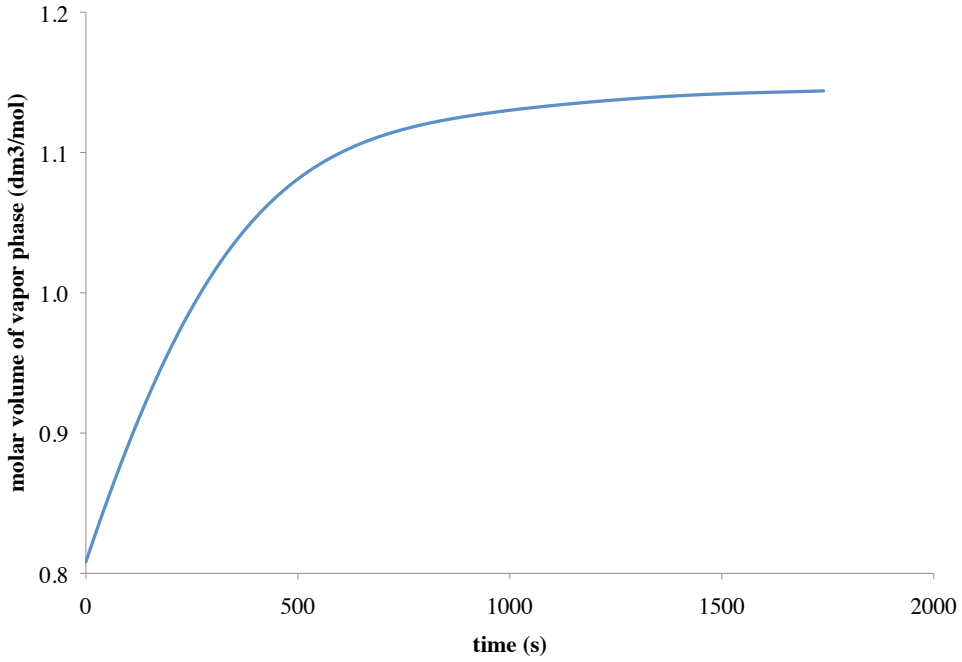

Figure 3.49: Vapor phase molar volume versus time for Experiment 1

Figure 3.49 shows that there is a far larger increase in the vapor phase molar volume than in the aqueous phase density, for Experiment 1. The change over the duration of the experiment is 41.5%. Even with the reduction in the volume of the vapor phase, as shown by the increase in the volume of the aqueous phase demonstrated in Figure 3.48, the vapor phase molar volume increase is the most significant factor in the decrease in *P* over the duration of an experiment.

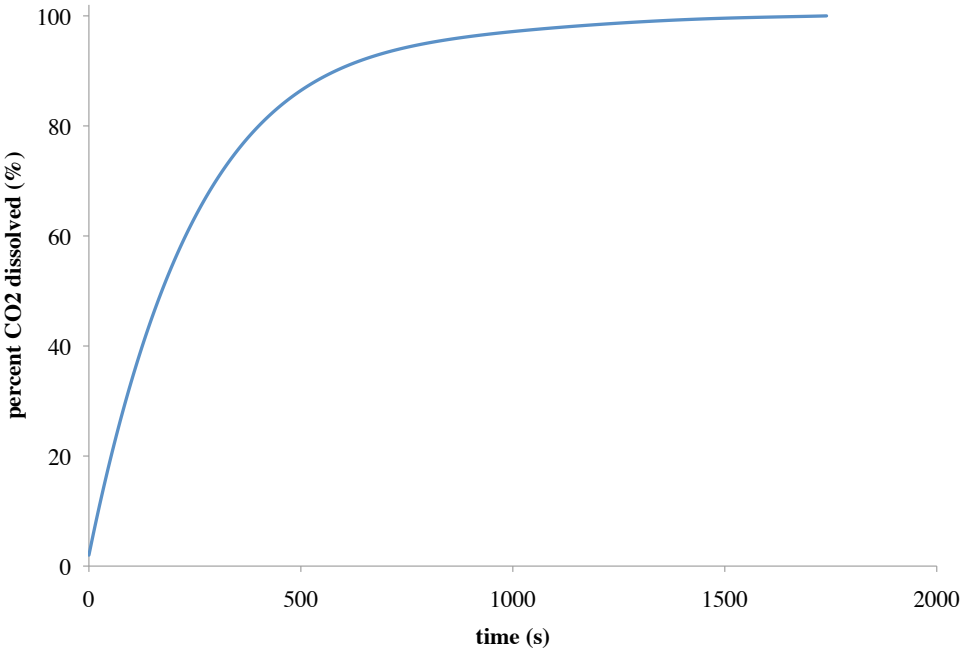

Figure 3.50: Percent CO_2 dissolved versus time for Experiment 1

Figure 3.50 shows the percent of CO_2 dissolved over the course of Experiment 1. At 600 s over 90% of the final equilibrium number of moles of CO_2 has been transported.

3.5.4 Discussion of Results

The twenty-two experiments were completed and processed with the results shown in the Figures 3.51, 3.52 and 3.53.

3.5.4.1 Small Wet CO_2 Density Results

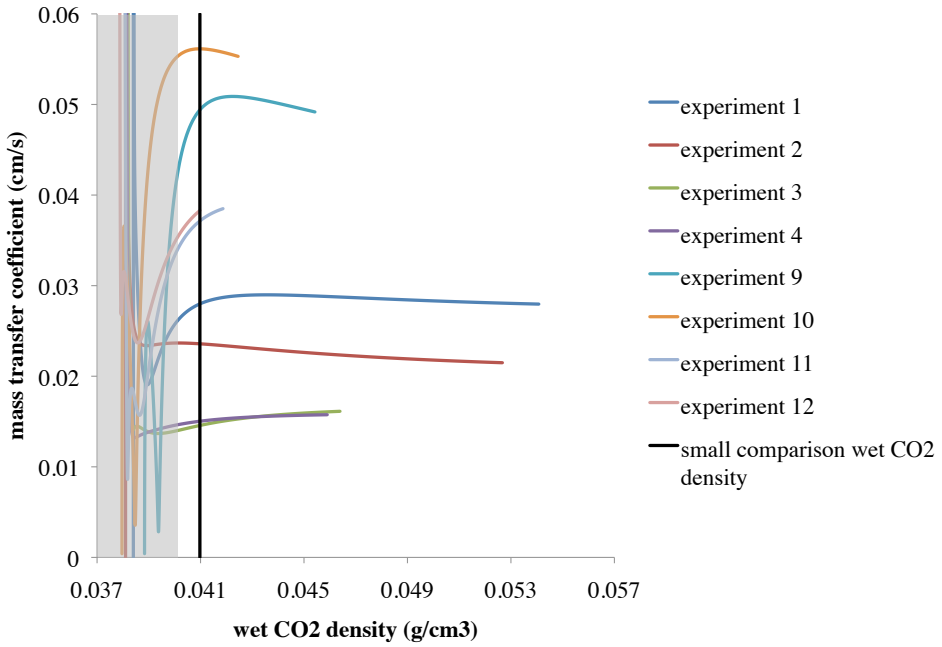

Figure 3.51: k_L versus $\rho_{wet\ CO2}$ for small $\rho_{wet\ CO2}$ experiments. The vertical line indicates the value of $\rho_{wet\ CO2}$ at which representative values of k_L are chosen for comparison. The transparent block shows the portion of the calculated k_L where noise is apparent, as discussed above.

Figure 3.51 shows the calculated values of k_L from the small $\rho_{wet\ CO2}$ experiments. As discussed in section 3.5.3 'Data Processing Technique', there is noise in the calculated k_L at the end of each experiment. Ignoring this portion of the calculated result and making a comparison at a wet CO_2 density of 0.041 g/cm^3, a number of observations can be made by examining Figure 3.51.

Firstly, the range of k_L values calculated of 0.015 cm/s to 0.056 cm/s are in reasonable agreement with the experimental results for CO_2 dissolution into an aqueous

phase available in the literature. Maalej *et al*. (2003) reported k_L values of 0.014 cm/s to 0.048 cm/s, Niranjan *et al*. (1988) included their results of 0.015 cm/s to 0.060 cm/s, Vazquez (1995) found k_L to vary between 0.0108 cm/s to 0.0123 cm/s, Calderbank and Moo-Young (1961) published values of 0.007 cm/s to 0.008 cm/s and Robinson and Wilke (1974) reported 0.0137 cm/s to 0.0228 cm/s. A comprehensive discussion of the prior experiments is included in section 2.1.3.3 'Experimental Measurement of Mass Transfer Coefficient'.

Secondly, the values of k_L for Experiments 9 to 12, conducted at 363 K, are larger than those of Experiments 1 to 4, which were conducted at 308 K. The prediction of the empirical Wilke and Chang (1955) equation, included as Equation 2.2, is a greater D for a greater T. Experimental evidence has since shown k_L to be proportional to a power, n, of D. The value of n has been found experimentally to vary from near 0 to 0.9, according to Treybal (1980). Thus a larger k_L for a larger T is in agreement with the literature.

Thirdly, the experiments with S_{NaCl} of 4.0 m produce a smaller k_L, than those with 0.6 m S_{NaCl}, all other factors being equal. k_L from Experiment 3 is smaller than the value from Experiment 1, the value from Experiment 4 is smaller than for Experiment 2 and so forth.

Finally, the k_L from experiments with S_{CaCl2} of 0.2 m are close to those with S_{CaCl2} of zero. There is some indication that with a non-zero S_{CaCl2} there is a smaller value of k_L, for example the value from Experiment 2 is smaller than that of Experiment 1. However, this difference must be put in context of the experiment-to-experiment variability

discussed in the next section 3.5.4.2 'Medium Wet CO_2 Density Results; Center Point Repeats'.

3.5.4.2 Medium Wet CO_2 Density Results; Center Point Repeats

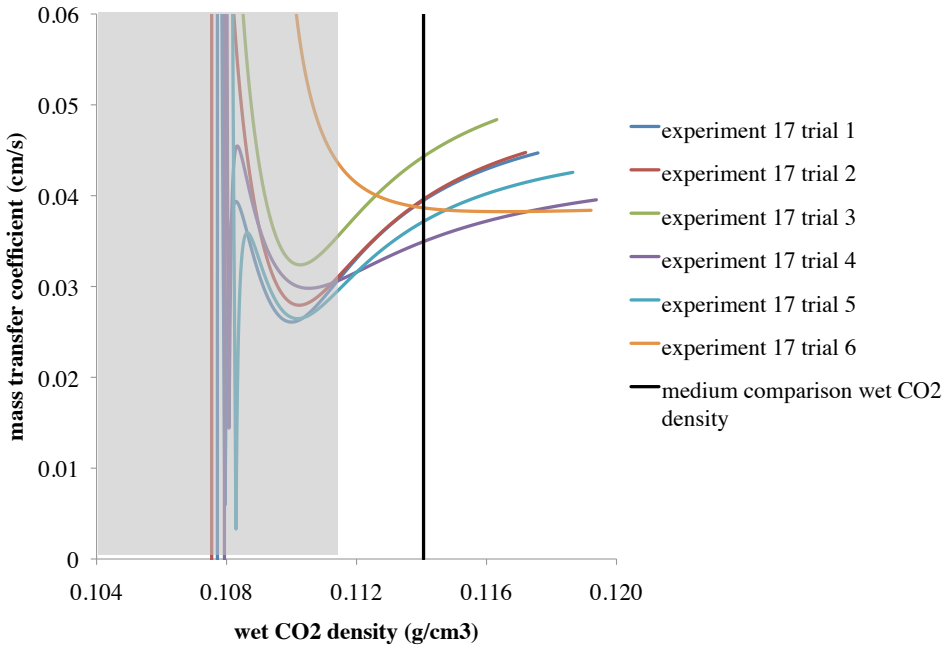

Figure 3.52: k_L versus $\rho_{wet\ CO2}$ for medium $\rho_{wet\ CO2}$ experiments. The vertical line indicates the value of $\rho_{wet\ CO2}$ at which representative values of k_L are chosen for comparison. The transparent block shows the portion of the calculated k_L where noise is apparent, as discussed above.

Calculated values of k_L for the experiments performed at an intermediate value of $\rho_{wet\ CO2}$ are shown in Figure 3.52. A comparison at a $\rho_{wet\ CO2}$ of 0.114 g/cm^3 demonstrates a range of k_L from 0.035 cm/s to 0.044 cm/s. Recall that these are results for a repeats of an experiment at the same conditions each time and therefore provide a measure of the

experiment-to-experiment variability. Again the values of k_L calculated are in reasonable agreement with the values available in the literature.

T = 336 K, S_{NaCl} = 2.3 m and S_{CaCl2} = 0.1 m for these experiments. One trend observed from examination of the results of small $\rho_{wet\ CO2}$ experiments, presented in Figure 3.51, is that greater T leads to a greater k_L. A second trend apparent from the same results is that greater S_{NaCl} leads to a smaller k_L. If it is first assumed that there is no trend in k_L due to $\rho_{wet\ CO2}$, it would be expected that experiments at an intermediate T and S_{NaCl} would produce an intermediate k_L. This expectation is confirmed by the results of the experiments shown in Figure 3.52.

The range of k_L observed from repeats of the same experiment is 0.009 cm/s. The largest difference in k_L observed between small $\rho_{wet\ CO2}$ experiments with S_{CaCl2} = 0.0 m and those with S_{CaCl2} = 0.2 m was 0.007 cm/s. Since the experiment-to-experiment variability is greater than the effect of S_{CaCl2}, it is unlikely that there is a significant trend in k_L with S_{CaCl2} for the small $\rho_{wet\ CO2}$ experiments.

3.5.4.3 Large Wet CO_2 Density Results

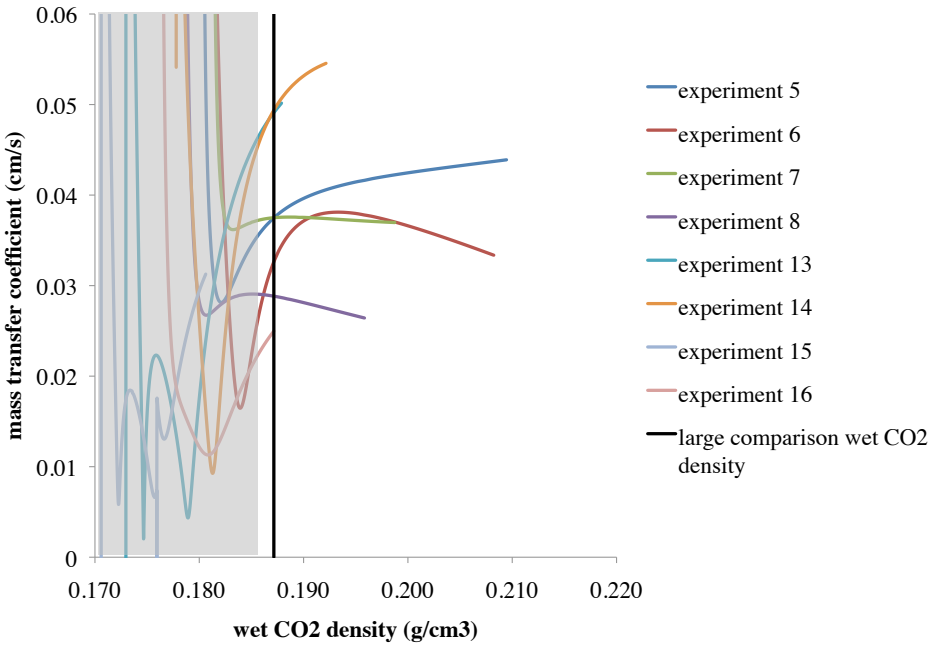

Figure 3.53: k_L versus $\rho_{wet\ CO2}$ for large $\rho_{wet\ CO2}$ experiments. The vertical line indicates the value of $\rho_{wet\ CO2}$ at which representative values of k_L are chosen for comparison. The transparent block shows the portion of the calculated k_L where noise is apparent, as discussed above.

Figure 3.53 shows the calculated values of k_L from the large $\rho_{wet\ CO2}$ experiments. Making a comparison at a wet CO_2 density of 0.187 g/cm^3, a number of observations can be made.

Firstly, again the k_L values calculated are in reasonable agreement with the literature.

Secondly, when comparing the results of experiments at large $\rho_{wet\ CO2}$ to those at small $\rho_{wet\ CO2}$, in three of the eight cases there is an increase in the k_L value calculated from the larger wet CO_2 density experiments. This is the case comparing Experiments 5 and 1, Experiments 7 and 3, and Experiments 8 and 4. However, when comparing Experiments 16 and 12 there is a decrease in k_L for a larger $\rho_{wet\ CO2}$, i.e. the opposite trend is observed. For a comparison between each of the remaining four experiments the difference is less than the experiment-to-experiment variability. It is apparent that there is an interaction effect between the trend in k_L due to $\rho_{wet\ CO2}$ and the trend due to T.

Thirdly, the values of k_L for Experiments 13 and 14, conducted at 363 K, are larger than those of Experiments 5 to 8. However, the values of k_L for Experiments 15 and 16, conducted at 363 K, are smaller than those of Experiments 5 to 8. This may be an indication of an interaction effect between the trend in k_L due to T and the trend due to S_{NaCl}.

Fourthly, the effect of S_{NaCl} on k_L values at large $\rho_{wet\ CO2}$ are varied. There is a very large reduction in k_L comparing the S_{NaCl} = 4.0 m experiments to S_{NaCl} = 0.6 m experiments at 363 K. However, for experiments at 308 K there is a reduction in k_L between Experiments 6 and 8, though not between Experiments 5 and 7.

Finally, as discussed in section 3.5.4.2 'Medium Wet CO_2 Density Results; Center Point Repeats', the range of k_L observed from repeats of the same experiment is 0.009 cm/s. The largest difference in k_L observed between large $\rho_{wet\ CO2}$ experiments with S_{CaCl2} = 0.0 m and those with S_{CaCl2} = 0.2 m was 0.009 cm/s. Since the experiment-to-experiment variability is greater or equal to the effect of S_{CaCl2}, it is unlikely that there is a

significant trend in k_L with S_{CaCl2} for the large $\rho_{wet\ CO2}$ experiments, the same conclusion drawn from the small $\rho_{wet\ CO2}$ experiments.

The point values of k_L for each experiment are tabulated in Table 3.4.

Experiment	T (K)	$\rho_{wet\ CO2}$ (g/cm^3)	S_{NaCl} (m)	S_{CaCl2} (m)	k_L (cm/s)
1	308	0.041	0.6	0.0	0.028
2	308	0.041	0.6	0.2	0.024
3	308	0.041	4.0	0.0	0.015
4	308	0.041	4.0	0.2	0.015
5	308	0.187	0.6	0.0	0.038
6	308	0.187	0.6	0.2	0.033
7	308	0.187	4.0	0.0	0.037
8	308	0.187	4.0	0.2	0.029
9	363	0.041	0.6	0.0	0.050
10	363	0.041	0.6	0.2	0.056
11	363	0.041	4.0	0.0	0.037
12	363	0.041	4.0	0.2	0.038
13	363	0.187	0.6	0.0	0.049
14	363	0.187	0.6	0.2	0.049
15	363	0.181*	4.0	0.0	0.031
16	363	0.187	4.0	0.2	0.025
17, trial 1 to 6	336	0.114	2.3	0.1	0.040, 0.040, 0.044, 0.035, 0.037, 0.039

Table 3.4: Designed experiment results

The * in Table 3.4 denotes the $\rho_{wet\ CO2}$ at which a representative value of k_L was selected for Experiment 15. Experiment 15 data were taken from an early trial, which

commenced at a smaller P^o than required to provide information at $\rho_{wet\ CO2} = 0.187$ g/cm^3, leaving k_L at the largest $\rho_{wet\ CO2} = 0.181$ g/cm^3, which is approximately 3% smaller.

An alternative approach to selecting representative values of k_L from the calculations for each experiment was investigated. Rather than making a comparison of of k_L values at small, medium and large values of $\rho_{wet\ CO2}$, a comparison was made at the point where 50% of the final equilibrium number of moles of CO_2 transported to the aqueous phase had occurred. This selection approach produced k_L values within 13% of those from the approach described above, in all cases except for Experiment 15 and Experiment 16. In those two cases the difference was 46% and 54% respectively. The comparisons at small, medium and large values of $\rho_{wet\ CO2}$ produced larger values k_L for the two experiments, which are representative of earlier time during each experiment and therefore greater CO_2 concentration difference, the driving force for mass transfer. These values are more relevant to modeling the process since a greater mass transfer rate occurs for a greater CO_2 concentration difference. The k_L values selected using this alternative approach are presented in Appendix G.

3.5.5 Forward Model

The k_L values presented in section 3.5.4 'Discussion of Results' are single values computed over the duration of each experiment at intervals of ten seconds. To allow comparison between experiments, a single value of $\rho_{wet\ CO2}$ was then selected for each group of experiments, see Table 3.4 and vertical lines in Figures 3.51, 3.52 and 3.53. To examine the accuracy of assigning a single value of k_L to each experiment, a model using

a single fixed value of k_L was developed to allow comparison to the dynamic (time-varying) k_L.

Several simplifying assumptions were made. The first was that the phase volumes do not change throughout the experiment. That is, there was no brine swelling as shown in Figure 3.48 for Experiment 1. This example demonstrated that the effect was fairly small, in fact only a 1.3 % change over the course of the experiment. Further, the vapor phase was assumed to be pure CO_2. As previously discussed, the vapor pressure of H_2O is small at small T. At the larger T of the designed experiment, 336 K for the center point repeats and 363 K for the large T, there is more error introduced by this assumption, though y_{H2O} is still very small compared to y_{CO2}. The initial V for the CO_2 phase was calculated using the PR EOS. The value of V as the experiment progressed was calculated from the remaining number of moles of CO_2 in the constant volume phase. From the subsequent V, P was calculated at successive time steps using the PR EOS. Using a single tuned PR EOS flash calculation at the initial conditions, Henry's law was then used to calculate the CO_2 solubility at subsequent values of P. Finally, the accumulated moles of CO_2 in the aqueous phase formed the second part of the driving force for mass transfer, the concentration difference. A numerical approach was used to calculate the dissolved concentration history from the mass transfer model. This was then compared to the dynamic calculation of k_L which invokes none of the simplifying assumptions described above. Figure 3.54 shows a comparison of the dissolved CO_2 concentration calculated by each model for Experiment 1.

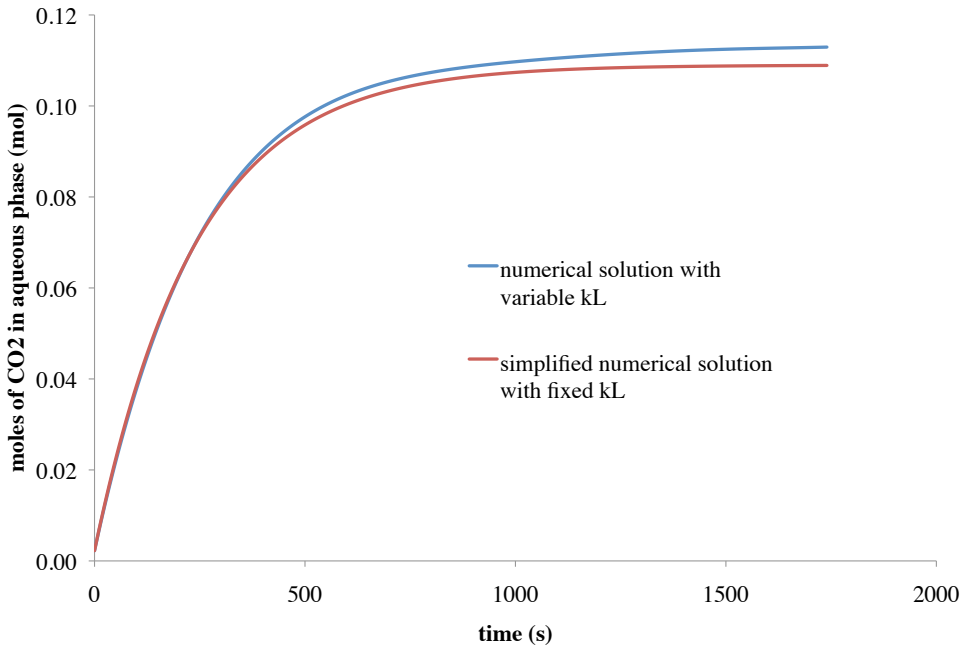

Figure 3.54: Dissolved CO_2 concentration versus time for Experiment 1, calculated by both the dynamic k_L and fixed k_L (forward model) approaches

Figure 3.54 demonstrates that a good fit to the CO_2 concentration history from the dynamic (time-varying) k_L model was achieved with the forward model for Experiment 1. The maximum and minimum percentage errors were 2.9 and -3.6% respectively. The forward model results for each of the twenty-two experiments are presented in Table 3.5.

Experiment	Maximum percentage error (%)	Minimum percentage error (%)
1	2.9	-3.6
2	9.3	-3.6
3	0.0	-6.0
4	0.0	-3.0
5	0.0	-6.0
6	0.0	-6.0
7	3.3	-4.5
8	10.5	-5.6
9	5.1	0.0
10	5.4	0.0
11	7.8	-1.0
12	7.0	-1.0
13	19.6	-3.9
14	8.3	-3.9
15	33.0	-3.2
16	23.3	-3.8
17 trial 1 to 6	3.0, 3.0, 2.7, 0.3, 1.6, 1.2	-2.8, -3.2, -2.8, -3.2, -3.0, -3.7

Table 3.5: Percentage difference in moles of CO_2 in aqueous phase calculated by dynamic k_L and fixed k_L (forward model) approaches

Table 3.5 shows that the percentage difference in moles of CO_2 dissolved into the aqueous phase could be matched to within 10.5 and –6.0% using a single fixed value of

k_L for each experiment, for all but three of the experiments. The remaining three could be matched to within 33.0 and –3.9% using a single fixed value of k_L.

3.5.6 Conclusions

The forward model results demonstrated that a single representative value k_L could be selected for each experiment. The trends in k_L produced by different values of $\rho_{wet\ CO2}$, T, S_{NaCl} and S_{CaCl2} were examined in section 3.5.4 'Discussion of Results'. The difference between any two experiments, one with S_{CaCl2} = 0.0 m and the other with S_{CaCl2} = 0.2 m, all other independent variables being equal, was equal to or smaller than the experiment-to-experiment variation. As a result the sixteen experiments were reduced to eight experiments for further discussion. The k_L values for the eight experiments are shown in Table 3.6.

Experiment	T (K)	$\rho_{wet\ CO2}$ (g/cm^3)	S_{NaCl} (m)	S_{CaCl2} (m)	k_L (cm/s)
1	308	0.041	0.6	0.0	0.028
3	308	0.041	4.0	0.0	0.015
5	308	0.187	0.6	0.0	0.038
7	308	0.187	4.0	0.0	0.037
9	363	0.041	0.6	0.0	0.050
11	363	0.041	4.0	0.0	0.037
13	363	0.187	0.6	0.0	0.049
15	363	0.181*	4.0	0.0	0.031

Table 3.6: Designed experiment results

When examining the k_L values for the remaining eight experiments, a greater S_{NaCl} results in a smaller value of k_L in all four comparisons made between otherwise identical experiments. In one comparison, that of Experiments 5 and 7, the difference in k_L is within the experiment-to-experiment variation. Nonetheless the trend is uniform.

A larger T results in a greater value of k_L in three of the four comparisons made between otherwise identical experiments. For the one comparison where the trend is reversed, Experiments 7 and 15, the difference in k_L is within the experiment-to-experiment variation.

A larger $\rho_{wet\ CO2}$ results in a greater value of k_L in two of the four comparisons made between otherwise identical experiments. For the two remaining comparisons where the trend is reversed, comparison of Experiments 9 to 13 and Experiments 11 to 15, the difference in k_L is within the experiment-to-experiment variation. The trends discussed are illustrated by Figure 3.55.

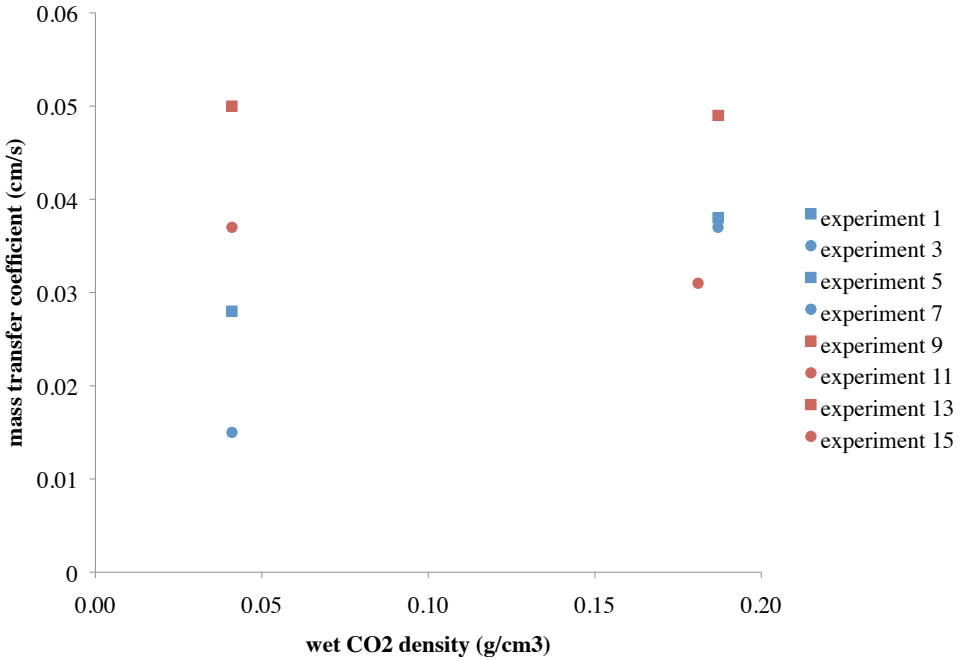

Figure 3.55: k_L versus $\rho_{wet\ CO2}$ for the eight experiments

Figure 3.55 shows T = 308 K experiments in blue and T = 363 K experiments in red. S_{NaCl} = 0.6 m experiments are represented by squares and S_{NaCl} = 4.0 m experiments are indicated by circles.

3.5.6 Statistical Analysis

3.5.6.1 Analysis of Variance

Using the representative k_L values included in Table 3.4, an analysis of variance (ANOVA) procedure was completed. This was undertaken to determine the statistical significance, or otherwise, of the effect of $\rho_{wet\ CO2}$, T, S_{NaCl} and S_{CaCl2} on k_L. The first step in the ANOVA was to determine the sum of squares error (SSE) using the center point

repeats (Experiment 17 trials 1 to 6). The SSE was calculated to be 0.0000494. The second step in the ANOVA was to calculate the mean square (MS) for the independent variables $\rho_{wet\ CO2}$, T, S_{NaCl}, S_{CaCl2}, and interactions between them. Two-way, three-way and the four-way interactions were considered. The third step was to calculate the p-value for each independent variable and interaction term. The MS and p-value for each are presented in Table 3.7.

Variable	Mean square	p-value
T	0.0008677	0.00857
$\rho_{wet\ CO2}$	0.0000516	0.35356
S_{NaCl}	0.0006019	0.01748
S_{CaCl2}	0.0000160	0.59377
$T*\rho_{wet\ CO2}$	0.0004220	0.03293
$T*S_{NaCl}$	0.0001336	0.16105
$T*S_{CaCl2}$	0.0000225	0.52977
$\rho_{wet\ CO2}*S_{NaCl}$	0.0000025	0.83182
$\rho_{wet\ CO2}*S_{CaCl2}$	0.0000350	0.43850
$S_{NaCl}*S_{CaCl2}$	0.0000072	0.71913
$T*\rho_{wet\ CO2}*S_{NaCl}$	0.0000549	0.34005
$T*\rho_{wet\ CO2}*S_{CaCl2}$	0.0000012	0.88445
$T*S_{NaCl}*S_{CaCl2}$	0.0000103	0.66689
$\rho_{wet\ CO2}*S_{NaCl}*S_{CaCl2}$	0.0000057	0.74806
$T*\rho_{wet\ CO2}*S_{NaCl2}*S_{CaCl2}$	0.0000037	0.79420

Table 3.7: MS and p-value for each independent variable and interaction term

Using significance level of 0.05, the p-values indicate that only T, S_{NaCl} and $T^*\rho_{wet\ CO2}$ are statistically significant.

3.5.6.2 Empirical Correlation

Based on the three variables determined to be statistically significant, a linear empirical correlation was developed and is given by Equation 3.10.

$$k_L = 0.00027(T - 336.15) - 0.00256(T - 336.15)\left(\rho_{wetCO_2} - 0.114\right) - 0.00361 S_{NaCl} + 0.04288$$

Equation 3.10

Equation 3.10 demonstrates a positive correlation between k_L and T. The interaction term $T^*\rho_{wet\ CO2}$ produces an increase in k_L for an increase in $\rho_{wet\ CO2}$ when T is less than 336.15 K and a decrease in k_L for an increase in $\rho_{wet\ CO2}$ when T is greater than 336.15 K. Finally, there is a negative correlation between k_L and S_{NaCl}.

3.5.7 Region of Applicability

The empirical correlation presented above was developed from data measured over the ranges presented in Table 3.8.

Parameter	Small value	Large value
T (K)	308	363
$\rho_{wet\ CO2}$ (g/cm^3)	0.041	0.187
S_{NaCl} (m)	0.6	4.0

Table 3.8: Parameter ranges

Caution would be advised in using the correlation outside of the parameter ranges presented in Table 3.8. For practical purposes, operating P is more likely to be used for process design than $\rho_{wet\ CO2}$. The conversion between the range of $\rho_{wet\ CO2}$ used and range of P is presented in Figure 3.56.

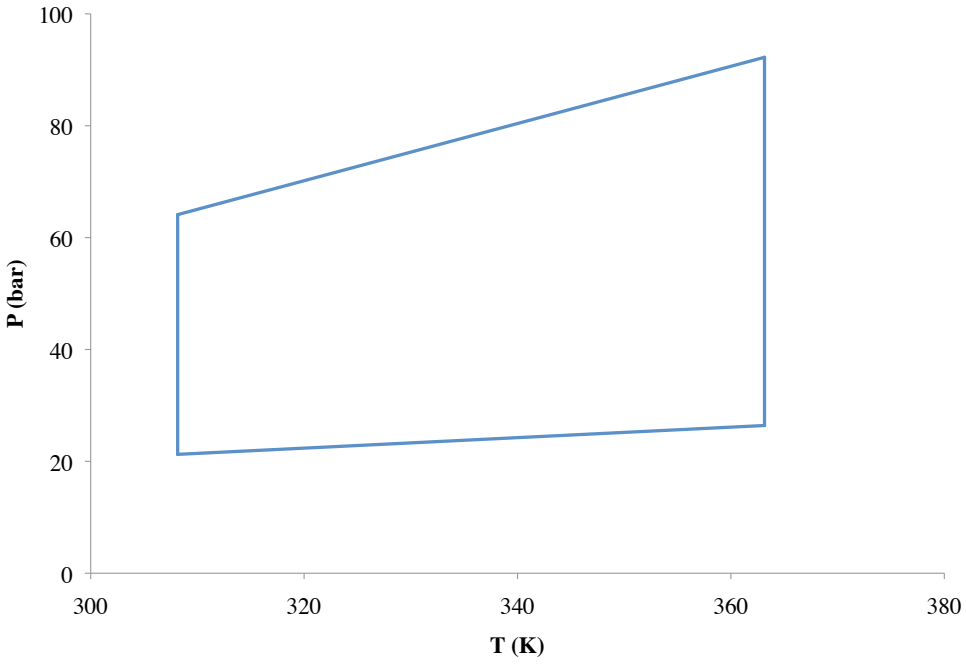

Figure 3.56: Applicable P, T space for Equation 3.10

Chapter 4: Application to Geologic CO_2 Storage

The kinetics data for CO_2 dissolution into brine obtained from the designed experiment was applied to a number of different mass transport scenarios. The first example studied is co-injection of CO_2 with brine at the wellhead. This CO_2 sequestration approach may be considered a hybrid between conventional and surface dissolution approaches. The second and third configurations are both true surface dissolution approaches, where CO_2 is completely dissolved into brine on the surface prior to injection at the wellhead. The second system utilizes CO_2 and brine co-injection in a horizontal pipe, whereas the third uses a mixing tank. There are advantages and disadvantages to each approach.

4.1 Co-Injection at the Wellhead

4.1.1 Background on Surface Dissolution Approach

Previous research on the surface dissolution approach to CO_2 sequestration by Burton (2008) and Jain (2011) assumed a mixing tank on the surface. An alternative to this process is to use the tubing string in individual injection wells as in-line mixers, thereby eliminating the capital and possible operating costs of a mixing tank. With such a concept, native brine would still be lifted from an aquifer via extraction wells, though CO_2 would be co-injected at the wellheads of injection wells rather than into a separate surface facility prior to injection. A schematic of this approach is shown in Figure 4.1.

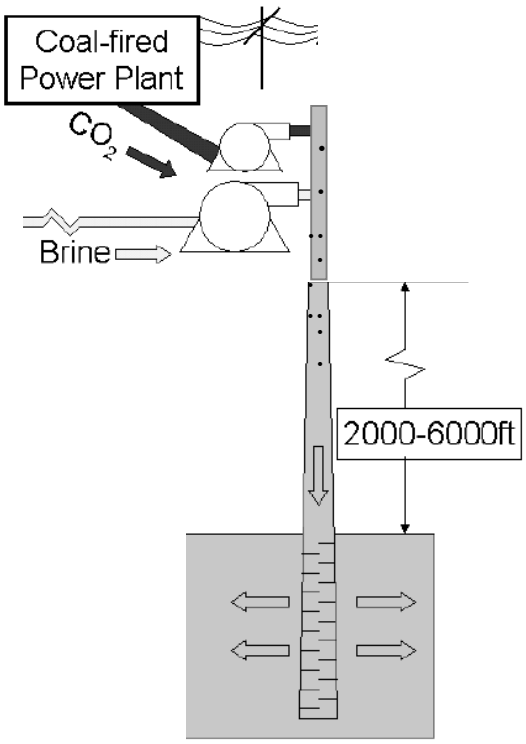

Figure 4.1: Schematic of the co-injection approach. The bulk CO_2 phase enters the brine stream as bubbles, which dissolve as they travel down the wellbore.

Burton (2008) provided an estimate of the capital costs of a surface dissolution approach of $750 to $900 thousand per MW of capacity. Assuming the large end of this range estimate, the surface dissolution infrastructure for a typical 500 MW power station would cost $450 million. The cost breakdown itemized the mixing tank cost of $20 to $30 thousand per MW of capacity. Again taking the upper bound of this range for a 500 MW power station, the mixing tank cost is $15 million. This is a small component of the overall capital cost, approximately 3%. However, if it can be demonstrated that the same technical outcome (viz., complete dissolution of CO_2 phase and a target dissolved CO_2 concentration) can be achieved, the co-injection approach would be preferable. The potential disadvantage of this approach is that detecting process upsets may be more

difficult. With the true surface dissolution approach, the CO_2 saturated brine could be easily sampled and concentration measurements performed. Sampling brine from the bottom of each injection well using the hybrid co-injection approach would be difficult.

4.1.2 Rates and Concentrations at Typical Operating Conditions

The core of the surface dissolution approach is injection of CO_2 laden brine with concentration at or below that of the saturation CO_2 concentration at target aquifer conditions. This requirement remains unchanged with this hybrid approach. A simplified transport model is developed below to predict the dissolution of CO_2 bubbles co-injected with brine at the wellhead. The model assumes a target aquifer at a depth of 2000 ft, which was determined by Burton (2008) to be the optimum depth in terms of maximum CO_2 storage per unit volume of pore space. This result was obtained from examining the trend of equilibrium x_{CO2} with depth assuming typical P, T and S_{NaCl} trends. The example brine composition was S_{NaCl} = 0.6 m and S_{CaCl2} = 0.2 m. Assuming a normal pore P gradient of 0.433 psi/ft, the hydrostatic contribution to pore P at 2000 ft is 866 psig, $P_{storage}$ = 60.7 bar. The storage aquifer was assumed to be at T = 308 K, derived from a typical surface T of 60 °F and geothermal gradient of 1.75 °F/100ft. The tuned Peng-Robinson EOS flash calculation yields x_{CO2} = 0.0165 for these conditions. The density model of Li *et al*. (2011) predicts a CO_2 saturated brine density of 1.05 g/cm^3 for the aquifer considered. From these two results, the saturation CO_2 concentration is 8.90×10^{-4} mol/cm^3.

Jain (2011) conducted an economic optimization study for a set of typical reservoir parameters and a CO_2 storage rate of 10 000 ton/d. The results showed that 168

wells, each injecting 7358 b/d, was the lowest cost option. Assuming the brine composition above, the per-well mole rate of H_2O is 740 mol/s, which via the value of x_{CO2} given above, allows the calculation of the per well mole rate of CO_2 of 12.4 mol/s. The calculation of total CO_2 storage rate for the 168 wells is 8 000 ton/day, which is lower than the 10 000 ton/day used by Jain (2011) in the optimization study. The difference between the two values may be due to the value of x_{CO2} used by Jain (2001). Since q is large, heat transfer is assumed to be negligible and the system isothermal at the target aquifer T.

One of the reservoir engineering assumptions made by Jain (2011) was the bottom-hole injection P, $P_{bottomhole}$ (bar), was limited by the fracture pressure for the formation. With an assumed fracture gradient of 1 psi/ft, the fracture P of the 2000 ft well is 2000 psig, 138.9 bar. Thus $P_{bottomhole}$ was assumed to be 138.9 bar. The injection P, $P_{injection}$ (bar) is given by:

$$P_{injection} = P_{bottomhole} - P_{hydrostatic} + P_{friction} \qquad \text{Equation 4.1}$$

with hydrostatic P, $P_{hydrostatic}$ (bar), and frictional P loss, $P_{friction}$ (bar). $P_{hydrostatic}$ = 59.8 bar regardless of wellbore size and $P_{friction}$ = 1.7 bar for a 4 inch wellbore. It is apparent that $P_{friction}$, even a small wellbore of 4 inch diameter, is small compared to $P_{hydrostatic}$. $P_{friction}$ = 0.2 bar for a 6 inch wellbore. Since $P_{friction}$ is small, the same $P_{injection}$ was used for both the 4 inch and 6 inch wellbores. The parameters for the typical application considered are presented in Table 4.1.

Wellbore diameter (inch)	4 and 6
Depth (ft)	2000
S_{NaCl} (m)	0.6
S_{CaCl2} (m)	0.2
T (K)	308
q (b/d)	7358
$P_{storage}$ (bar)	60.7
$P_{injection}$ (bar)	80.8
$P_{bottomhole}$ (bar)	138.9

Table 4.1: Parameters for wellhead co-injection at typical operating conditions

4.1.3 Design Considerations for Hybrid Approach

As discussed in detail in the CO_2 solubility section of Chapter 3, CO_2 solubility increases with increasing P, all other factors being equal. Since both $P_{injection}$ and $P_{bottomhole}$ are greater than $P_{storage}$, it follows that the CO_2 solubility down the entire depth of the well is greater than the desired CO_2 concentration for aquifer storage. This, in turn, leads to the necessity of controlling the CO_2 concentration of brine at the bottom of the well by adjusting the injected CO_2 rate at the wellhead. Stated another way, if the CO_2 rate injected at the wellhead exceeds that which will produce a CO_2 concentration greater than the CO_2 solubility at aquifer conditions, the brine will be over-saturated with CO_2 at aquifer conditions. This would lead to buoyant CO_2 flashing from brine in the aquifer and existing as a bulk phase. If this were to occur, the core purpose of the surface dissolution approach to CO_2 sequestration would not be achieved. Hence the design target for the co-

injection approach is two-fold: i) determine the ratio of CO_2 and brine injection rates at the wellhead which yields the desired concentration of dissolved CO_2, and ii) ensure that the CO_2 is completely dissolved when the fluids reach the bottom of the well.

The concept of a 'stoichiometric CO_2 rate' is convenient. This refers to a CO_2 rate which produces brine with a CO_2 concentration at the saturation solubility for the target aquifer conditions, once complete dissolution has occurred. Using the tuned Peng-Robinson flash calculation, the saturation CO_2 concentration at both $P_{injection}$ and $P_{bottomhole}$ was calculated. Since pressure varies linearly in the wellbore, a linear relationship between saturation concentration and depth is assumed for the purposes of modeling the driving force for mass transfer.

It is important to note that the $P_{injection}$ calculations presented above are for a single brine phase flowing in the wellbore, whereas the actual case is of two-phase flow (bulk CO_2 and brine) for some fraction of the wellbore. The farther down the wellbore the smaller the CO_2 volume as a fraction of the total volume of phases flowing. For a stoichiometric CO_2 rate, no liquid or gas holdup and the conditions assumed above, the maximum (i.e. before any dissolution occurs) bulk phase CO_2 volume is 7.5% of the total volume. Since this is relatively small, the system was simplified to the case of single-phase flow for the purpose of calculating $P_{friction}$ and the P traverse. If a detailed two-phase flow-in-pipe simulation were to be completed, it would indicate a greater $P_{injection}$ was required. This would increase the saturation CO_2 concentration and the driving force for mass transfer. A small volume fraction of CO2 would also reduce the hydrostatic gradient in the wellbore, leading to a larger $P_{injection}$. Consequently, the simplification used in this model is conservative.

The CO_2 phase is less dense than brine and thus will move more slowly down the wellbore than brine due to buoyancy. The simplifying assumption of no liquid or gas holdup is therefore also conservative, since if buoyant CO_2 phase moves upward relative to the brine, it will contact brine with a smaller instantaneous CO_2 concentration and thus transfer mass into the brine more rapidly than if the CO_2 moves at the same speed as the brine.

The expected flow regime for the brine with a 7.5% by volume gas phase was determined using the chart of Govier and Aziz (2008), presented in Figure 4.2, and the superficial velocities of each phase. Based on the assumed flowrate of 7358 b/d, the brine superficial velocity is 5.5 ft/s for a 4 inch wellbore and 2.4 ft/s for a 6 inch wellbore. The CO_2 superficial velocity at the wellhead, where it is greatest, is 0.5 ft/s for a 4 inch wellbore and 0.2 ft/s for a 6 inch wellbore. These superficial velocities indicate that the flow regime is a continuous flow of liquid phase with bubbles of gas phase.

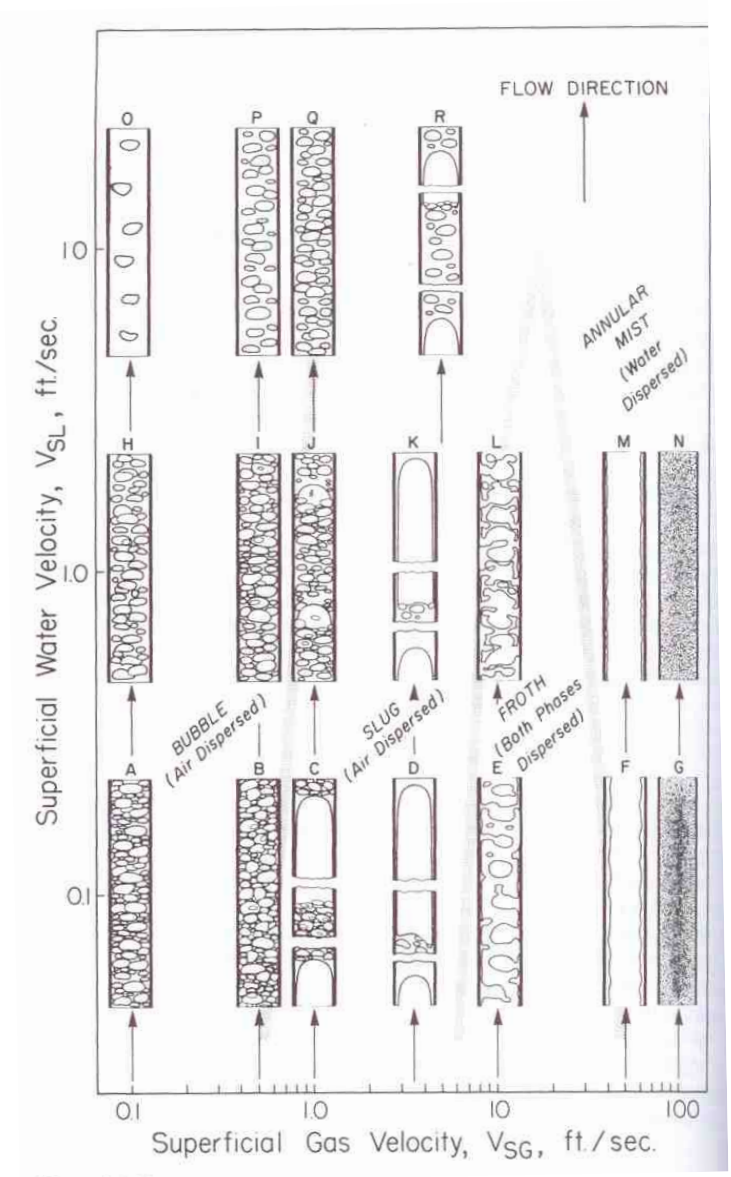

Figure 4.2: Expected two phase flow regimes based on phase superficial velocities from Govier and Aziz (2008)

There is a significant decrease in CO_2 *V* from wellhead injection conditions to bottom-hole conditions, due to the increase in *P* between the two points. For CO_2 at close to the *T* and *P* range considered, the Peng-Robinson prediction of volumetric properties

was shown to be inaccurate by as much as 13%, see Figure 1 for details. Instead the NIST Thermophysical Properties of Fluid Systems (2012) calculator was used to predict the CO_2 *V*. For the *P* range considered at the *T* assumed, the following data was generated:

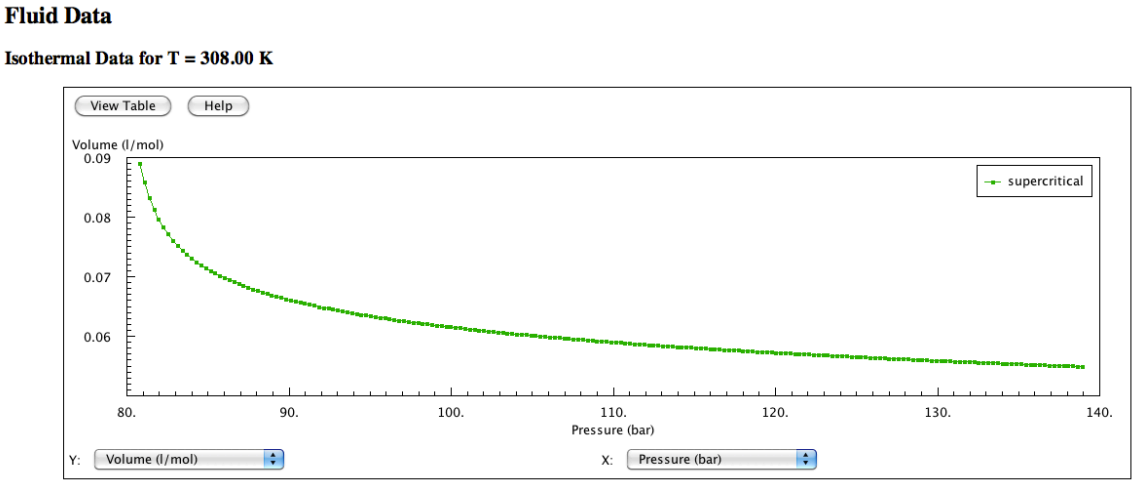

Figure 4.3: CO_2 *V* versus *P* for 308 K from NIST (2012)

Figure 4.3 shows that the supercritical CO_2 *V* varies from 0.089 dm^3/mol to 0.055 dm^3/mol from $P_{injection}$ = 80.8 bar to $P_{bottomhole}$, = 138.9 bar, a 38% reduction. This reduces the volume of supercritical phase CO_2 and therefore the surface area for mass transport available as flow progresses down the wellbore.

4.1.4 Mathematical Model of Mass Transfer During Co-Injection

The numerical model developed discretized the well depth into 10 ft increments. Based on the superficial velocity of brine, a time step was calculated that allowed flow over the 10 ft depth increment. The number of moles of CO_2 required by stoichiometry for the input brine flow rate was calculated and converted to a volume of vapor phase

CO_2 using the CO_2 V from NIST for the prevailing P. It was assumed that this volume of CO_2 was split equally into a constant number of CO_2 bubbles. That is, the bubbles do not run into each other and form larger bubbles or break up to form smaller bubbles. With a number of bubbles specified, the initial bubble size and the CO_2/brine interfacial area a were calculated.

The k_L value calculated from experiment 6, 0.033 cm/s, was applied. Doing so assumes that k_L calculated from an experiment with two bulk phases and a relatively flat interface can be applied to the case of gas bubbles in a continuous liquid phase. The further assumption is made that k_L is independent of bubble size. Calderbank and Moo-Young (1961) found k_L to be independent of bubble size for a particular bubble class, small rigid bubbles or large bubbles, though they measured a smaller k_L for small bubbles and a larger k_L for large bubbles. Since a rigorous approach for determining a small bubble k_L and a large bubble k_L is not available, the simplifying assumption that these are the same has been made.

The parameters used for experiment 6 were T = 308 K, wet CO_2 density = 0.187 g/cm^3, S_{NaCl} = 0.6 m and S_{CaCl2} = 0.2 m. The wet CO_2 density range for the wellhead co-injection application is from 0.494 g/cm^3 to 0.801 g/cm^3, considerably greater than the densities prevailing in experiment 6. The designed experiment was developed for the application of true surface dissolution, which would be conducted at a smaller wet CO_2 density. The experiments were also practically limited by the change in flow regime encountered for wet CO_2 densities above 0.25 g/cm^3. The designed experiment results show an increase in k_L with increasing wet CO_2 density at T less than 336 K and while

using the data for this application is an extrapolation outside the range, it is made as conservatively as possible by not extrapolating the increase in k_L.

With a defined for the particular time increment and k_L obtained from experimental data, the instantaneous and saturation CO_2 concentrations are the only remaining terms required to calculate the CO_2 dissolution rate from Equation 2.4b. The instantaneous CO_2 concentration is initially zero, while the saturation CO_2 concentration was calculated from the linear trend determined above. The molar rate of CO_2 mass transfer for a time step was then calculated. Using a numerical integration with respect to time, the moles of CO_2 transported into the brine phase during the time step was calculated. The balance of moles of CO_2 remaining in the bulk phase was then calculated. This balance was used for the next time step, where a is reduced due to the smaller number of moles of CO_2 and a smaller CO_2 V. The instantaneous CO_2 concentration was then calculated from cumulative CO_2 transferred to the control volume of brine. Thus we ignore axial mixing of the brine phase. The results for 4 inch and 6 inch wellbores are shown in Figure 4.4.

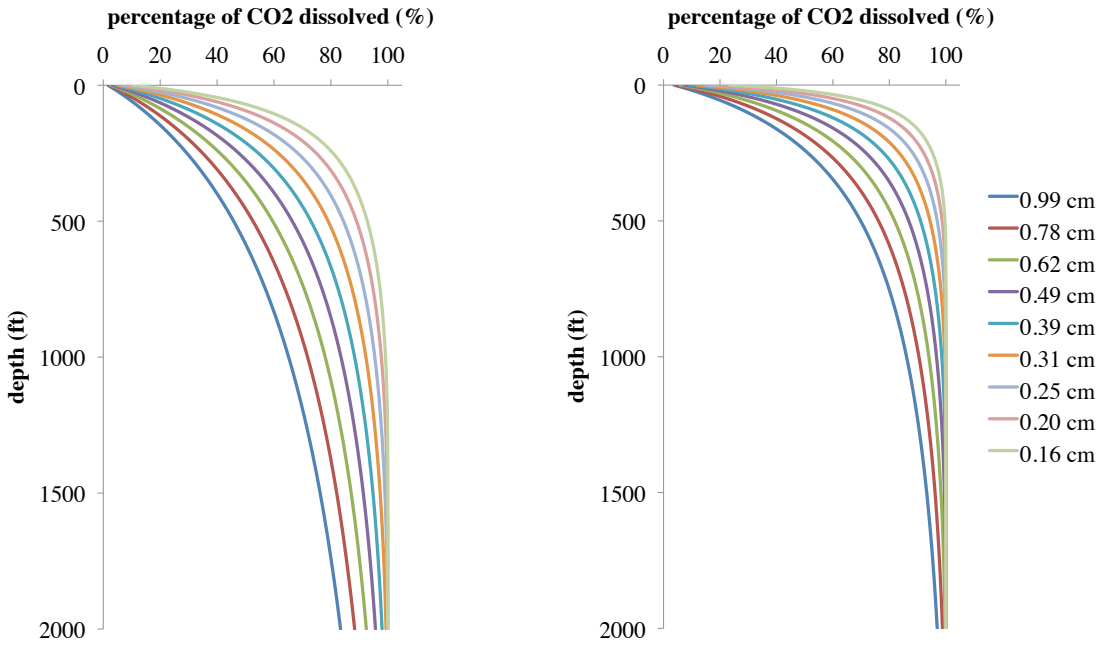

Figure 4.4: Percentage of CO_2 dissolved versus depth for 4 inch wellbore (left) and 6 inch wellbore (right). Operating conditions given in Table 4.1.

Figure 4.4 presents the CO_2 dissolved as a percentage of the stoichiometric quantity injected at the wellhead. Recall that the design aim of this hybrid approach is to completely dissolve the CO_2 injected at the wellhead prior to injection at the bottom of the well. It follows then that for a particular wellbore size and flowrate, a CO_2 bubble size should be selected that achieves complete dissolution at a depth shallower than the bottom of the well. For the 4 inch wellbore, this occurs for only two of the bubbles sizes, 0.20 cm and 0.16 cm, for which the depths for complete dissolution are 1830 ft and 1480 ft, respectively. The depths at which complete CO_2 dissolution is achieved for the 6 inch wellbore are shallower than for the 4 inch wellbore due to the slower flow velocities in a larger well for the same flowrate. For the 6 inch wellbore a bubble size of 0.31 cm

produces complete dissolution at 1330 ft, with smaller bubbles dissolving completely at progressively shallower depths. The depths at which complete dissolution is achieved for a 6 inch wellbore are shown in Figure 4.5.

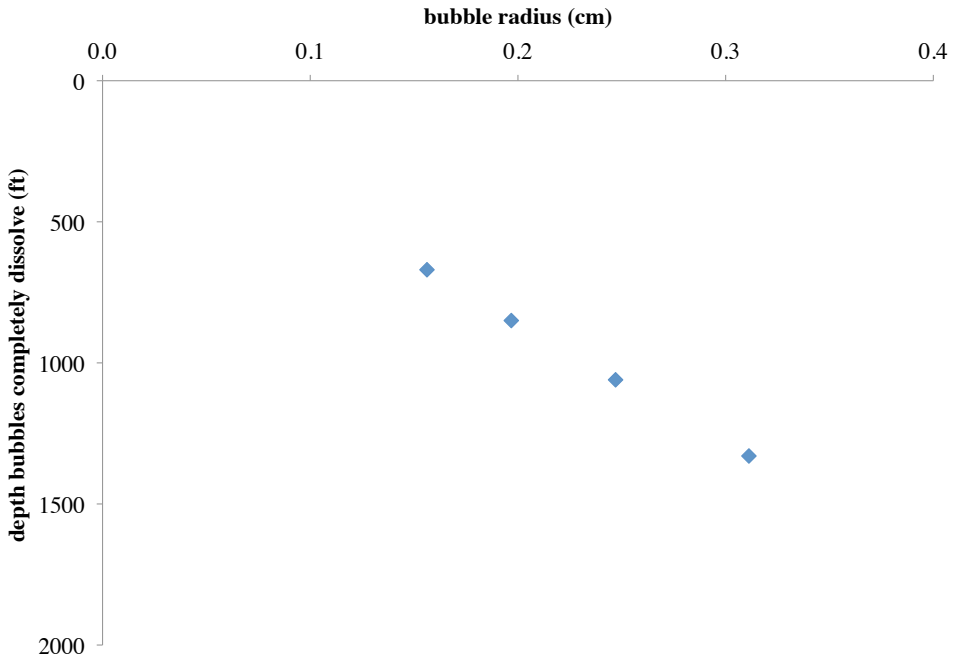

Figure 4.5: Depths at which bubbles completely dissolve for a 6 inch wellbore for operating conditions given in Table 4.1.

The trend of complete dissolution depth versus bubble radius is linear. The surface area of a spherical bubble is proportional to its radius squared. If the radius is doubled the surface area, and hence the rate of mass transfer between CO_2 phase and aqueous phase, increases by a factor of four. The volume of a spherical bubble is proportional to radius cubed. If the radius is doubled the volume increases by a factor of eight. Since the calculation is for a fixed rate of CO_2 injection, the total initial volume of bulk phase CO_2 is the same regardless of bubble size. Thus for bubbles of double the

radius, the number of bubbles is reduced by a factor of eight. So while the surface area of each is increased by a factor of four, there are only one eighth the number of bubbles available. Thus for a doubling of bubble radius there is a halving of available total surface area and consequently a halving of the overall rate of mass transfer. This, in turn, leads to the linear relationship of greater depth for complete dissolution of larger bubbles observed in Figure 4.5.

It should be noted that in any application a range of bubble sizes would be produced, rather than all being of equal size. It follows that the results above could be used as a guide to the maximum bubble size allowable to achieve complete dissolution for a particular depth.

4.2 Co-Injection in a Horizontal Pipe

One possible approach to true surface dissolution is co-injection in a horizontal pipe on surface. The horizontal pipe would serve as the in-line equivalent to the mixing tank and contribute to the capital cost of the project, though such an approach offers the advantage of process control at the surface and easy sampling of CO_2 saturated brine sampling for concentration measurement.

The transport model used for co-injection in a horizontal pipe is very similar to that used for co-injection in a wellbore. Calculations were made on the basis of the product of the example 7358 b/d per well brine flowrate and 168 wells determined by Jain (2011) as an economic optimum for typical reservoir properties. The total flowrate was 1 236 144 b/d. The brine superficial velocity was calculated to be 6.4 ft/s for a 48

inch diameter pipe. It was again assumed that the system would be isothermal at the aquifer storage *T*. However, in this case the possibility of injecting a greater than stoichiometric rate of CO_2 was considered, since this would allow for a greater *a* and therefore shorter length of pipe to reach saturation CO_2 concentration. CO_2 that does not dissolve at the end of the horizontal in-line mixer is easily recycled. To limit the concentration of CO_2 for this configuration, the operating *P* of the horizontal pipe $P_{operating}$ (bar) would be at $P_{storage}$. The *P* of the CO_2 laden brine from the end of the horizontal pipe would then be increased to $P_{injection}$ on a single or multi-well basis, allowing control of each injection well as required. The *P* drop across a 2000 ft long and 48 inch diameter pipe was calculated to be 0.2 bar and neglected. With $P_{operating}$ constant, the CO_2 *V* is constant along the pipe and equal to 0.26 dm^3/mol, far greater than the 0.089 dm^3/mol to 0.055 dm^3/mol range for the case of wellhead co-injection. Constant $P_{operating}$ also leads to a constant saturation CO_2 concentration along the length of the pipe.

Pipe diameter (inch)	48
Depth (ft)	2000
S_{NaCl} (m)	0.6
S_{CaCl2} (m)	0.2
T (K)	308
q (b/d)	1 236 144
$P_{storage}$ (bar)	60.7
$P_{operating}$ (bar)	60.7

Table 4.2: Parameters for horizontal pipe co-injection at typical operating conditions

The greater CO_2 *V* leads to a superficial velocity of 1.6 ft/s. Consultation of the chart prepared by Govier and Aziz (2008), Figure 50, shows that this places the flow regime into the slug flow region. This is undesirable from the standpoint of discrete bubbles with a known *a*. To produce flow in the bubble region, the CO_2 superficial velocity was restricted to 1 ft/s. This, in turn, reduces the CO_2 rate to 65% of stoichiometric. The results of this calculation for different bubble sizes is shown in Figure 4.6.

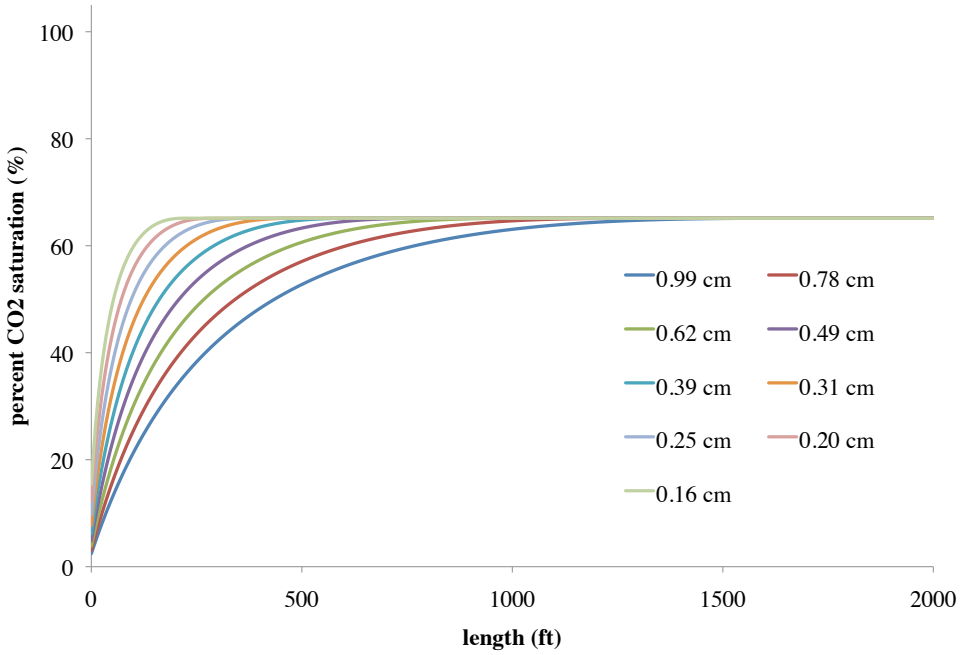

Figure 4.6: Percentage of CO_2 saturation versus axial position for a 48 inch horizontal pipe for operating conditions given in Table 4.2

Figure 4.6 shows that there is an axial position in the pipe for each bubble size beyond which there is no further increase in percent CO_2 saturation. This is the point where the bubbles have completely dissolved. Figure 4.7 shows the length along the

horizontal pipe where complete dissolution of the CO_2 bubbles occurs for each bubble size.

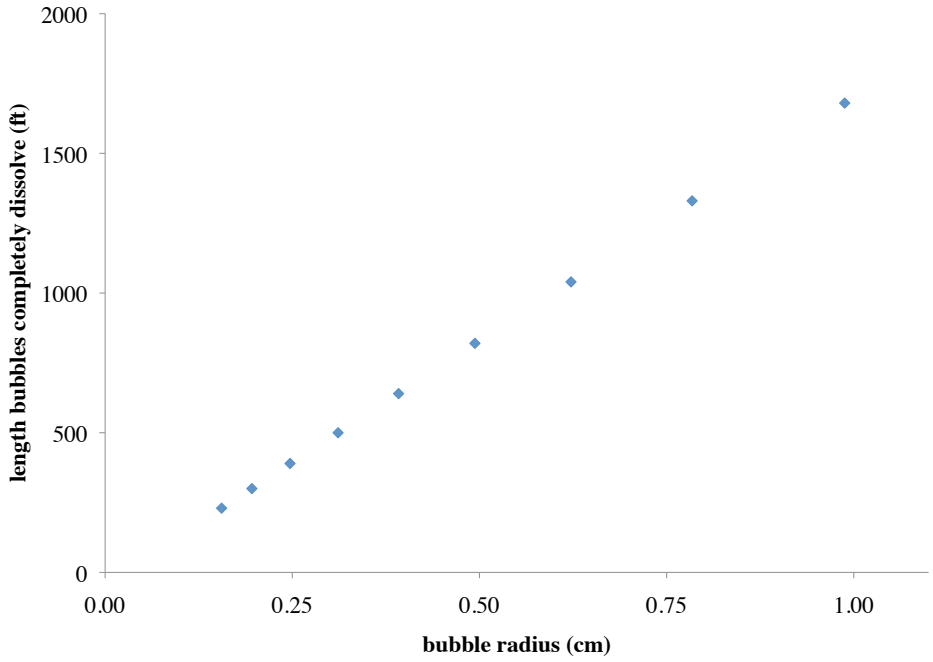

Figure 4.7: Axial position along horizontal pipe where complete bubble dissolution occurs

The same linear trend between distance travelled to complete bubble dissolution and bubble radius presented in Figure 4.5 for a 6 inch wellbore is demonstrated in Figure 4.7 for a horizontal pipe. The same logic of available total surface area applies, that is a doubling of bubble radius leads to a halving of available total surface area for a given flow rate of bulk phase CO_2.

With a surface horizontal pipe, it is feasible to have multiple CO_2 feeds, which would allow close to complete saturation even at an operating *P* equal to that of the target aquifer. This approach also allows the possibility of a catching tank or 'separator' prior to injection of the CO_2 saturated brine at wellheads. The separator would not be run in the typical oilfield application by operating at a *P* significantly lower than the incoming stream. Rather it would be operated at close to the same pressure as the horizontal mixing pipe and be designed to allow sufficient residence time for any un-dissolved CO_2 bubbles to rise out of the brine and be re-circulated through the dissolution system, enabling greater process control.

4.3 MIXING TANK

Another possible approach to true surface dissolution is a mixing tank. A mixing tank allows sampling of CO_2 saturated brine for concentration measurement and would provide a high level of process control, at the cost of the infrastructure required. The most basic calculation of the volume required for such a tank was made on the basis of a residence time.

For the *P*, *T* and brine composition considered in the co-injection applications, the forward model, detailed in section 3.55 'Forward Model', was run for an ideal case where there are initially two pure phases. In contrast the isothermal data analyzed from the designed experiment always starts with two partially mixed phases since the earliest time data was affected by departure from isothermal conditions and some mass transfer takes place during displacement of brine from the vessel. The results of the forward model are shown in Figure 4.8.

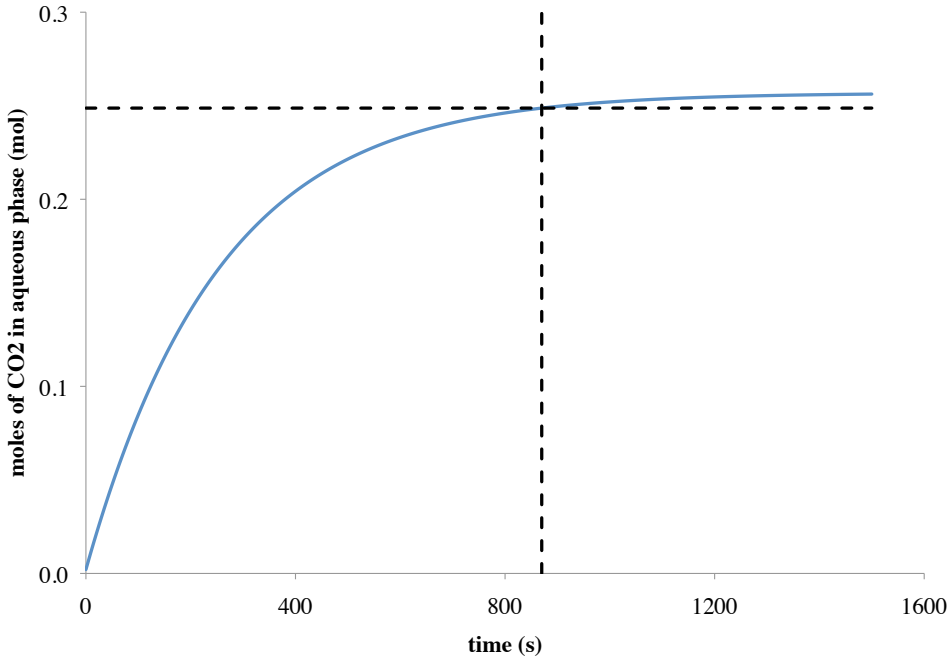

Figure 4.8: Forward model results for an ideal Experiment 6

The forward model results show that the time to 90% of CO_2 saturation is 870 seconds. Assuming an increase in *a* of 100 times due to gas entrainment, the 90% saturation time, which was used as a residence time, is 8.7 seconds. Using the example brine flowrate of 1 236 144 b/d from Table 4.2, the mixing tank volume required is 124 b. It should be stressed that this is an estimate rather than a detailed engineering approach to the problem. It assumes that the same specific surface area can be created in a 124 b tank as in a 600 cm^3 laboratory pressure reactor, which may not be realistic.

Chapter 5: Conclusions and Future Work

The surface dissolution approach is a feasible alternative to standard geologic CO_2 sequestration. This thesis has explored the kinetics of CO_2 dissolution into brine, which is a critical aspect of the process and one for which data were not previously available in the literature.

An empirical correlation was developed for k_L as a function of T, $\rho_{wet\ CO2}$ and S_{NaCl}. This correlation was positive for T and negative for S_{NaCl}. There was found to be an interaction between T and $\rho_{wet\ CO2}$ that produced a varied effect on k_L, depending on the value of each. The $CaCl_2$ concentration tested, which was selected to be representative of formation brines, produced no statistically significant change in k_L compared to experiments with no $CaCl_2$. It was shown that gas entrainment can produce a considerable increase in interfacial area, which is desirable to decrease time to equilibrium.

An experimentally determined value of k_L was applied to a typical application using several basic mass transfer models for different process configurations. It was demonstrated that the hybrid surface dissolution approach of wellhead co-injection of CO_2 and brine can be used to produce complete dissolution of bulk phase CO_2 before fluid enters the storage structure as a single phase. It was also shown that a horizontal flow line or mixing tank could be used.

The apparatus and procedure developed to conduct the batch experiments may be used for other kinetics applications. One such application is the simultaneous dissolution

of CO_2 into and production of dissolved CH_4 from brine. Another application is dissolution of flue gas into brine, in place of pure CO_2. This could potentially replace the energy intensive CO_2 capture process employed by many, if not all, sequestration applications. To understand the in detail the two phase flow regime of CO_2 and brine at the operating conditions of interest, co-injection experiments may be done in vertical or horizontal pipes.

The transport calculations may be refined. Accurate two-phase flow correlations could be used, along with statistical models for bubble size distributions. An optimization study could be conducted to select the best process configuration.

5.1 Results of Experiments

5.1.1 Investigative Experiment Results

The investigative experiments conducted allowed selection of a mechanical configuration and experimental parameters that produced a well-mixed aqueous phase with quantifiable a. These two conditions are critical in conducting experiments from which an accurate calculation of k_L can be made.

An aqueous phase volume half of the vessel volume was used. A single 45º pitched downward pumping impeller was placed approximately one third of the aqueous phase height from the bottom of the vessel and operated at 30.0 rev/s. Compared to alternative configurations, this setup was shown to produce the best aqueous phase mixing, while largely avoiding gas entrainment. No baffles were included as there was no large central vortex produced in their absence due to effective baffling of the reactor by

the internal equipment. In addition, the baffles produced no effect on the onset of gas entrainment. The Parr reactor was shown to provide adequate T control to 363 K, which was used as a practical limit for subsequent experiments. Gas entrainment was apparent for experiments with $\rho_{wet\ CO2}$ of 0.25 g/cm^3 and greater, which was used as another practical limit for subsequent experiments.

5.1.2 Designed Experiment Results

The functional dependence of k_L upon T, $\rho_{wet\ CO2}$ and S_{NaCl} developed in this research indicates that for greater T and smaller S_{NaCl}, there is an increase in k_L. There is an effect on k_L from the interaction between T and $\rho_{wet\ CO2}$. For T less than 336 K, k_L increases with increasing $\rho_{wet\ CO2}$. However, for T greater than 336 K, k_L decreases with increasing $\rho_{wet\ CO2}$. While the S_{NaCl} dependency was demonstrated to be statistically significant, the large value selected was representative of a niche application, that of effluent from a desalination plant. As a result, for most applications in which brine is sourced from the storage formation it may be neglected, leaving k_L a function of T and $\rho_{wet\ CO2}$ alone. A possible S_{CaCl2} dependency was not shown to be statistically significant.

5.2 Application

The k_L value calculated from Experiment 6, 0.033 cm/s, was used for several mass transfer calculations. Experiment 6 was selected as it best represents typical conditions for optimum surface dissolution, namely T = 308 K, $\rho_{wet\ CO2}$ = 0.187 g/cm^3, S_{NaCl} = 0.6 m and S_{CaCl2} = 0.2 m. The process configurations included co-injection of CO_2 and brine at the wellhead, co-injection in a horizontal pipe and use of a mixing tank.

5.2.1 Wellhead Co-Injection

Using an optimum well depth from Burton (2008) and an optimum brine injection rate from Jain (2011), a stoichiometric CO_2 rate was calculated for co-injection of CO_2 and brine at the wellhead for injection into a typical aquifer. The bulk phase CO_2 was modeled as a stream of uniform radius bubbles, which move at the same speed as brine down the wellbore, shrinking due to increased *P* and dissolution as they move. The goal of this process is complete dissolution of bulk phase CO_2 within the wellbore, so the point at which this takes place was calculated for 4 inch and 6 inch wellbores and a variety of bubble sizes.

A smaller wellbore requires a faster fluid velocity compared to a larger wellbore for the same flow rate, due the smaller area available. This leads to a smaller residence time for a 4 inch wellbore and a deeper point at which the bubbles completely dissolve when compared to a 6 inch wellbore. For a 6 inch wellbore and the discrete bubble sizes considered, bubbles larger than 0.31 cm radius do not completely dissolve prior to entering the formation. Thus the is the objective of the approach is not achieved in this case. In contrast, bubbles of 0.31 cm radius and smaller completely dissolve before arriving at the bottom of the well. 0.31 cm radius bubbles completely dissolve at 1330 ft and at a depth of 670 ft, 0.16 cm radius bubbles completely dissolve. For the 4 inch wellbore, complete dissolution of bulk phase CO_2 occurs at 1480 ft for 0.16 cm radius bubbles and 0.31 cm radius bubbles do not dissolve completely in the wellbore. While the bubble size and wellbore radius are critical, it is feasible to design the process for complete dissolution prior to injection into the storage structure.

5.2.2 Horizontal Pipe Co-Injection

The total brine rate required for the dissolution of a CO_2 stream from a typical coal fired power station was obtained from Jain (2011). Using a fraction of the corresponding stoichiometric CO_2 rate to ensure a bubble flow regime, the distance along a single large diameter horizontal pipe for complete dissolution of bulk phase CO_2 was calculated. The results indicated that this was at a distance of 500 ft for 0.31 cm radius bubbles and 230 ft for 0.16cm radius bubbles. Since the CO_2 rate is limited by flow regime, at this distance or less a second stream of CO_2 would be injected to produce brine at the desired CO_2 concentration for the target aquifer. These distances are small compared to the many miles of pipeline in use in the oil and gas industry and demonstrate that this configuration could be used practically.

5.2.3 Mixing Tank

Using the time to 90% of CO_2 dissolution calculated from the forward model, a calculation of the volume required for a mixing tank was completed. This calculation was based on a 100-fold increase in area due to gas entrainment and the same total brine rate used for the horizontal pipe calculation. The result was a relatively small tank volume of only 124 b ($20m^3$), which is small compared to the large tanks used in industry.

5.3 Future Work

5.3.1 Simultaneous CO_2 Dissolution and CH_4 Production

There is a niche application of simultaneous CO_2 dissolution and CH_4 production from brine. To understand the kinetics of this process, the existing apparatus could be used to conduct similar batch experiments to those described above, using the same

procedure and methane saturated brine. However, additional experimental equipment would be required. The data processing technique described in section 3.5.3 'Data Processing Technique' calculates instantaneous dissolved CO_2 concentration from the *P* at any time using an assumption that CO_2 is the only component being transported between phases. If CH_4 is moving from brine to vapor phase simultaneously with CO_2 moving from vapor phase into brine, the composition of at least one phase must be measured directly to allow calculation of transport of each.

5.3.2 Flue Gas Dissolution

The CO_2 capture process used as part of standard sequestration typically consumes 30% of the energy produced by the power station (Burton, 2008). Assuming a 30% loss leads to a required increase in generating capacity of 43% to produce the same net power as a power station not fitted with a CO_2 capture system. However, if the capture process was achieved by dissolving flue gas into brine that was lifted from the reservoir for the surface dissolution strategy, this large power loss would be avoided entirely.

Similarly to the possible simultaneous CO_2 dissolution and CH_4 production experiments proposed above, with the addition of the ability to directly measure the composition of at least one phase, the kinetics of this process could be studied for each component.

5.3.3 Co-Injection Experiments

The measured k_L was applied to a number of scenarios using simple mass transport models. Each of these models assumed that a was known precisely. While reasonable assumptions were made, a new experimental apparatus allowing co-injection of CO_2 and brine would either validate these assumptions or demonstrate the need for their refinement.

5.3.4 Refinement of Transport Models and Optimization of Process

Many simplifications were made in developing the transport models used to calculate the depth at which bulk phase CO_2 dissolves in a wellhead co-injection scenario and the distance along a horizontal pipe in such a process configuration. These simplifications include no liquid or gas holdup and a frictional P drop due to a single phase of brine flowing, as discussed in detail in section 4.1.2 'Rates and Concentrations at Typical Operating Conditions'. These assumptions are conservative, that is, the result in terms of the depth in a well or distance along a horizontal pipe is deeper or longer than it would otherwise be if they were not made. To a degree, this simplification leads to over-engineering the process. For example, if these factors were taken into account, the required maximum bubble size calculated would be larger. This may be important if significant hydraulic power is required to produce smaller bubbles through nozzles.

The bubble size distribution used in the transport models for co-injection was uniform. This leads complete dissolution lengths for the largest bubble of a distribution. A more realistic distribution could be used from the outset, which would refine the instantaneous CO_2 concentration distribution along the wellbore or pipe.

Finally, while the three process configurations modeled were all determined to be feasible, the costs of each were not examined in great detail, which would allow selection based on the lowest cost or a combination of cost and other factors such as process failsafe considerations.

Appendices

APPENDIX A: SOLUBILITY TUNING STEPS FOR $CaCl_2$ BRINE

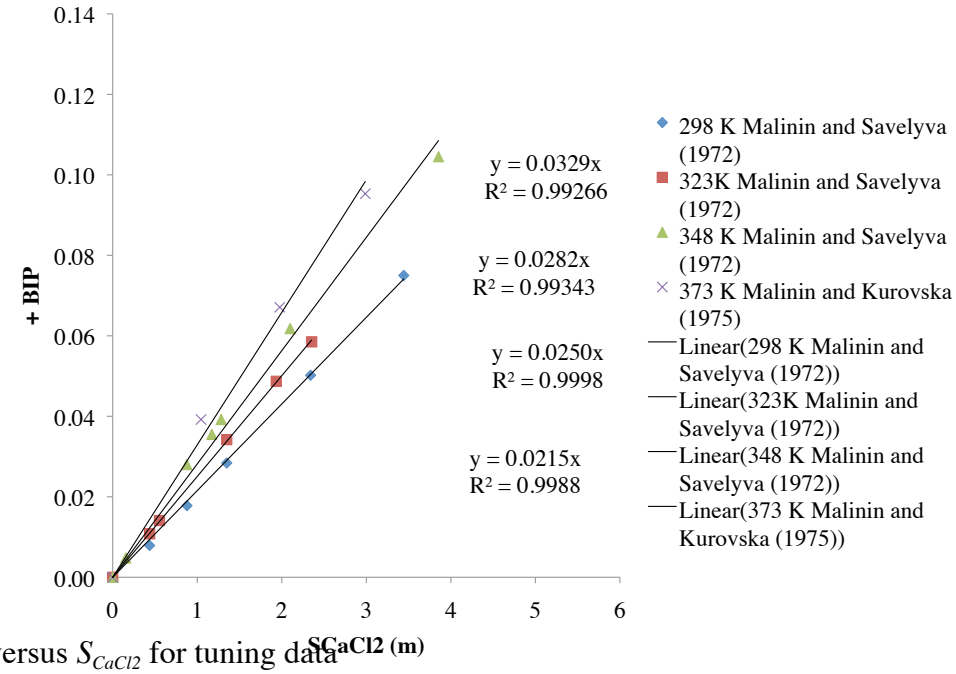

$+BIP$ versus S_{CaCl2} for tuning data

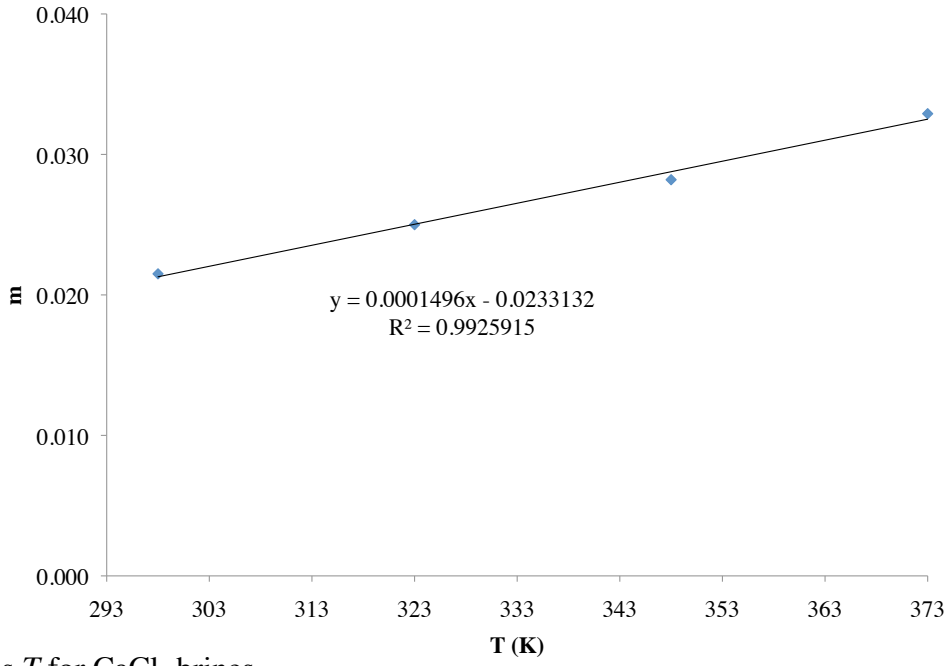

m versus T for $CaCl_2$ brines

APPENDIX B: TUNED PR EOS FLASH COMPARISON TO DUAN AND SUN MODEL

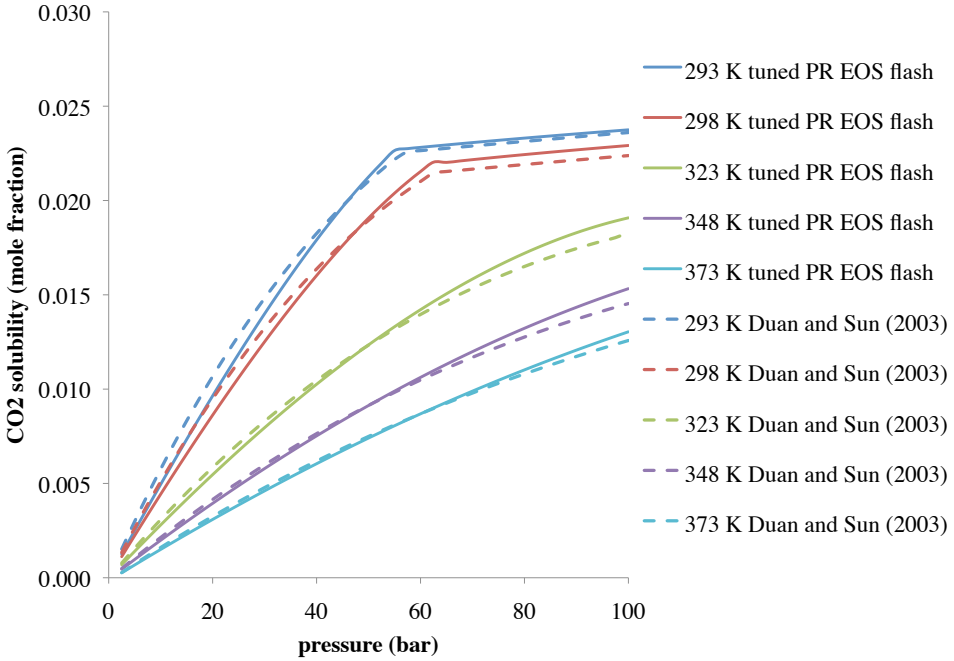

Comparison between the tuned PR EOS flash and the Duan and Sun (2003) model, for 0.5 m NaCl aqueous solutions

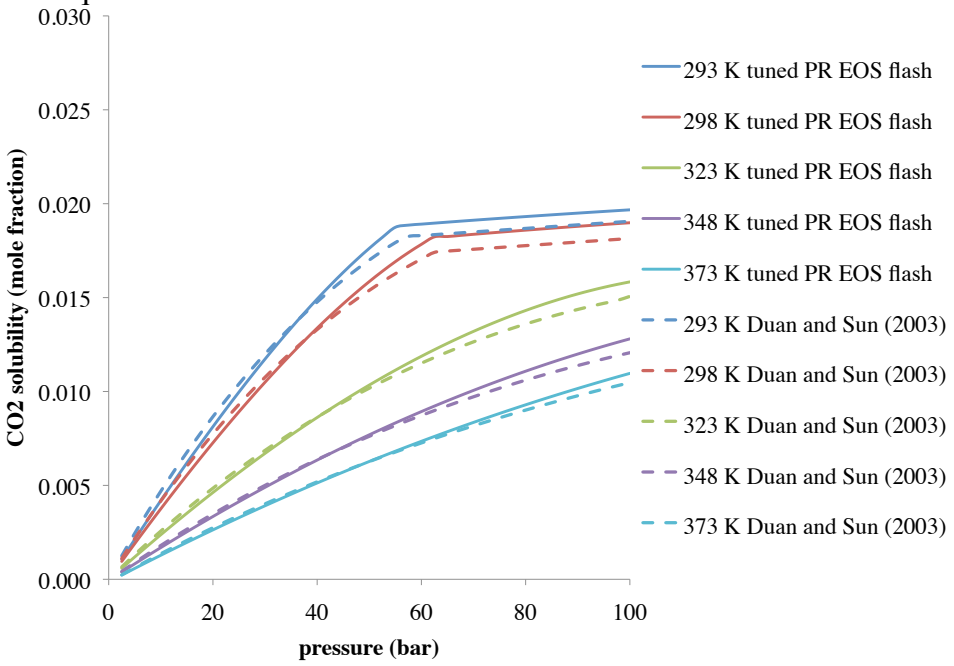

Comparison between the tuned PR EOS flash and the Duan and Sun (2003) model, for 1.5 m NaCl aqueous solutions

APPENDIX C: CALCULATION OF EXPECTED PRESSURE DROP

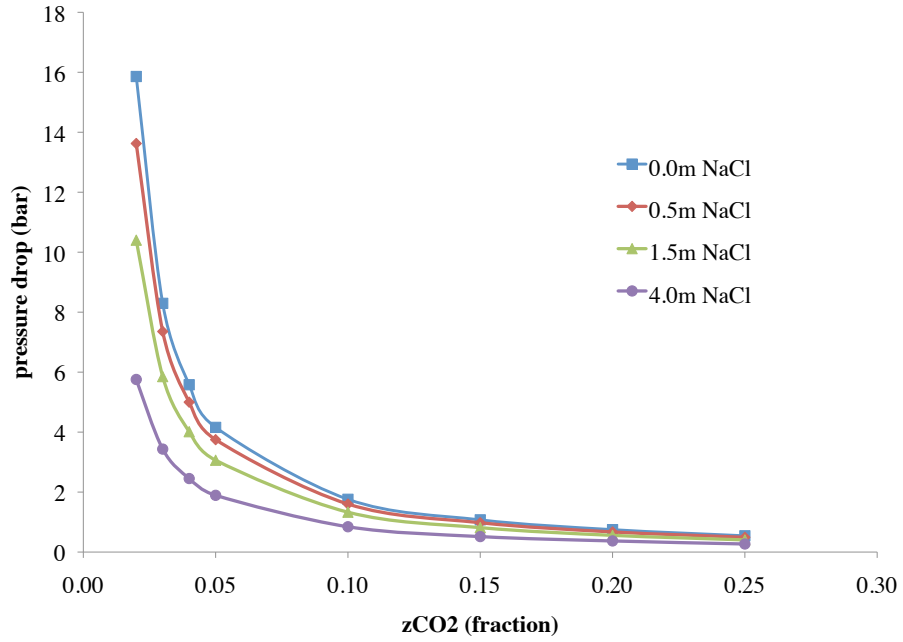

Calculated P drop versus z_{CO2}, $P^{equilibrium}$ = 20 bar

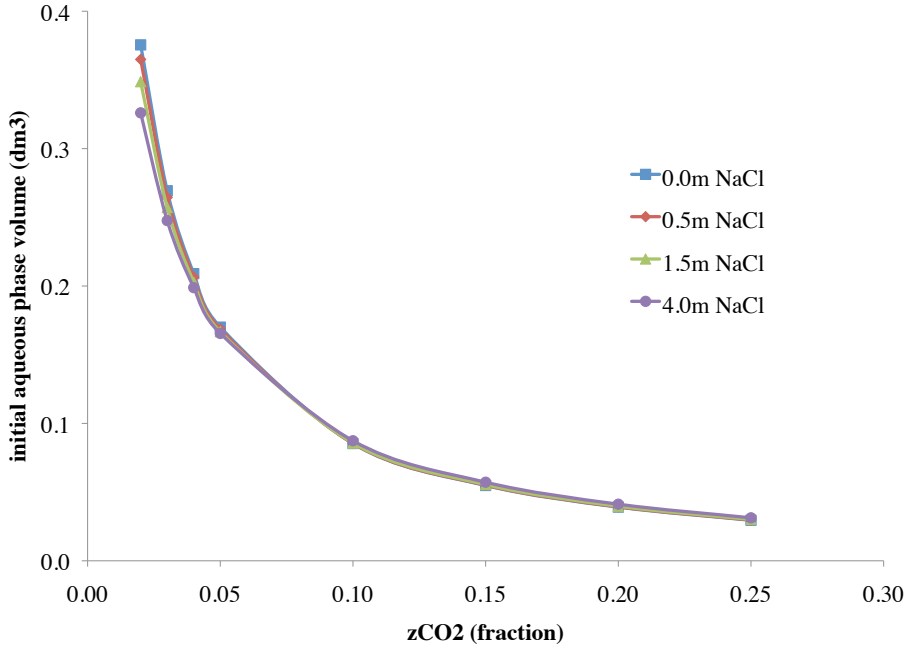

Initial aqueous phase volume versus z_{CO2}, $P^{equilibrium}$ = 20 bar

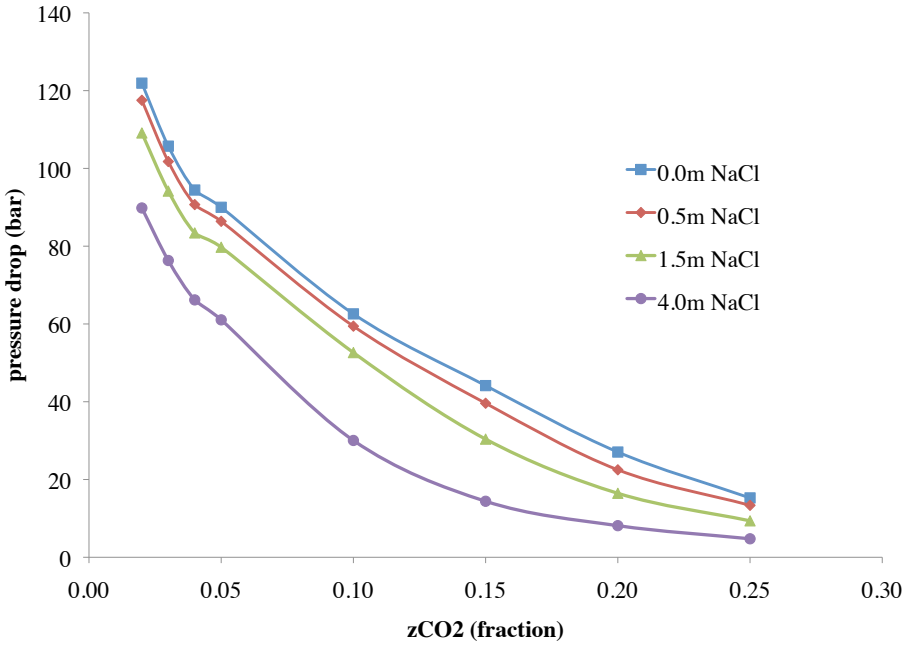

Calculated P drop versus z_{CO2}, $P^{equilibrium}$ = 70 bar

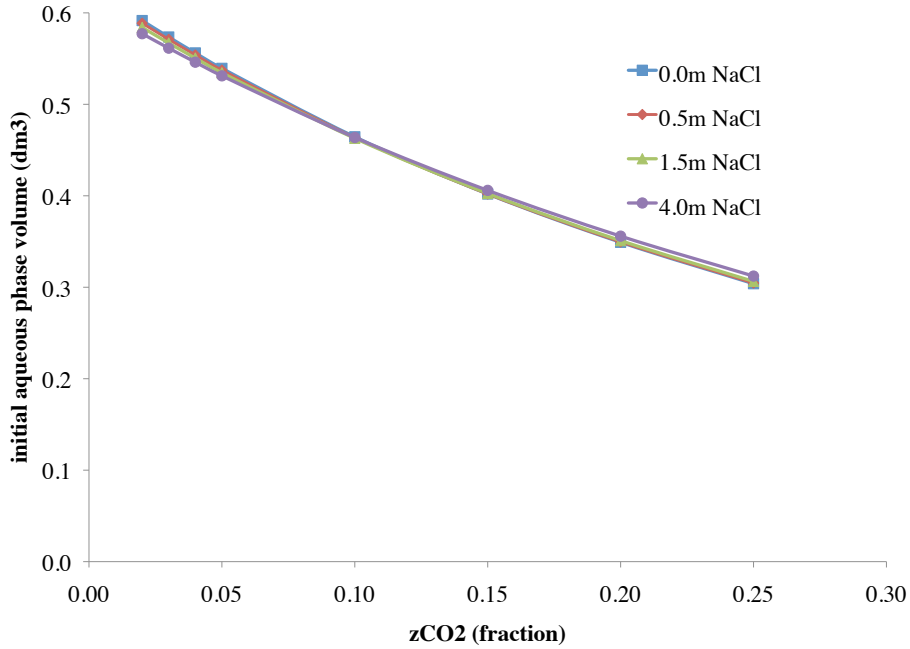

Initial aqueous phase volume versus z_{CO2}, $P^{equilibrium}$ = 70 bar

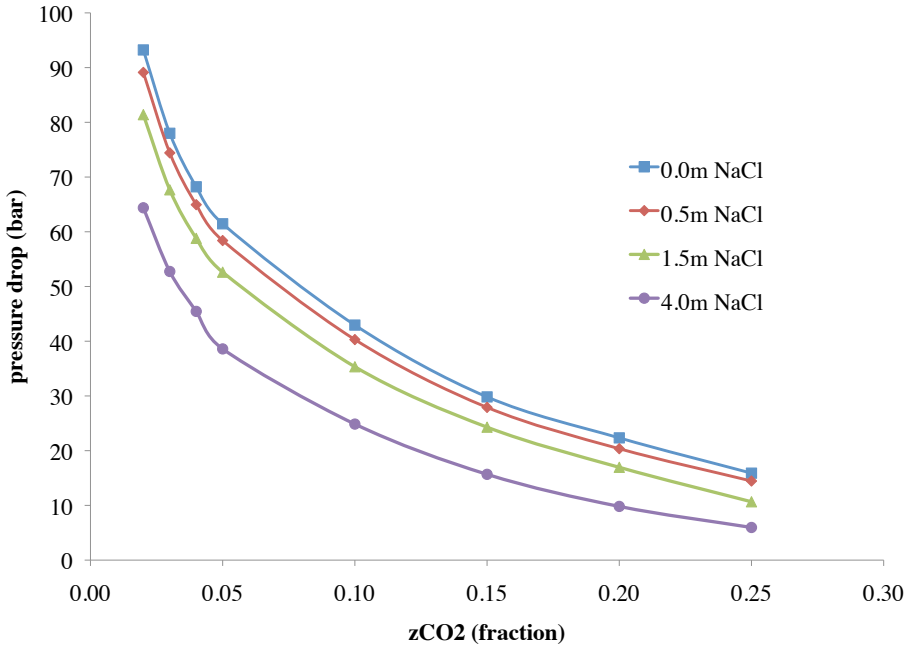

Calculated P drop versus z_{CO2}, $P^{equilibrium}$ = 100 bar

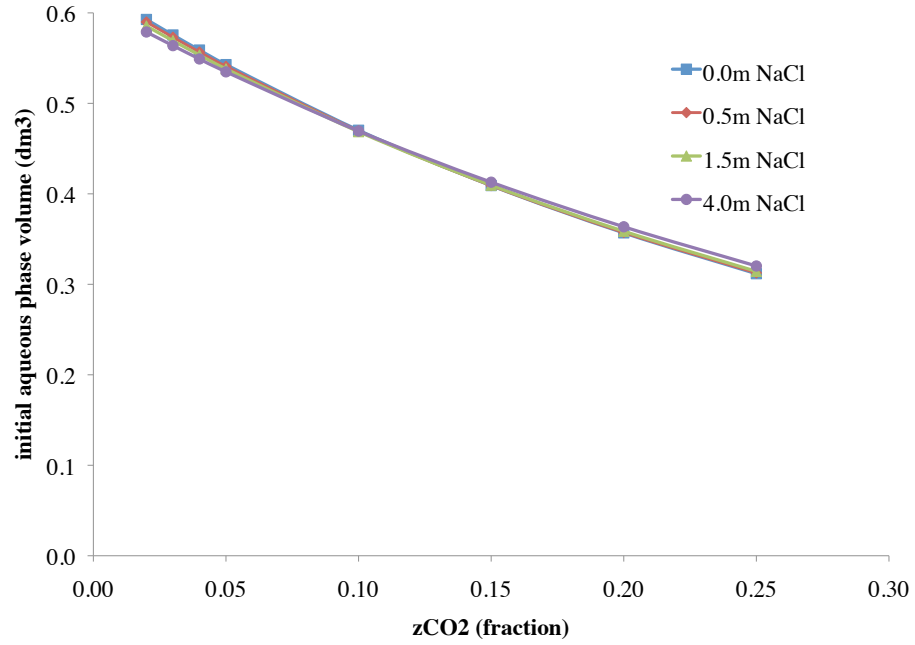

Initial aqueous phase volume versus z_{CO2}, $P^{equilibrium}$ = 100 bar

APPENDIX D: EXPERIMENT DATA SHEET

Mass transfer of carbon dioxide into brine experimental procedure
September 6th, 2011

Date		(mm/dd/yyyy)
Time data recording commenced		(hh:mm)
Experiment number		
Stirrer configuration		
Stirrer rotational speed		(rpm)
Metering valves number of turns open		(turns)
ISCO pump constant pressure setting		(psig)
Steady state water only flowrate from pump through metering valves (ISCO reading)		(mL/min)
Steady state water only pressure shown on pump (ISCO reading)		(psig)
Steady state water only pressure in Parr vessel (Parr reading)		(psig)
Time when phases were brought into contact		(counter)
Time when bottom drain valve was opened		(counter)
Time when bottom drain valve was closed		(counter)
Initial pressure in Parr vessel when bottom drain valve was closed		(psig)
Time when gas fill valve was closed		(counter)
Time the motor was started		(counter)
Brine NaCl molality		(m)
Brine $CaCl_2$ molality		(m)
Target mass of aqueoous phase (mass of water + mass of salt) drained from Parr vessel		(g)
Mass of aqueous phase (mass of water + mass of salt) drained from Parr vessel		(g)
Temperature (accumulator / line / vessel)		(°C)

Brine preparation
NaCl molar mass = 58.443 g/mol
$CaCl_2$ molar mass = 110.986 g/mol

Water mass		(g)
NaCl mass		(g)
$CaCl_2$ mass		(g)

Experiment data sheet

APPENDIX E: CO_2 SOLUBILITY VERSUS *P* FOR VARIOUS *T*

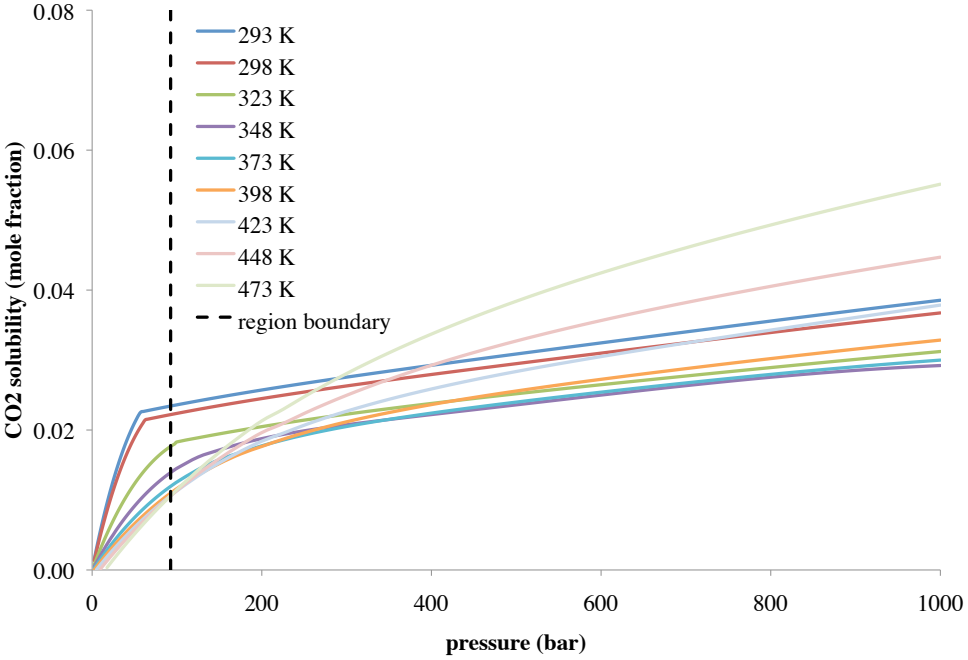

CO_2 solubility in 0.5 m NaCl versus *P* for various *T*, model results from Duan and Sun (2003)

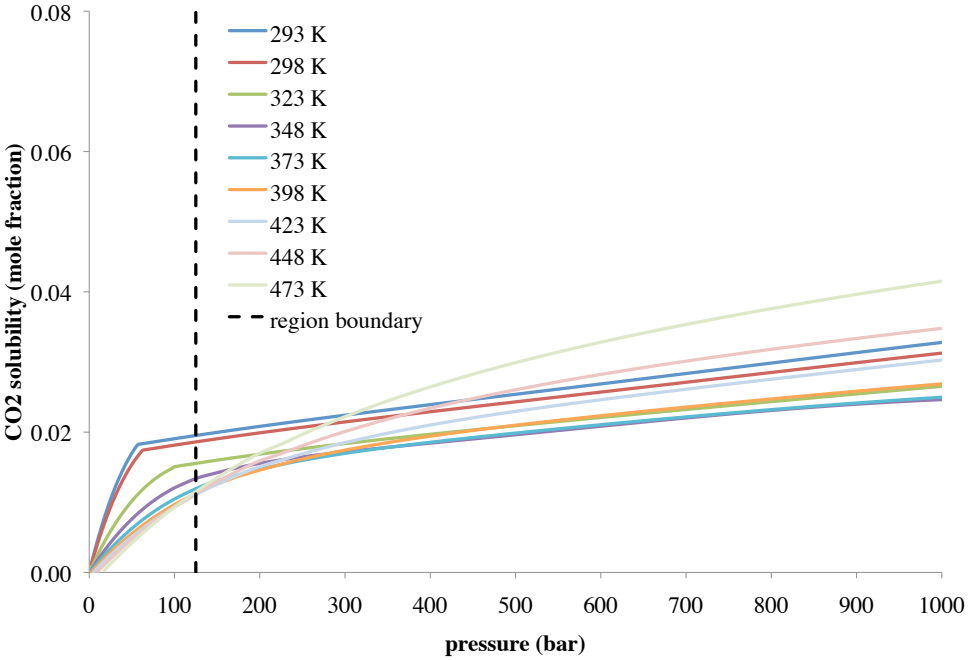

CO_2 solubility in 1.5 m NaCl versus *P* for various *T*, model results from Duan and Sun (2003)

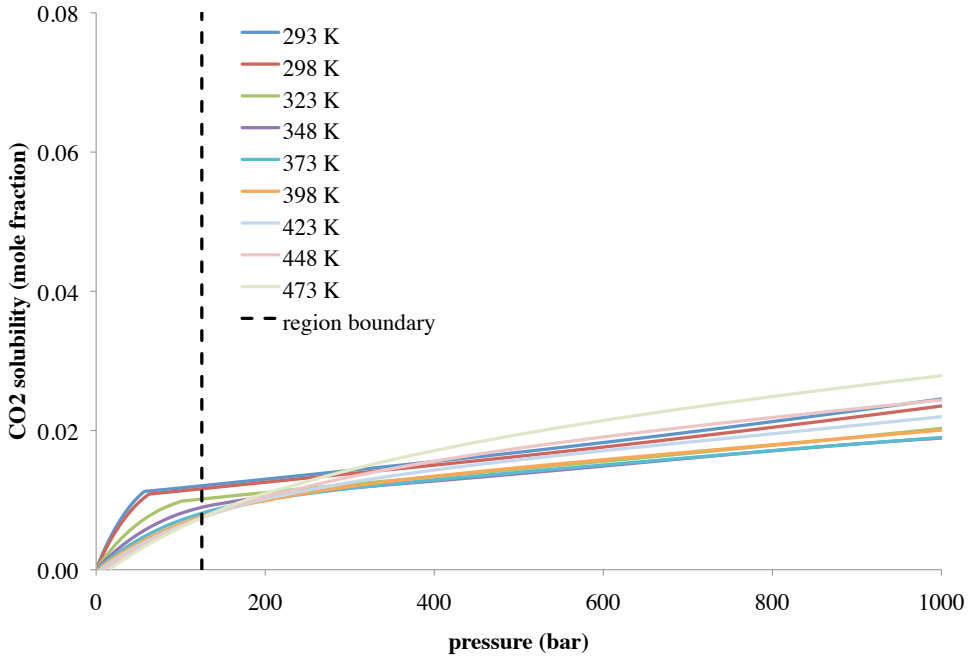

CO_2 solubility in 4.0 m NaCl versus P for various T, model results from Duan and Sun (2003)

APPENDIX F: *P* AND *T* DATA FROM DESIGNED EXPERIMENT

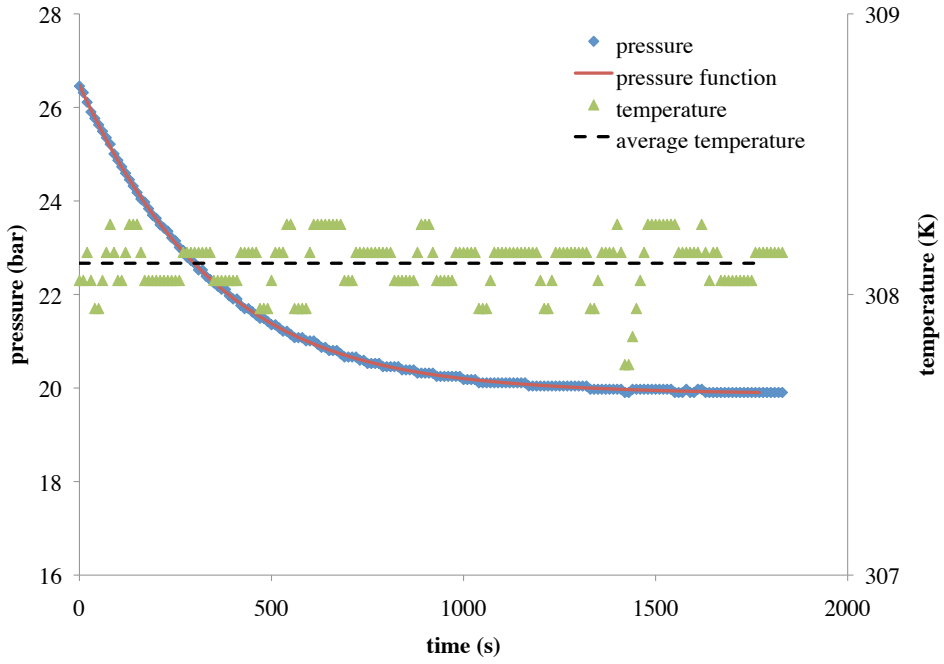

P and *T* versus time for Experiment 2

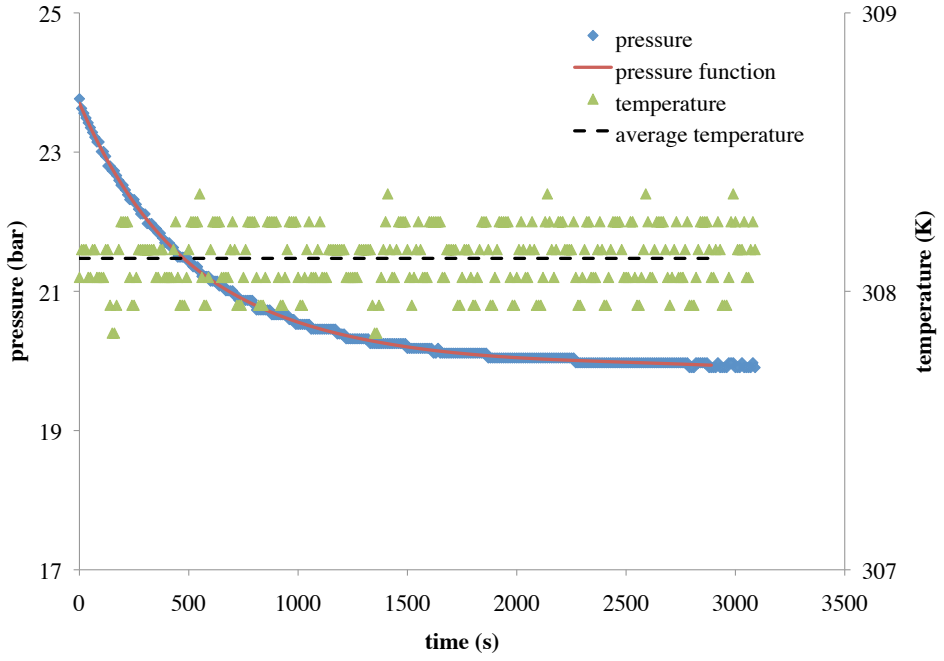

P and *T* versus time for Experiment 3

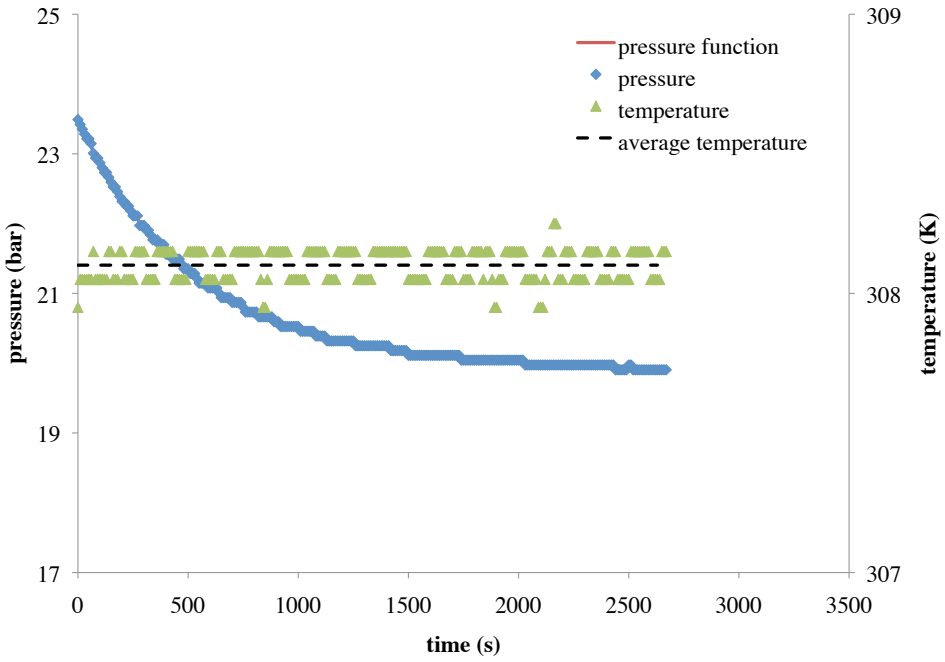

P and *T* versus time for Experiment 4

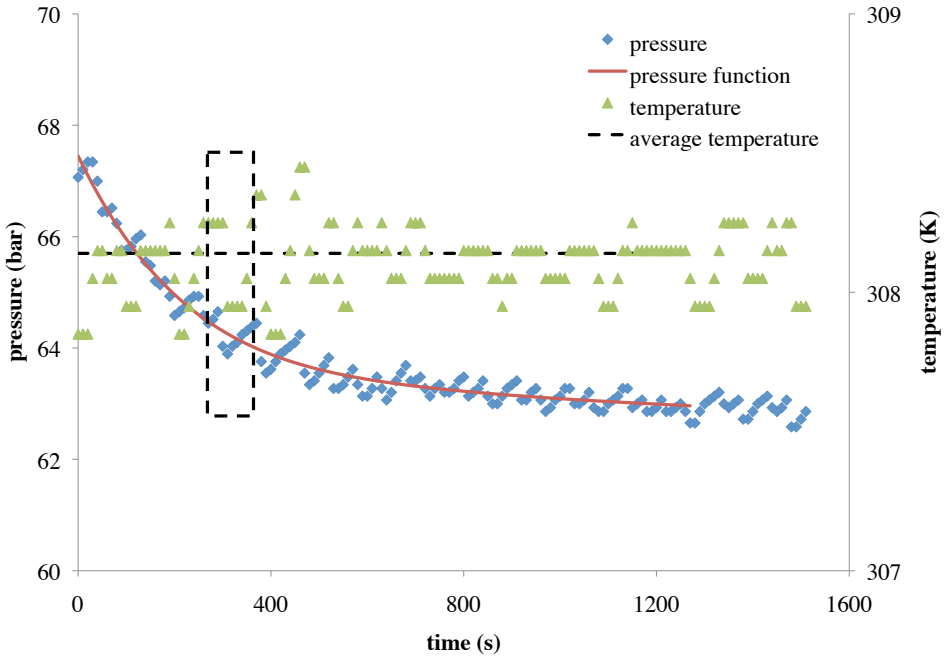

P and *T* versus time for Experiment 5, dashed rectangle shows data selection analyzed in Figure 3.44b

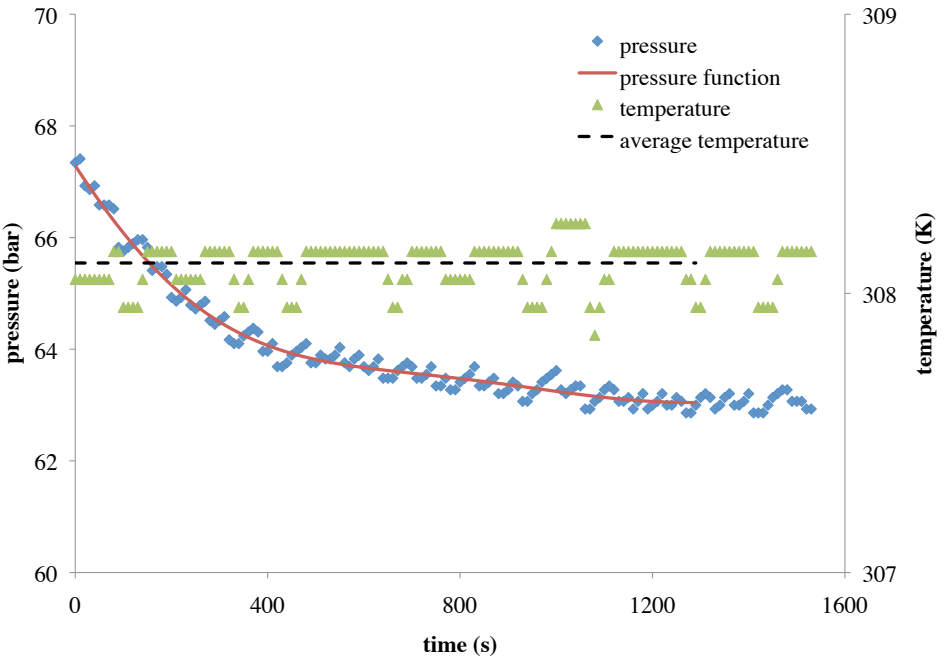

P and *T* versus time for Experiment 6

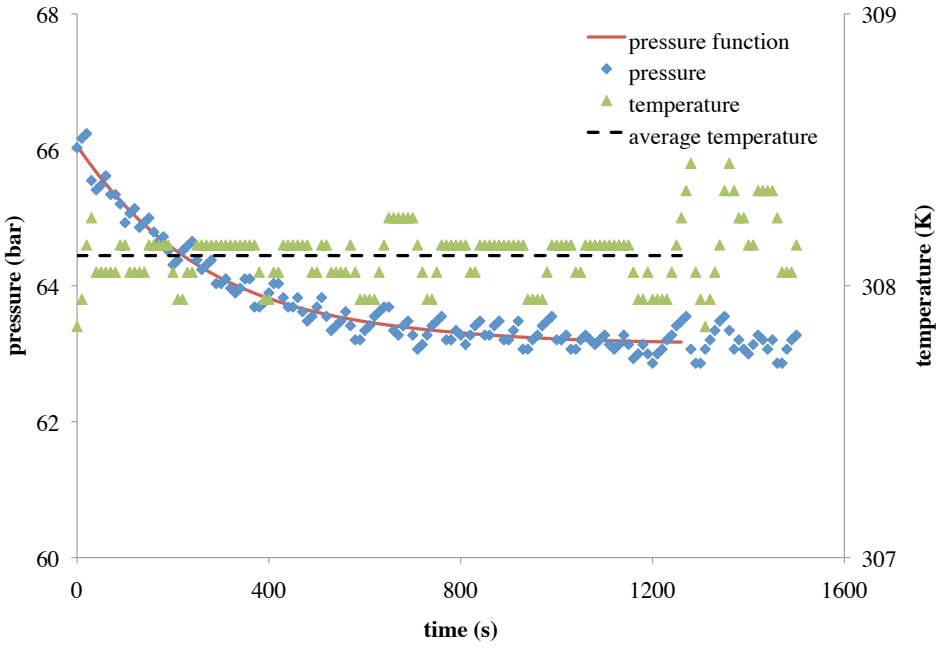

P and *T* versus time for Experiment 7

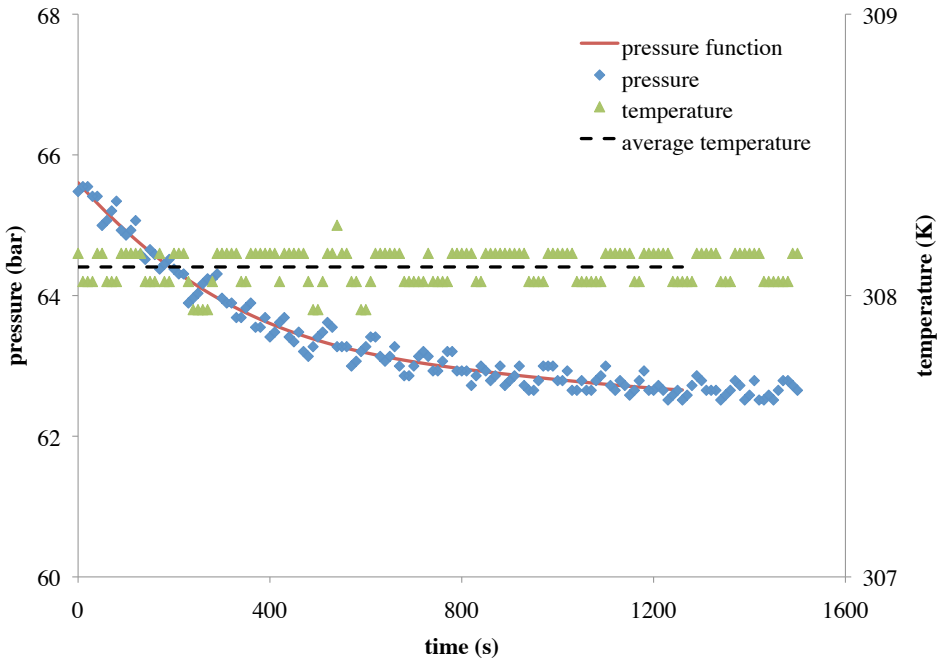

P and *T* versus time for Experiment 8

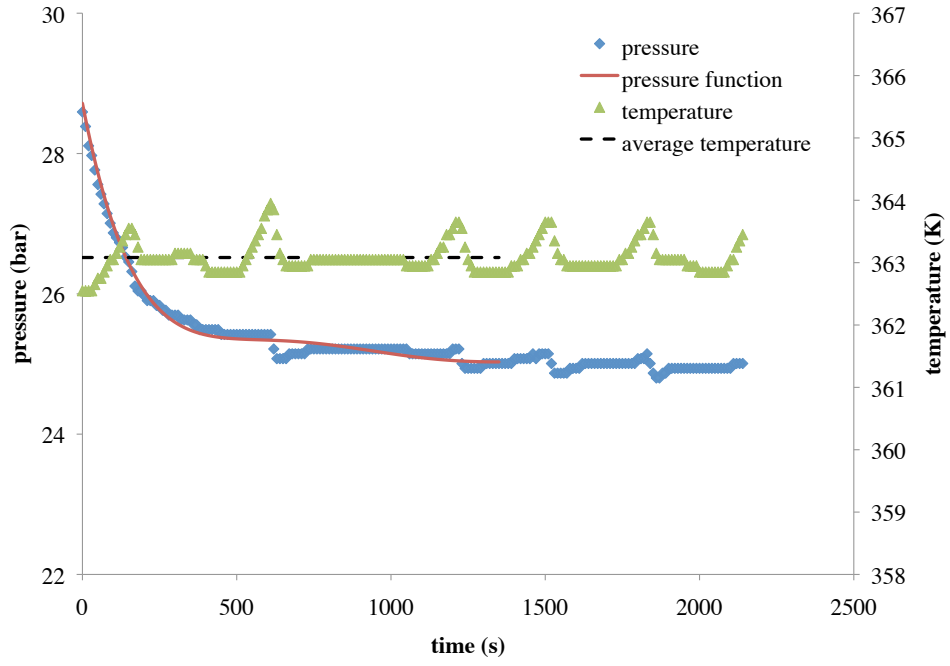

P and *T* versus time for Experiment 9

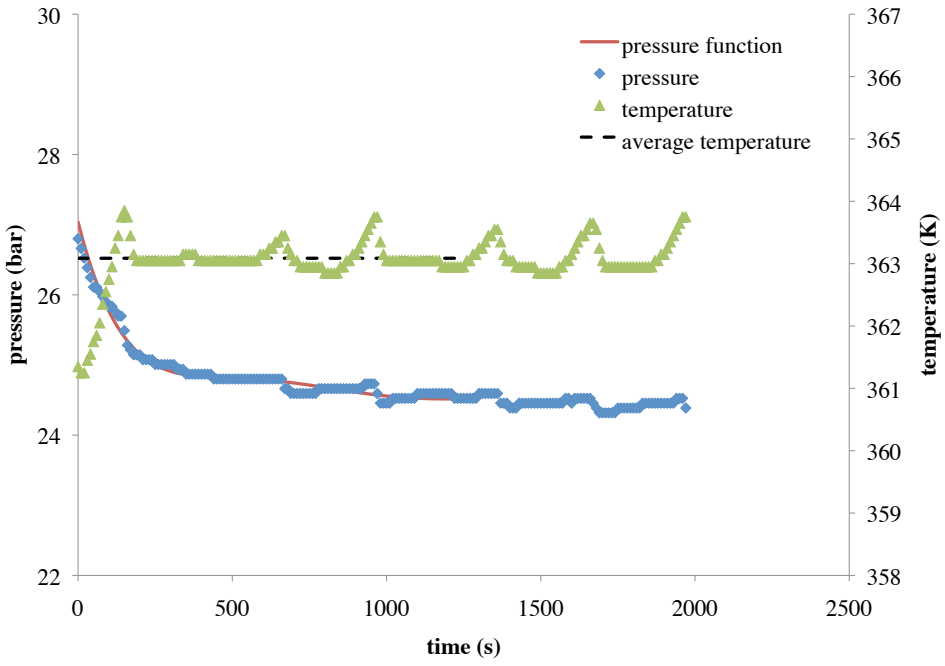

P and *T* versus time for Experiment 10

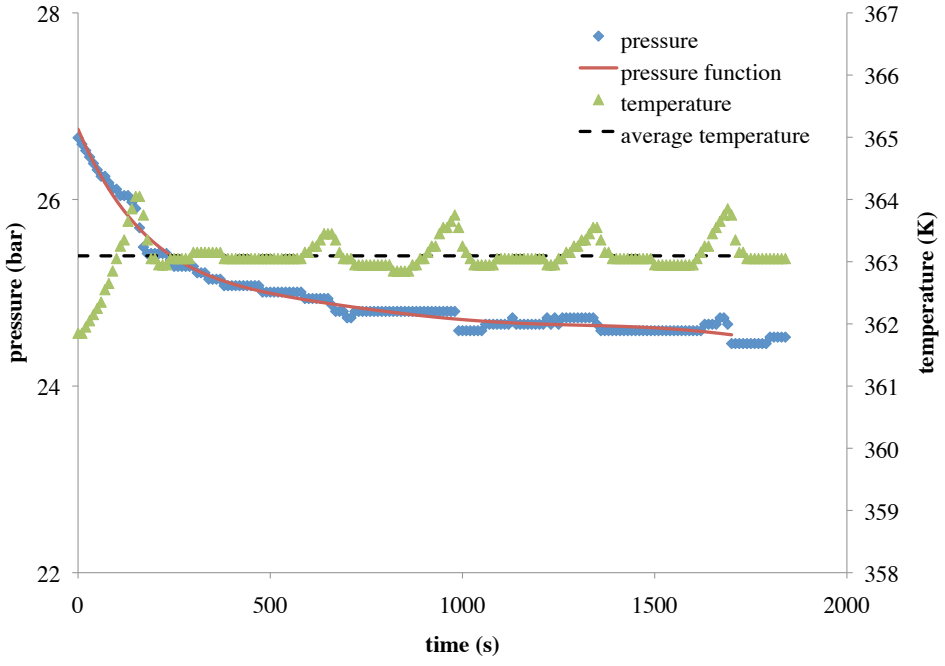

P and *T* versus time for Experiment 11

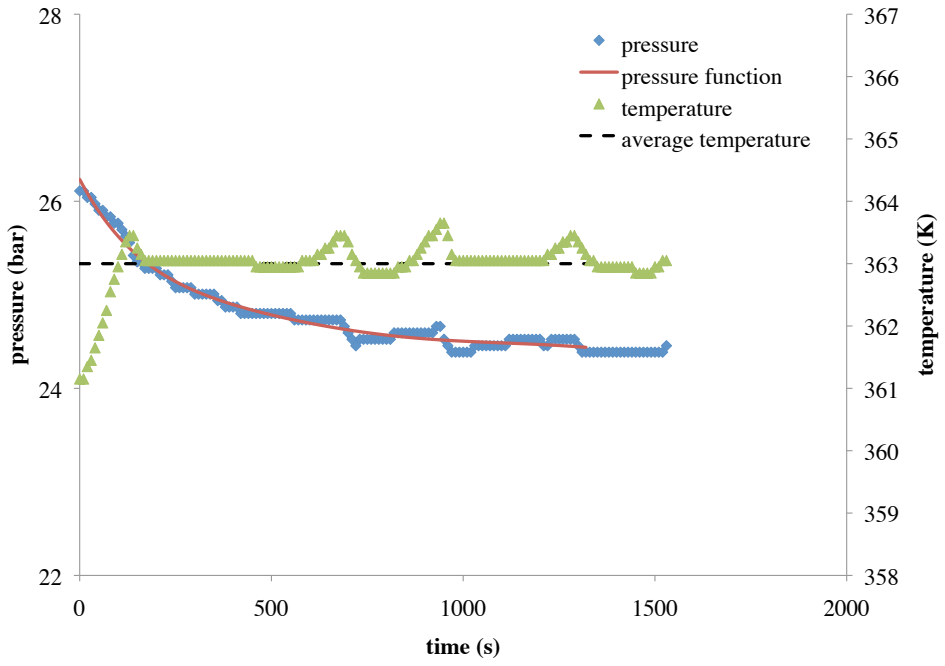

P and *T* versus time for Experiment 12

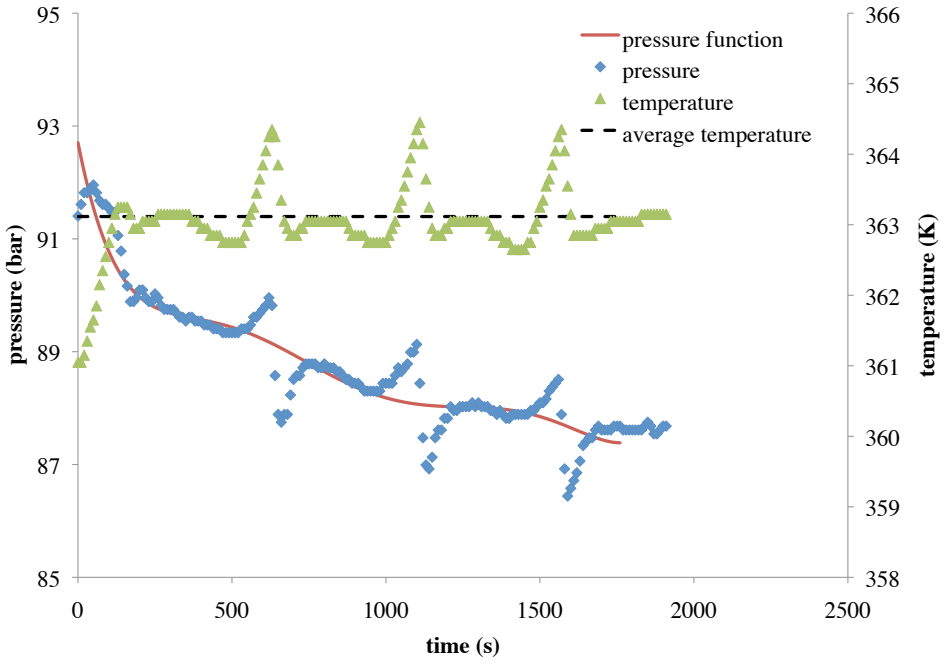

P and *T* versus time for Experiment 13

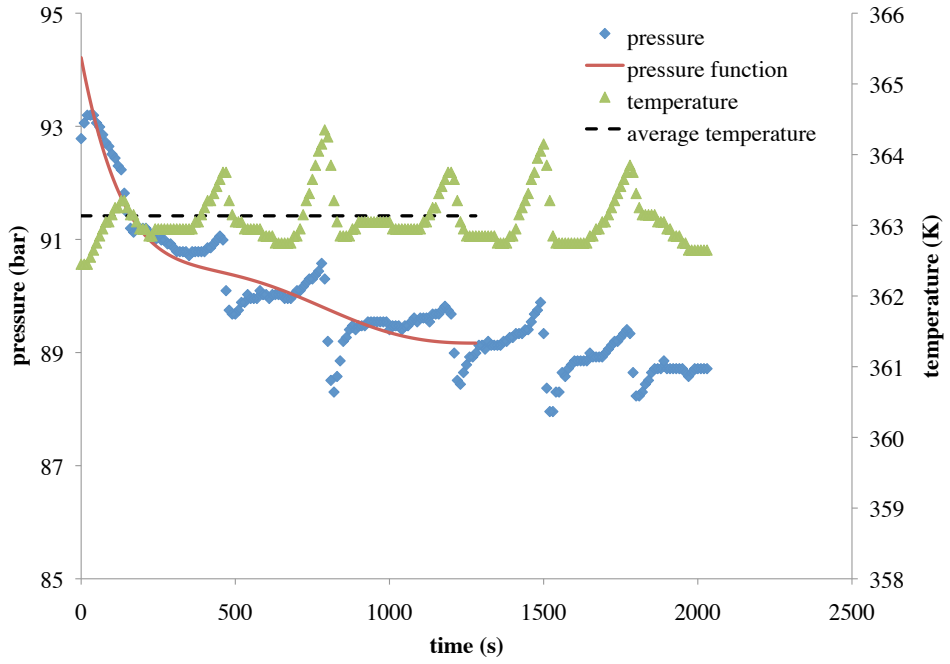

P and *T* versus time for Experiment 14

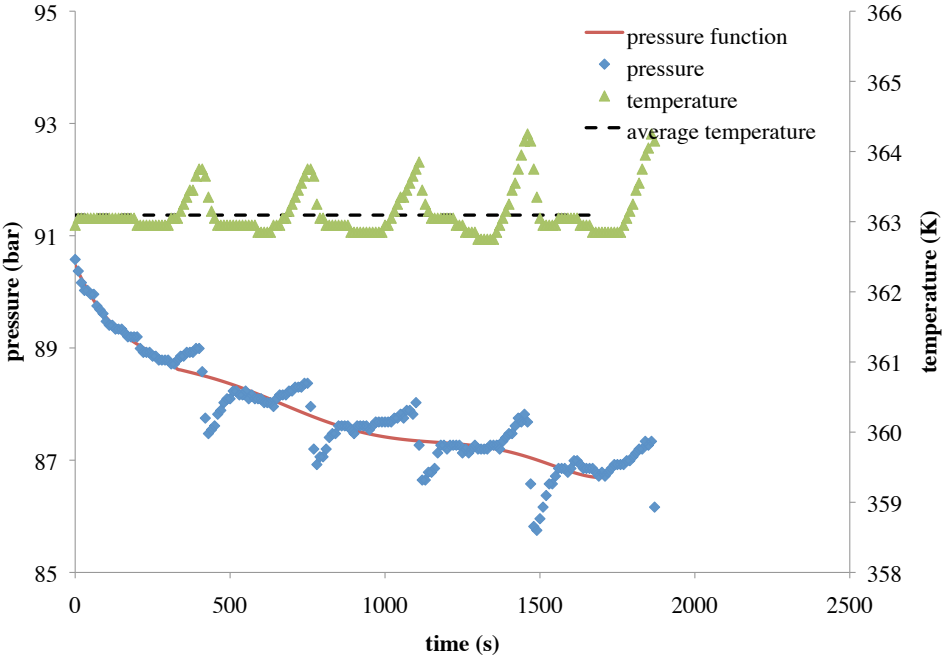

P and *T* versus time for Experiment 15

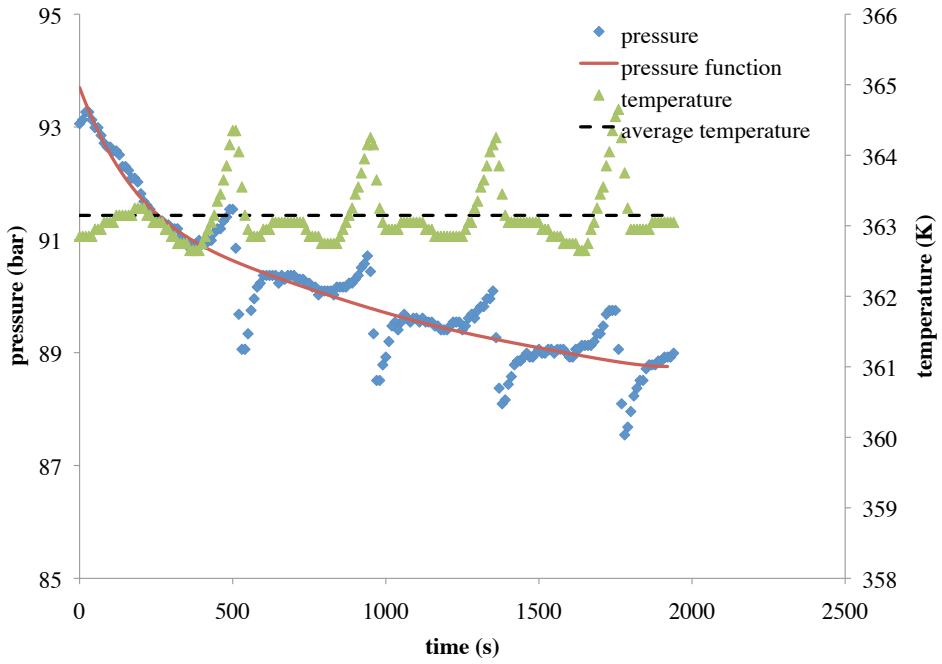

P and *T* versus time for Experiment 16

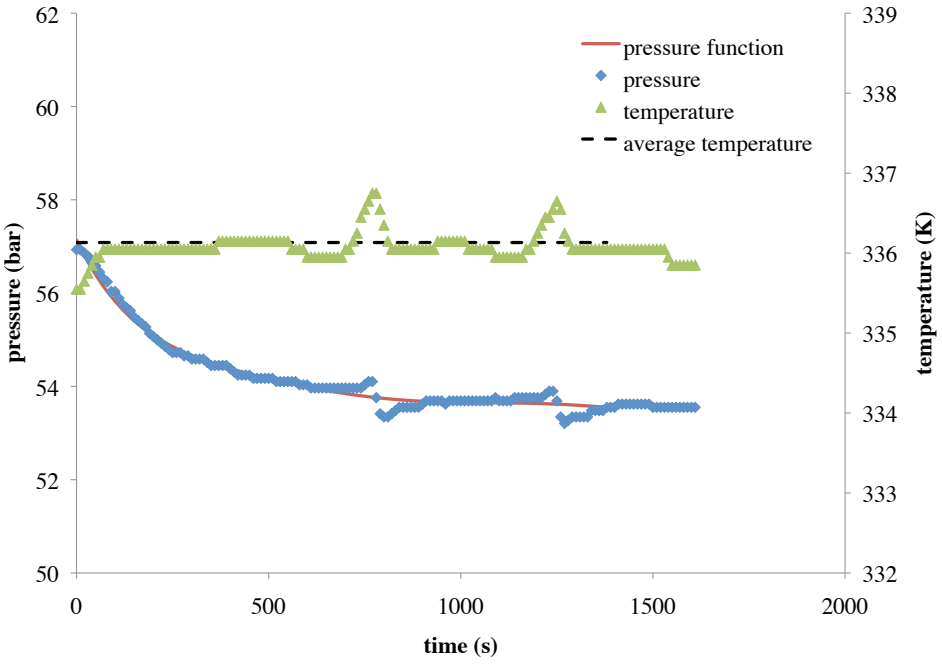

P and *T* versus time for Experiment 17 trial 1

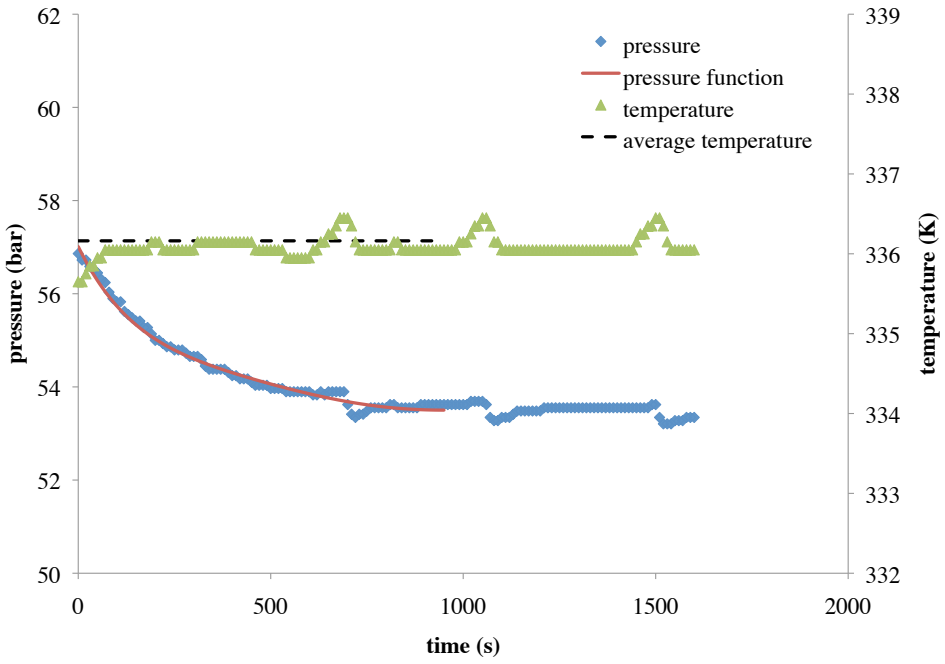

P and *T* versus time for Experiment 17 trial 2

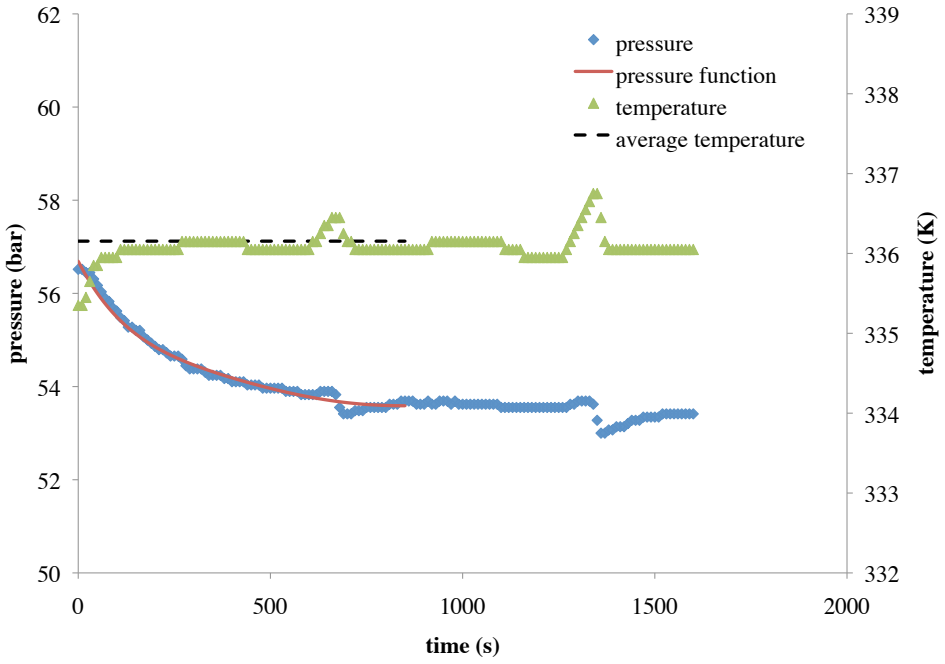

P and *T* versus time for Experiment 17 trial 3

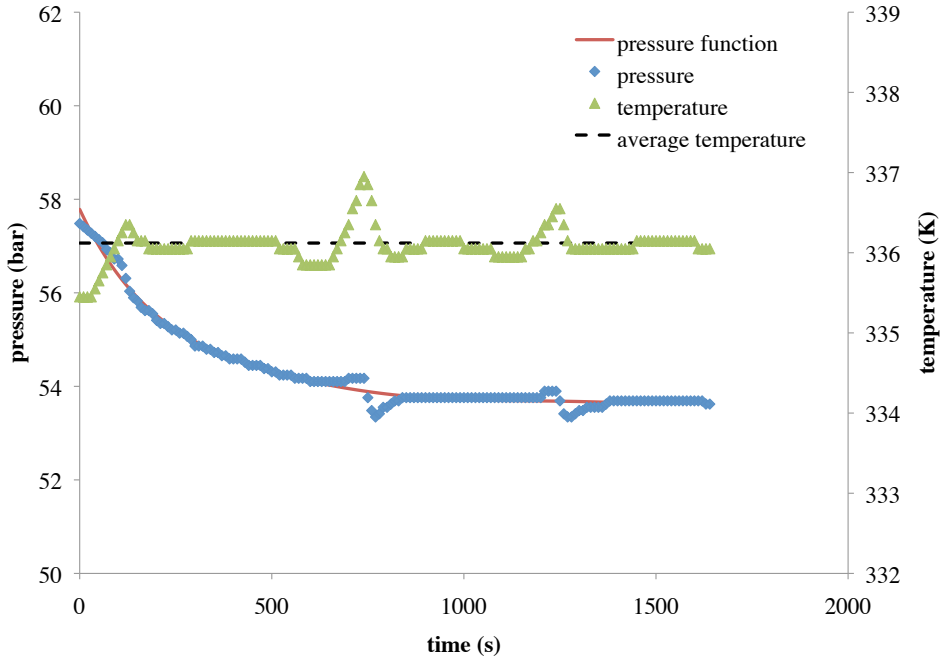

P and *T* versus time for Experiment 17 trial 4

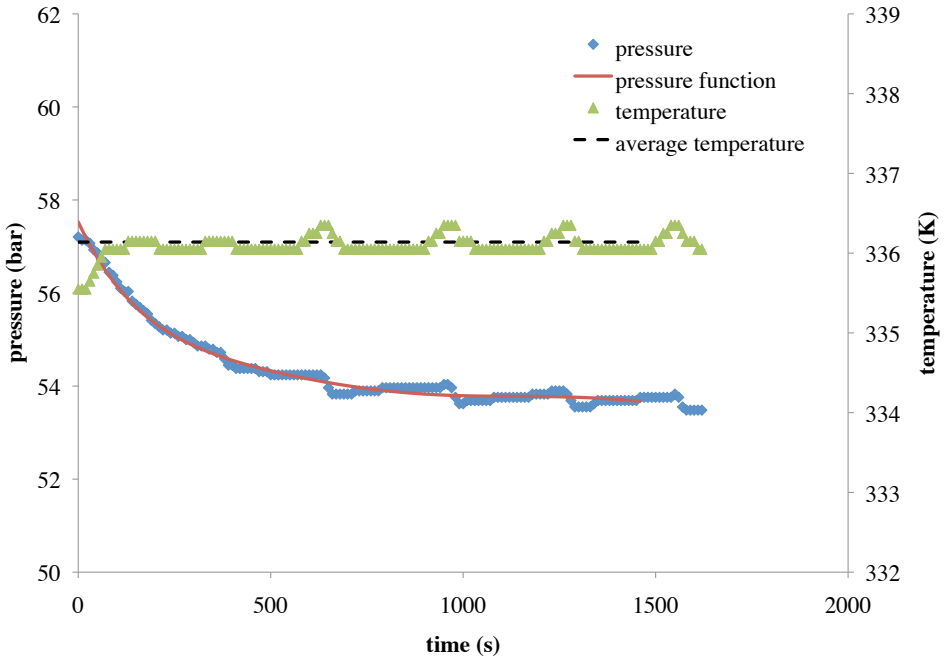

P and *T* versus time for Experiment 17 trial 5

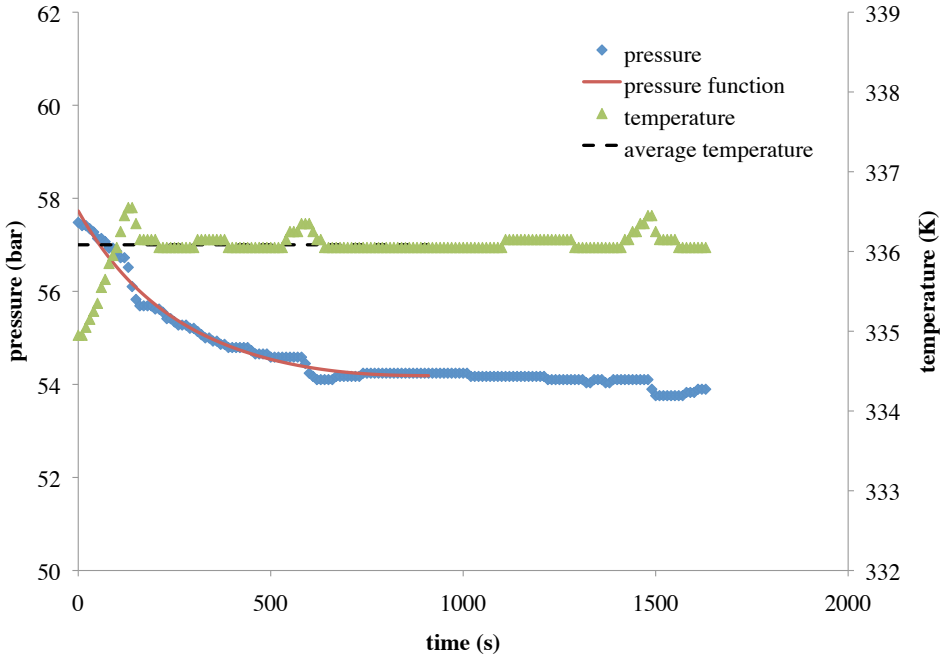

P and *T* versus time for Experiment 17 trial 6

APPENDIX G: k_L VALUES FROM ALTERNATIVE SELECTION PROCEDURE

Experiment	T (K)	$\rho_{wet\ CO2}$ (g/cm^3)	S_{NaCl} (m)	S_{CaCl2} (m)	k_L (cm/s)
1	308	0.047	0.6	0.0	0.029
2	308	0.046	0.6	0.2	0.022
3	308	0.043	4.0	0.0	0.015
4	308	0.042	4.0	0.2	0.015
5	308	0.200	0.6	0.0	0.042
6	308	0.199	0.6	0.2	0.037
7	308	0.191	4.0	0.0	0.037
8	308	0.188	4.0	0.2	0.029
9	363	0.044	0.6	0.0	0.050
10	363	0.042	0.6	0.2	0.056
11	363	0.041	4.0	0.0	0.036
12	363	0.040	4.0	0.2	0.036
13	363	0.186	0.6	0.0	0.047
14	363	0.190	0.6	0.2	0.053
15	363	0.177	4.0	0.0	0.015
16	363	0.182	4.0	0.2	0.013
17, trial 1 to 6	336	0.116, 0.116, 0.116, 0.116, 0.116, 0.118	2.3	0.1	0.043, 0.043, 0.048, 0.038, 0.041, 0.038

Designed experiment results from alternative k_L selection procedure

Nomenclature

General nomenclature

a = interfacial area (m^2 or cm^2)

A = component

B = component

C_A = concentration of A (mol/m^3 or mol/cm^3)

C_{A0} = concentration of A at phase boundary (mol/m^3 or mol/cm^3)

$C_{A\delta}$ = concentration of A at the boundary layer of thickness δ (m) (mol/m^3 or mol/cm^3)

$C_{Asaturation}$ = saturation concentration of A (mol/m^3 or mol/cm^3)

δ = boundary layer thickness (m)

D_{AB} = diffusion coefficient of A in B (m^2/s)

J_{Ax} = molar flux of A in direction x (m) (mol/m^2s)

k_L = liquid-side mass transfer coefficient (m/s or cm/s)

k_La = volumetric liquid-side mass transfer coefficient (m^3/s)

n = a power

N_{iL} = moles of component i in liquid phase (mol)

N_{total} = total moles (mol)

N_V = moles of vapor phase (mol)

M_B = molecular weight of B (g/mol)

μ = viscosity (cp)

P = pressure (bar absolute)

$P_{bottomhole}$ = bottomhole pressure (bar absolute)

$P^{equilibrium}$ = equilibrium pressure (bar absolute)

$P_{friction}$ = friction pressure (bar absolute)

$P_{injection}$ = injection pressure (bar absolute)

P^o = initial pressure (bar absolute)

$P_{storage}$ = storage pressure (bar absolute)

q = rate (b/d)

ρ = density (g/cm^3)

S = salinity (m)

t = time (s)

T = temperature (K)

V = molar volume (dm^3/mol)

V_A = molar volume of A as liquid at its normal boiling point (cm^3/gmol)

V_V = vapor phase molar volume (dm^3/mol)

$Volume_L$ = liquid phase volume (dm^3)

$Volume_{total}$ = total volume (dm^3)

$Volume_V$ = vapor phase volume (dm^3)

x = direction (m)

ψ_B = association parameter for B

Original nomenclature pertaining to IAPWS-IF97

g = specific Gibbs free energy

I = exponent

J = exponent

n = coefficient

p = pressure (bar absolute)

p^* = reducing pressure (bar absolute)

π = reduced pressure

T^* = reducing temperature (K)

τ = inverse reduced temperature

v = specific volume (cm^3/g)

Original nomenclature pertaining to the model of Mao and Duan (2008)

A_v = volumetric Debye-Huckel limiting law slope

b = constant ($kg^{0.5}/mol^{0.5}$)

B_V = second virial coefficient

c = coeffcient

C_V = third virial coefficient

$h(I)$ = function of ionic strength

I = ionic strength

m = salt molality (m)

m_r = reference salt molality (m)

M_s = molar mass of chlorides (g/mol)

ρ_{H2O} = water density (g/cm^3)

ρ_{sol} = brine density (g/cm^3)

v = sum of number of anion charges and cation charges

v_+ = number of anion charges

v_- = number of cation charges

V = solution volume

z_+ = anion charge

z_- = cation charge

Original nomenclature pertaining to the model of Li *et al*. (2008)

a = coefficient

K = density perturbation

m_{CO2} = CO_2 molality (m)

m_{NaCl} = NaCl molality (m)

ρ = CO_2 laden brine density (g/cm^3)

ρ_B = brine density (g/cm^3)

ρ_W = water density (g/cm^3)

Original nomenclature pertaining to the Peng-Robinson Equation of State

a = repulsion term

$a\alpha^L$ = product of a and α for liquid phase

$a\alpha^V$ = product of a and α for vapor phase

α = temperature dependent function

A^L = coefficient in cubic of compressibility factor Z for liquid phase

A^V = coefficient in cubic of compressibility factor Z for vapor phase

b^L = attraction parameter for liquid phase

b^V = attraction parameter for vapor phase

B^L = coefficient in cubic of compressibility factor Z for liquid phase

B^V = coefficient in cubic of compressibility factor Z for vapor phase

δ_{ij} = binary interaction parameter for i and j

f_i^L = component fugacity of component i in liquid phase (bar)

f_i^V = component fugacity of component i in vapor phase (bar)

G = Gibbs free energy

κ = quadratic function

n_L = liquid phase mole fraction

n_V = vapor phase mole fraction

N_c = number of components

P_c = critical pressure (bar absolute)

ϕ_i^L = fugacity coefficient for component i in liquid phase

ϕ_i^V = fugacity coefficient for component i in vapor phase

T_c = critical temperature (k)

T_r = reduced temperature

ω = accentric factor

x_i = liquid phase mole fraction of component i

y_i = vapor phase mole fraction of component i

z_i = overall mole fraction of component i

k_i = ratio of y_i to x_i

Z = compressibility factor

Z^L = compressibility factor for liquid phase

Z^V = compressibility factor for vapor phase

Bibliography

Bahar, M. and Liu, K. 2008. 'Measurement of the Diffusion Coefficient of CO_2 in Formation Water Under Reservoir Conditions: Implications for CO_2 Storage'. SPE paper 116513 presented at the SPE Asia Pacific Oil and Gas Conference and Exhibition, Perth, Australia, 20 – 22 October.

Bamberger, A., Sieder, G. and Maurer, G. 2000. 'High-Pressure (Vapor + Liquid) Equilibrium in Binary Mixtures of (Carbon Dioxide + Water or Acetic Acid) at Temperatures from 313 to 353 K'. The Journal of Supercritical Fluids, Volume 17, Pages 97 – 110.

Bhattacharya, S., Hebert, D. and Kresta, S. M. 2007. 'Air Entrainment in Baffled Stirred Tanks'. Chemical Engineering Research and Design, Volume 85, Pages 654 – 664.

Bird, R. B., Stewart, W. E. and Lightfoot, E. N. 2007. Transport Phenomena. Wiley, New York, United States of America.

Boogerd, F. C., Bos, P., Kuenen, J. G., Heijnen, J. J. and M. van der Lans, R. G. J. 'Oxygen and Carbon Dioxide Mass Transfer and the Aerobic, Autotrophic Cultivation of Moderate and Extreme Thermophiles: A Case Study Related to the Microbial Desulfurization of Coal'. Biotechnology and Bioengineering, Volume 35, Pages 1111 – 1119.

Bourgoyne, A. T., Chenevert, M. E., Millheim, K. K. and Young, F. S. 1986. Applied Drilling Engineering. Society of Petroleum Engineers, Texas, United States of America.

BP, 2009. 'BP Announces Giant Oil Discovery in the Gulf of Mexico', press release viewed on March 20th, 2012, http://www.bp.com/.

Bradley, D. J. and Pitzer, K. S. 1979. 'Thermodynamics of Electrolytes. 12. Dielectric Properties and Debye-Huckel Parameters to 350 ºC and 1 Kbar'. The Journal of Physical Chemistry, Volume 83, Number 12, Pages 1599 – 1603.

British Geological Survey. 2012. 'CO_2 Storage Sleipner', website viewed on April 1st, 2012, http://www.bgs.ac.uk/science/CO2/home.html.

Bryant, S. L., Lakshminarasimhan, S. and Pope, G. A. 2008. 'Buoyancy-Dominated Multiphase Flow and Its Effect on Geological Sequestration of CO_2'. SPE Journal, December, Pages 447 – 454.

Burton, M. 2008. 'Surface Dissolution: Addressing Technical Challenges of CO_2 Injection and Storage in Brine Aquifers', MS Thesis, The University of Texas at Austin.

Burton, M. and Bryant, S. L. 2009. 'Eliminating Buoyant Migration of Sequestered CO_2 Through Surface Dissolution: Implementation Costs and Technical Challenges'. SPE Reservoir Evaluation and Engineering, June, Pages 399 – 407.

Calderbank, P. H. and Moo – Young, M. B. 1961. 'The Continuous Phase Heat and Mass – Transfer Properties of Dispersions'. Chemical Engineering Science, Volume 16, Pages 39 to 54.

Cipolli, F., Gambardella, B., Marini, L., Ottonello, G. and Zuccolini, M. V. 2004. 'Geochemistry of High-pH Waters from Serpentinites of the Gruppo di Voltri (Genova, Italy) and Reaction Path Modeling of CO_2 Sequestration in Serpentine Aquifers'. Applied Geochemistry, Volume 19, Pages 787 – 802.

Diamond, L. W. and Akinfiev, N. N. 2003. 'Solubility of CO_2 in Water from – 1.5 to 100°C and from 0.1 to 100 MPa: Evaluation of Literature Data and Thermodynamic Modelling'. Fluid Phase Equilibria, Volume 208, Pages 265 – 290.

Duan, Z., Hu, J., Li, D. and Mao, S. 2008. 'Densities of the CO_2-H_2O and CO_2-H_2O-NaCl Systems up to 647 K and 100 MPa'. Energy and Fuels, Volume 22, Pages 1666 – 1674.

Duan, Z. and Sun, R. 2003. 'An Improved Model Calculating CO_2 Solubility in Pure Water and Aqueous NaCl Solutions from 273 to 533 K and from 0 to 2000 bar'. Chemical Geology, Volume 193, Pages 257 – 271.

Farajzadeh, R., Zitha, P. L. J. and Bruining, H. 2009. 'Enhanced Mass Transfer of CO_2 into Water: Experiment and Modelling'. SPE paper 121195 presented at EUROPE/EAGE Annual Conference and Exhibition, Amsterdam, The Netherlands, 8 – 11 June.

Fernando, W. J. N., Othman, M. R. and Karunaratne, D. G. G. P. 2010. 'Agitation Speed and Interfacial Mass Transfer Coefficients in Mass Transfer Dominated Reactions'. International Journal of Engineering and Technology, Volume 11, Number 1.

Heywood, N. I., Madhvi, P. and McDonagh, M. 1985. 'Design of Ungassed Baffled Mixing Vessels to Minimise Surface Aeration of Low Viscosity Fluids'. Presented at the 5th European Conference on Mixing, Wurtzburg, West Germany, June 10 – 12.

Higbie, R. 1935. 'The Rate of Absorption of Pure Gas into a Still Liquid During Short Period of Exposure'. Transactions of the American Institute of Chemical Engineers. Volume 31, Issue 2, Page 365 – 389.

Hill, G. A. 2006. 'Measurement of Overall Volumetric Mass Transfer Coefficients for Carbon Dioxide in a Well – Mixed Reactor Using a pH Probe'. Industrial and Engineering Chemistry Research, Volume 45, Pages 5796 – 5800.

In Salah Gas. 2012. 'In Salah CO_2 Project', website viewed on April 2nd 2012, http://www.insalahco2.com/index.php?option=com_content&view=frontpage&Itemid=1&lang=en.

The International Association for the Properties of Water and Steam. (IAPWS). 1997. 'IAPWS Industrial Formulation 1997'. Retrieved March 27th, 2012, http://www.iapws.org.

Jain, L. 2011. 'Factors Determining Rapid and Efficient Geologic Storage of CO_2', MS Thesis, The University of Texas at Austin.

Johns, R. T. 2010. 'Advanced Thermodynamics and Phase Behavior'. Graduate course taught at UT Austin during Spring semester.

Joshi, J. B., Pandit, A. B. and Sharma, M. 1982. 'Mechanically Agitated Gas-Liquid Reactors'. Chemical Engineering Science, Volume 37, Number 6, Pages 813 – 844.

King, M. B., Mubarek, A., Kim, J. D. and Bott, T. R. 1992. 'The Mutual Solubilities of Water with Supercritical and Liquid Carbon Dioxide'. The Journal of Supercritical Fluids, Volume 5, Pages 296 – 302.

Kumar, A. 2004. 'A Simulation Study of Carbon Sequestration in Deep Saline Aquifers', MS Thesis, The University of Texas at Austin.

Kumar, A., Ozah, R., Noh, M., Pope, G. A., Bryant, S., Sepehrnoori and Lake, L. W. 2005. 'Reservoir Simulation of CO_2 Storage in Deep Saline Aquifers'. SPE Journal, September, Pages 336 – 348.

Kwak, T. Y. and Mansoori, G. A. 1986. 'Van der Waals Mixing Rules for Cubic Equations of State. Applications for Supercritical Fluid Extraction Modeling'. Chemical Engineering Science, Volume 41, Number 5, Pages 1303 – 1309.

Lewis, W. K. and Whitman, W. G. 1924. 'Principles of Gas Absorption'. Paper presented at the Division of Industrial and Engineering Chemistry at the 68th Meeting of the American Chemical Society, Ithaca, New York, United States of America.

Li, D., Graupner, B. J. and Bauer, S. 2011. 'A Method for Calculating the Liquid Density for the CO_2-H_2O-NaCl System Under CO_2 Storage Condition'. Energy Procedia, Issue 4, Pages 3817 – 3824.

Maalej, S., Benadda, B. and Otterbein, M. 2003. 'Interfacial Area and Volumetric Mass Transfer Coefficient in a Bubble Reactor at Elevated Pressures'. Chemical Engineering Science, Volume 58, Pages 2365 – 2376.

Mali, R. G. and Patwardhan, A. W. 2009. 'Characterization of Onset of Entrainment in Stirred Tanks'. Chemical Engineering Research and Design, Volume 87, Pages 951 – 961.

Malinin, S. D. and Kurovskaya, N. A. 1975. 'Solubility of CO_2 in Chloride Solutions at Elevated Temperatures and CO_2 Pressures'. Geochemistry International 12, Pages 199 – 201.

Malinin, S. D. and Savelyeva, N. I. 1972. 'The Solubility of CO_2 in NaCl and $CaCl_2$ Solutions at 25, 50 and 75° Under Elevated CO_2 Pressures'. Geochemistry International 9, Pages 410 – 418.

Mao, S. and Duan, Z. 2008. 'The P, V, T, x Properties of Binary Aqueous Chloride Solutions up to T = 573 K and 100 MPa'. Journal of Chemical Thermodynamics, Volume 40, Pages 1046 – 1063.

Markopoulos, J. and Kontogeorgaki, E. 1995. 'Vortex Depth in Unbaffled Single and Multiple Impeller Agitated Vessels'. Chemical Engineering Technology, Volume 18, Pages 68 – 74.

Martinez, Isidoro. 2012. 'Heat of Solution Data', website viewed on April 14th, 2012, http://webserver.dmt.upm.es/~isidoro/dat1/Heat%20of%20solution%20data.htm.

Matous, J., Sobr, J., Novak, J. P. and Pick, J. 1969. 'Solubility of Carbon Dioxide in Water at Pressures up to 40 atm'. Collection Czechoslovak Chemical Communications, Volume 34, Pages 3982 – 3985.

Mori, Y. H. and Mochizuki, T. 1998. 'Dissolution of Liquid CO_2 into Water at High Pressures: A Search for the Mechanism of Dissolution Being Retarded Through Hydrate-Film Formation'. Energy Conversion, Volume 39, Number 7, Pages 567 – 578.

Nagata, S. 1975. Mixing: Principles and Applications. Wiley, New York, United States of America.

National Climatic Data Center (NCDC). 2012. 'Global Warming Frequently Asked Questions', website viewed on April 2nd, 2012, http://www.ncdc.noaa.gov/oa/climate/globalwarming.html.

National Institute of Standards and Technology (NIST). 2012. 'NIST Chemistry WebBook Thermophysical Properties of Fluid Systems'. Website based calculator used March 27th, 2012, http://webbook.nist.gov/chemistry/fluid.

Nigam, K. D., Pandit, A. B. and Niranjan, K. 1995. 'Effect of Angle of Inclination on Liquid – Phase Controlled Mass Transfer From a Gas Slug'. Chemical Engineering Science, Volume 50, Number 2, Pages 289 – 298.

Niranjan, K., Hashim, M. A., Pandit, A. B. and Davidson, J. F. 1988. 'Liquid-Phase Controlled Mass Transfer From a Gas Slug'. Chemical Engineering Science, Volume 43, Number 6, Pages 1247 – 1252.

Ogasawara, K, Yamasaki, A. and Teng, H. 2000. 'Mass Transfer from CO_2 Drops Traveling in High-Pressure and Low-Temperature Water'. Energy and Fuels, Volume 15, Pages 147 – 150.

Oyevaar, M. H. and Westerterp, K. R. 1989. 'Mass Transfer Phenomena and Hydrodynamics in Agitated Gas – Liquid Reactors and Bubble Columns at Elevated Pressures: State of the Art'. Chemical Engineering Processes, Volume 25, Pages 85 – 98.

Parr Instrument Company. 2012. 'Parr Mini Bench Top Reactors'. Retrieved from website on Marth 27th, 2012. http://www.parrinst.com.

Pauss, A, Andre, G., Perrier, M. and Guiot, S. R. 1990. 'Liquid – to – Gas Mass transfer in Anaerobic Processes: Inevitable Transfer Limitations of Methane and Hydrogen in the Biomethanation Process'. Applied and Environmental Microbiology, Pages 1636 – 1644.

Peng, D. Y. and Robinson, D. B. 1976. 'A New Two-Constant Equation of State. Industrial and Engineering Chemistry: Fundamentals'. Volume 15, Number 1, Pages 59 – 64.

Pritchard, D. T. and Currie, J. A. 1982. 'Diffusion of Coefficients of Carbon Dioxide, Nitrous Oxide, Ethylene and Ethane in Air and their Measurement'. Journal of Soil Science, Volume 33, Issue 2, Pages 175 – 184.

Robinson, C. W. and Wilke, C. R. 1974. 'Simultaneous Measurement of Interfacial Area and Mass Transfer Coefficients for a Well – Mixed Gas Dispersion in Aqueous Electrolyte Solutions'. American Institute of Chemical Engineers Journal, Volume 20, Number 2, Pages 285 – 294.

Rumpf, B., Nicolaisen, H., Ocal, C. and Maurer, G. 1994. 'Solubility of Carbon Dioxide in Aqueous Solutions of Sodium Chloride: Experimental Results and Correlation'. Journal of Solution Chemistry, Volume 23, Number 3, Pages 431 – 448.

Sandler, S. I. 2006. Chemical, Biochemical, and Engineering Thermodynamics. John Wiley and Sons, New Jersey, United States of America.

Shyu, G. S., Hanif, N. S. M., Hall, K. R. and Eubank, P. T. 1997. 'Carbon Dioxide-Water Phase Equilibria Results from the Wong-Sandler Combining Rules'. Fluid Phase Equilibria, Volume 130, Pages 73 – 85.

Smit, L. and During, J. 1991. 'Vortex Geometry in Stirred Vessel'. Proceedings of the 7th European Congress of Mixing, Volume 2, Bruges, Belgium, Pages 633 – 639.

Song, Y., Chen, B., Nishio, M. and Akai, M. 2005. 'The Study on Density Change of Carbon Dioxide Seawater Solution at High Pressure and Low Temperature'. Energy, Issue 30, Pages 2298 – 2307.

Span, R. and Wagner, W. 1996. 'A New Equation of State for Carbon Dioxide Covering the Fluid Region from the Triple-Point Temperature to 1100 K at Pressures up to 800 MPa'. Journal of Physical Chemical Reference Data, Volume 25, Number 6, Pages 1509 – 1596.

Sverak, S. and Hruby, M. 1981. 'Gas Entrainment from the Liquid Surface of Vessels with Mechanical Agitators'. International Chemical Engineering, Volume 21, Number 3, Pages 519 – 526.

Talbot, P., Lencki, R. W. and Noue, J. 1990. 'Carbon Dioxide Absorption Characterization of a Bioreactor for Biomass Production of Phormidium Bohneri: Comparative Study of Three Types of Diffuser'. Journal of Applied Phycology, Volume 2, Pages 341 – 350.

Tamimi, A., Rinker, E. B., and Sandall, O. C. 1994. 'Diffusion coefficients for hydrogen sulfide, carbon dioxide and nitrous oxide in water over the temperature range 293 – 368K'. Journal of Chemical Engineering Data, Volume 39, Pages 330 – 332.

Tanaka, M., Noda, S. and O'Shima, E. 1986. 'Effect of the Location of a Submerged Impeller on the Enfoldment of Air Bubbles from the Free Surface in a Stirred Vessel'. International Chemical Engineering Journal, Volume 26, Number 2, Pages 314 – 318.

Teng, H. and Yamasaki, A. 1998. 'Mass Transfer of CO_2 Through Liquid CO_2-Water Interface'. International Journal of Heat and Mass Transfer, Volume 41, Pages 4315 – 4325.

Treybal, R. E. 1980. Mass – Transfer Operations. McGraw – Hill, New York, United States of America.

U.S. Environmental Protection Agency (EPA). 2012. 'Climate Change', website viewed on April 1st 2012, http://www.epa.gov/climatechange/.

Vazquez, G., Antorrena, G., Navaza, J. M. and Santos, V. 1996. 'Absorption of CO_2 by Water and Surfactant Solutions in the Presence of Induced Marangoni Effect'. Chemical Engineering Science, Volume 51, Number 12, Pages 3317 – 3324.

Veljkovic, V. B., Bicok, K. M. and Simonovic, D. M. 1991. 'Mechanism, Onset and Intensity of Surface Aeration in Geometrically-Similar, Sparged, Agitated Vessels'. The Canadian Journal of Chemical Engineering, Volume 69, Pages 916 – 926.

Wiebe, R. and Gaddy, V. L. 1939. 'The Solubility in Water of Carbon Dioxide at 50, 75 and 100°, at Pressures to 700 Atmospheres'. Journal of the American Chemical Society, Volume 61, Pages 316 – 318.

Wiebe, R. and Gaddy, V. L. 1940. 'The Solubility of Carbon Dioxide in Water at Various Temperatures from 12 to 40° and at Pressures to 500 Atmospheres'. Journal of the American Chemical Society, Volume 62, Pages 815 – 817.

Wilke, C. R. and Chang, P. 1955. 'Correlations of Diffusion Coefficients in Dilute Solutions'. American Institute of Chemical Engineers Journal, Volume 1, Number 2, Pages 264 – 270.

Wong, D. S. H. and Sandler, S. I. 1992. 'A Theoretically Correct Mixing Rule for Cubic Equations of State.' American Institute of Chemical Engineers Journal, Volume 38, Number 5, Pages 671 – 680.

Xu, T., Kharaka, Y. K., Doughty, C., Freifeld, B. M. and Daley, T. M. 2010. 'Reactive Transport Modeling to Study Changes in Water Chemistry Induced by CO_2 Injection at the Frio-I Pilot'. Chemical Geology, Volume 271, Pages 153 – 164.

Xu, T., Sonnenthal, E., Spycher, N. and Pruess, K. 2006. 'TOUGHREACT – A Simulation Program for Non-Isothermal Multiphase Reactive Geochemical Transport in Variably Saturated Geologic Media: Applications to Geothermal Injectivity and CO_2 Geological Sequestration'. Computers and Geosciences, Volume 32, Pages 145 – 165.

Yang, C. and Gu, Y. 2006. 'Accelerated Mass Transfer of CO_2 in Reservoir Brine Due to Density Driven Natural Convection at High Pressures and Elevated Temperatures'. Industrial and Engineering Chemical Research, Issue 45, Pages 2430 – 2436.

Zhang, Y., Lynn, R. J., Holder, G. D. and Warzinski, R. P. 2005. 'Mass Transfer from CO_2 Drops and the Apparent Solubility of CO_2 Under Deep-Ocean Conditions'. Conference Proceedings from the Fourth Annual Conference on Carbon Capture and Sequestration, May 2 – 5.

Vita

Christopher Allen Johnson Blyton graduated with a Master of Science in Engineering from The University of Texas at Austin. His research focused on experimental study of the kinetics of CO_2 dissolution into brine. Application of the original data obtained demonstrated that secure geologic sequestration of CO_2 by the novel surface dissolution approach is feasible. Mr. Blyton holds a Bachelor of Engineering from the University of Wollongong, Australia. He worked in the automotive industry for two years pre and post graduation. A change of career to the energy industry and a three-year international field career with Schlumberger followed, before he returned to university study.

Permanent email: chris.blyton@gmail.com

This thesis was typed by the author.